

**Fluctuation Induced Conductivity of Nano-particle doped
CuTl – 1223 Superconductor**



By

Asif Iqbal Bhatti

Registration No. 19-FBAS/MSPHY/F10



Department of Physics
Faculty of Basic and Applied Science
INTERNATIONAL ISLAMIC UNIVERSITY
ISLAMABAD, PAKISTAN
2012

Accession No TH-9334

MS
S30
BHF

① physics

INTERNATIONAL ISLAMIC UNIVERSITY
FACULTY OF BASIC AND APPLIED SCIENCE
DEPARTMENT OF PHYSICS
ISLAMABAD, PAKISTAN
2012

**Fluctuation Induced Conductivity of Nano-particle doped $CuTl - 1223$
Superconductor**

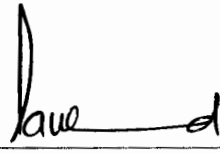
By

Asif Iqbal Bhatti

(Registration No. 19-FBAS/MSPHY/F10)

A thesis submitted to **Department of Physics**, International Islamic University Islamabad for the award of the degree of **MS Physics**.

Signature: _____

 9/08/2012

(Chairman, DOP)

Signature: _____



13/8/12
DEAN
Dean FBAS, Faculty of Basic & Applied Science,
International Islamic University,
Islamabad

ACCEPTANCE BY THE VIVA VOCE COMMITTEE

Title of Thesis: Fluctuation Induced Conductivity of Nano-particle doped
CuTl – 1223 Superconductor
Name of Student: Asif Iqbal Bhatti
Registration No. 19-FBAS/MSPHY/F10

Accepted by the Department of Physics, Faculty of Basic & Applied Sciences,
INTERNATIONAL ISLAMIC UNIVERSITY ISLAMABAD, in partial Fulfilment of the
requirements for the Master of Science in Physics with specialization in superconductivity.

VIVA VOCE COMMITTEE

Dean

Lawe d

Chairman/Director/Head

9/08/2012

DR. Iftikhar Hussain Gul

External Examiner

for Lawe d

Research Supervisor

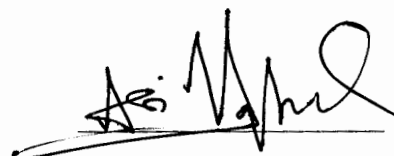
Karim Nadeem

Member

DECLARATION

I *Asif Iqbal Bhatti* (19-FBAS/MSPHY/F10), student of MS in Physics (session 2010 – 2012), hereby declare that the matter printed in the thesis titled “Fluctuation Induced Conductivity of Nano-particle doped $CuTl - 1223$ Superconductor” is my own research work and has not been published or submitted as research work or thesis in any form in any other university or institute in Pakistan or abroad.

Dated: 09/08/2012


Signature of Deponent

ACKNOWLEDGMENTS

First, I owe my deepest gratitude to Allah (SWT) for all of his blessings and rationality for deciphering the ungraspable knowledge and yet comprehensible. Next, I wish to acknowledge my achievements to my parents for being supportive and not burdening me with other matters.

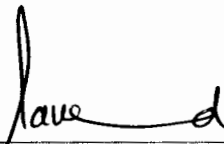
I would like to acknowledge the worth mentioning supervision of Dr. Muhammad Mumtaz. His supervision from the preliminary to the concluding level has enabled me to develop an understanding of this field. His wide and deep knowledge have been great value for me. I would like to also thank Dr. Kashif Nadeem for his guidance and support.

ASIF IQBAL BHATTI

FORWARDING SHEET BY RESEARCH SUPERVISOR

The thesis entitled "Fluctuation Induced Conductivity of Nano-particle doped $CuTl - 1223$ Superconductor" submitted by Asif Iqbal Bhatti in partial fulfilment of MS degree in Physics has been completed under my guidance and supervision. I am satisfied with the quality of student research work and allow him to submit this thesis for further process to graduate with Master of Science Degree from Department of Physics, as per IIU rules & regulation.

Date: 9/08/2012

for


Muhammad Mumtaz, Ph. D
Assistant Prof (TTS)
Department of Physics
International Islamic University
Islamabad.

TABLE OF CONTENTS

DECLARATION.....	II
ACKNOWLEDGMENTS	III
FORWARDING SHEET BY RESEARCH SUPERVISOR	IV
TABLE OF CONTENTS.....	V
LIST OF TABLES.....	VII
LIST OF FIGURES	VIII
ABSTRACT.....	X
CHAPTER 1	1
INTRODUCTION	
1.1. SUPERCONDUCTIVITY	1
1.2. THE MEISSNER EFFECT	3
1.3. DIAMAGNETISM IN SUPERCONDUCTOR	3
1.4. CRITICAL PARAMETERS OF SUPERCONDUCTIVITY	4
1.4.1 Critical Temperature (T_c).....	4
1.4.2 Critical Magnetic Field (H_c)	4
1.4.3 Critical Current (I_c).....	5
1.5 TYPES OF SUPERCONDUCTORS	5
1.5.1 Type-I and Type-II Superconductors.....	5
1.6 THEORIES FOR CONVENTIONAL SUPERCONDUCTORS	7
1.6.1 London Equations	7
1.6.2 Ginzburg Landau (GL) Theory.....	8
1.6.3 Coherence Length(ξ) and Penetration Depth(λ)	9
1.6.4 BCS Theory of Superconductivity.....	10
1.7 VORTICES AND FLUX PINNING	10
1.8 JOSEPHSON EFFECT	11
1.9 CLASSIFICATION SYSTEM TO DESCRIBE STRUCTURE TYPES	12
1.10 STRUCTURE OF HTSCS.....	13
1.11 MATERIAL IMPERFECTION	14
1.12 PHASE DIAGRAM.....	15
1.13 DISCOVERY AND CHEMISTRY OF THALLIUM-BARIUM-CALCIUM-COPPER OXIDE (TBCCO) SYSTEM SUPERCONDUCTORS	16
1.13.1 $CuTl$ -based Superconductors.....	18
1.14 EFFECTS OF OXYGEN NONSTOICHIOMETRIC ON SUPERCONDUCTIVITY	19
1.15 NANO-SCIENCE	19
1.16 TYPES OF NANO-STRUCTURES	19
1.17 MORPHOLOGY OF NANOPARTICLE.....	20
1.18 PROPERTIES OF CUPRIC OXIDE (CuO) NANOPARTICLES	20

1.19	SMALL-SCALE SUPERCONDUCTIVITY	21
------	-------------------------------------	----

CHAPTER 2.....22

THEORY OF FIC AND LITERATURE REVIEW

2.1	FLUCTUATION INDUCED CONDUCTIVITY (FIC).....	22
2.2	MEAN FIELD THEORY (MFT)	24
2.3	LITERATURE REVIEW	24
2.4	MOTIVATION.....	30

CHAPTER 3.....31

SYNTHESIS AND EXPERIMENTAL TECHNIQUES

3.1	SYNTHESIS TECHNIQUES.....	31
3.1.1	Solid State reaction method	31
3.2	TECHNIQUES TO SYNTHESIZE NANO-PARTICLE	32
3.2.1	Co-precipitation method	32
3.3	SAMPLE PREPARATION.....	32

3.3.1	Synthesis of [L,]	32
3.3.2	Synthesis of CuO nano-particles.....	34
3.4	CHARACTERIZATION TECHNIQUES:	34
3.4.1	X-ray Diffraction.....	34
3.4.2	Scanning Electron Microscopy (SEM) and Energy Dispersive X-ray Analysis (EDX).....	36
3.4.3	DC resistivity	38

CHAPTER 4.....40

RESULTS AND DISCUSSION

4.1	INTRODUCTION	40
4.2	RESULTS AND DISCUSSION	42
4.2.1	X-ray diffraction (XRD)	42
4.2.2	Scanning Electron Microscopy (SEM) and Energy Dispersive X-ray (EDX)	43

LIST OF TABLES

Table 1.1:	Homologues series of <i>Tl</i> compounds.	16
Table 4.1:	The energy dispersive <i>X</i> -ray (EDX) analysis of $(CuO)_x/CuTl - 1223$; $x = 15\%$ composite showing % of different parameters.	44
Table 4.2:	The critical exponents (λ_{2D} and λ_{3D}), extracted from the FIC analysis of as-prepared and oxygen post-annealed $(CuO)_x/CuTl - 1223$ composites with $x = 0\%, 10\%, 15\%$ and 20% .	51
Table 4.3:	The parameters such as normal state resistivity $\rho_n(290K)$, the zero resistivity critical temperature (T_c), onset of superconductivity (T_c^{onset}), cross-over temperatures (T_o), mean field critical temperature (T_c^{mf}), INTER-GRAIN COUPLING CONSTANT (α), zero temperature coherence length along <i>c</i> -axis $\{\xi_c(0)\}$ and inter-plane coupling (J) extracted from the FIC analysis of as-prepared $(CuO)_x/CuTl - 1223$ composites with $x = 0\%, 10\%, 15\%$ and 20% .	59
Table 4.4:	The widths of 3D and 2D fluctuation regions observed from the fitting of the experimental data using AL model on resistivity data of as-prepared $(CuO)_x/CuTl - 1223$ composites with $x = 0\%, 10\%, 15\%$ and 20% .	60
Table 4.5:	The parameters such as normal state resistivity $\rho_n(290K)$, the zero resistivity critical temperature (T_c), onset of superconductivity (T_c^{onset}), cross-over temperatures (T_o), mean field critical temperature (T_c^{mf}), INTER-GRAIN COUPLING CONSTANT (α), zero temperature coherence length along <i>c</i> -axis $\{\xi_c(0)\}$ and inter-plane coupling (J) extracted from the FIC analysis of oxygen post-annealed $(CuO)_x/CuTl - 1223$ composites with $x = 0\%, 10\%, 15\%$ and 20% .	61
Table 4.6:	The widths of 3D and 2D fluctuation regions observed from the fitting of the experimental data using AL model on resistivity data of oxygen post-annealed $(CuO)_x/CuTl - 1223$ composites with $x = 0\%, 10\%, 15\%$ and 20% .	61

LIST OF FIGURES

1.1	Vanishing resistance at 0K as discovered by Onnes.	1
1.2	History of superconductor development with time.	2
1.3	Exclusion of magnetic field in a superconducting state.	3
1.4	Magnetic susceptibility of a superconductor as a function of temperature. Above T_c it is constant normal state value, χ_n , which is small and positive (paramagnetic). Below T_c the susceptibility is large and negative, $\chi = -1$, portraying perfect diamagnetism.	4
1.5	Variation of critical magnetic field with temperature.	5
1.6	Behaviour of Type-I and Type-II superconductor in magnetic field versus temperature.	6
1.7	Penetration depth along one dimension.	8
1.8	Interaction between two electrons via phonon.	10
1.9	Magnetic flux inside the sheet of high temperature superconductors.	11
1.10	Manifestation of Josephson Effect (a) SIS (b) Intergrain coupling (c) Tunnelling between <i>Cu</i> planes.	12
1.11	General structure of a cuprates HTSCs ($A_m E_2 C a_{n-1} C u_n O_{2n+m+2+y}$) for $m = 1$.	13
1.12	The crystal boundary between two grains (HTSCs microstructure). The dark green dot indicates the secondary phases. Moreover, oxygen reduction can be controlled at grain boundaries.	14
1.13	Orientations of three types of grain boundaries (shaded region).	15
1.14	Phase diagram of HTSCs. A competition exists between (antiferromagnetic) AF and superconductivity (SC) state. Pseudo-gap T^* is thought to be the precursor for superconducting state (SC).	15
1.15	Crystal structures of <i>Tl</i> monolayer superconducting oxides $TlBa_2Ca_{n-1}Cu_nO_{2(n+1)}$ ($n = 1 - 5$).	17
1.16	Crystal structure of <i>CuTl</i> - 1223 unit cell.	18
1.17	Nanostructures broadly categorized as 1D, 2D and 3D.	19
1.18	A perspective view of the crystal structure of <i>CuO</i> .	20
2.1	Schematic representation of FIC theory.	23
3.1	Flow chart of preparation of HTSC sample.	33
3.2	Diffraction of <i>X</i> -rays from crystal planes.	35
3.3	Schematic diagram of <i>X</i> -ray diffractometer.	36
3.4	Types of electrons emitted from a specimen. The EDS analysis determines the characteristics <i>X</i> -ray whereas SEM scans determines BSE.	37

3.5	EDS output from X-rays.	38
3.6	Arrangement for resistivity measurements.	39
4.1(a)	The X-ray diffraction (XRD) patterns of $(CuO)_x/CuTi - 1223$ composites (a) $x = 0\%$.	42
	(b) The X-ray diffraction (XRD) patterns of $(CuO)_x/CuTi - 1223$ composites (a) $x = 15\%$.	43
4.2(a)	The X-ray diffraction (XRD) patterns of $(CuO)_x/CuTi - 1223$ composites (a) $x = 0\%$.	44
	(b) The X-ray diffraction (XRD) patterns of $(CuO)_x/CuTi - 1223$ composites (a) $x = 15\%$.	45
4.3(a)	The Energy Dispersive X-ray (EDX) analysis of $(CuO)_x/CuTi - 1223$; $x = 15\%$ composite. SEM showing the square portion for EDX.	45
	(b) The Energy Dispersive X-ray (EDX) analysis of $(CuO)_x/CuTi - 1223$; $x = 15\%$ composite.	46
4.4	The resistivity versus temperature measurements of as-prepared $(CuO)_x/CuTi - 1223$ composites with $x = 0\%, 10\%, 15\%$ and 20% .	47
4.5	The resistivity versus temperature measurements of oxygen post-annealed $(CuO)_x/CuTi - 1223$ composites with $x = 0\%, 10\%, 15\%$ and 20% .	47
4.6(a)	$\ln(\Delta\sigma)$ versus $\ln(\epsilon)$ plot of as-prepared $(CuO)_x/CuTi - 1223$ composite with $x = 0\%$.	51
	(b) $\ln(\Delta\sigma)$ versus $\ln(\epsilon)$ plot of as-prepared $(CuO)_x/CuTi - 1223$ composite with $x = 10\%$.	52
	(c) $\ln(\Delta\sigma)$ versus $\ln(\epsilon)$ plot of as-prepared $(CuO)_x/CuTi - 1223$ composite with $x = 15\%$.	53
	(d) $\ln(\Delta\sigma)$ versus $\ln(\epsilon)$ plot of as-prepared $(CuO)_x/CuTi - 1223$ composite with $x = 20\%$.	54
4.7(a)	$\ln(\Delta\sigma)$ versus $\ln(\epsilon)$ plot of oxygen post-annealed $(CuO)_x/CuTi - 1223$ composite with $x = 0\%$.	55
	(b) $\ln(\Delta\sigma)$ versus $\ln(\epsilon)$ plot of oxygen post-annealed $(CuO)_x/CuTi - 1223$ composite with $x = 10\%$.	56
	(c) $\ln(\Delta\sigma)$ versus $\ln(\epsilon)$ plot of oxygen post-annealed $(CuO)_x/CuTi - 1223$ composite with $x = 15\%$.	57
	(d) $\ln(\Delta\sigma)$ versus $\ln(\epsilon)$ plot of oxygen post-annealed $(CuO)_x/CuTi - 1223$ composite with $x = 20\%$.	58

ABSTRACT

Synthesis and characterization of $(CuO)_x/CuTl - 1223$; $\{(CuO)_x/CuTl - 1223\}$ composites with $x = 0\%, 10\%, 15\%$ and 20% have been studied. The fluctuations induced conductivity (FIC) analysis of $(CuO)_x/CuTl - 1223$ composites has been carried out using Aslamazov-Larkin (AL) and Lawrence-Doniach (LD) models in the temperature regime well above the critical temperature ($T > T_c$). The electrical resistivity versus temperature curves of as-prepared and oxygen post-annealed $(CuO)_x/CuTl - 1223$ composites were fitted by using above mentioned models to extract the microscopic parameters such as zero temperature coherence length along c -axis $\{\xi_c(0)\}$, inter-layer coupling (J), dimensional critical exponent (λ) and inter-grain coupling constant (α) etc. It has been observed that the cross-over temperature (T_o) fits very well with two-dimensional (2D) and three-dimensional (3D) AL equations and shifts towards the lower temperature regime with the enhanced weight % of CuO nano-particles. The shifting of AL 3D region to higher temperature after oxygen post-annealing indicates the restoration of the oxygen and optimization of charge carriers in conducting CuO_2 planes of $CuTl - 1223$ superconductor. The gradual decrease in the value of inter-grain coupling constant (α) with the increase of CuO nano-particles content reflects an improvement in the inter-grain coupling resulting into an increase in the coherence length (ξ_c) along the c -axis. Almost all superconductivity parameters have been improved after oxygen post-annealing. The suppression of superconductivity parameters in the composites with $x = 20\%$ limits the optimum doping level of CuO nano-particles in $(CuO)_x/CuTl - 1223$ composites.

Chapter 1

INTRODUCTION

This chapter starts with the brief description of superconductivity, its brief history, classifications, simplest theoretical models and its consequences in particular the existence of vortices in superconductors moreover, difference between Type-I and Type-II superconductors, BCS theory, Tl -based superconductors (cell structure) and nano-science.

1.1. Superconductivity

The phenomenon in which the electrical resistance of certain materials completely vanishes at low temperatures, is one of the most interesting and sophisticated phenomenon in “*condensed matter physics*” In 1911 Kamerlingh Onnes and some of his subordinates were studying the resistance of metals at very low temperatures unexpectedly they discovered superconductivity. Onnes realized that this new phenomenon epitomized a new physical state and he termed it the “*superconductive state*” as depicted in Fig. 1.1. They studied the pure sample of mercury because it is easily prepared by condensation [1].

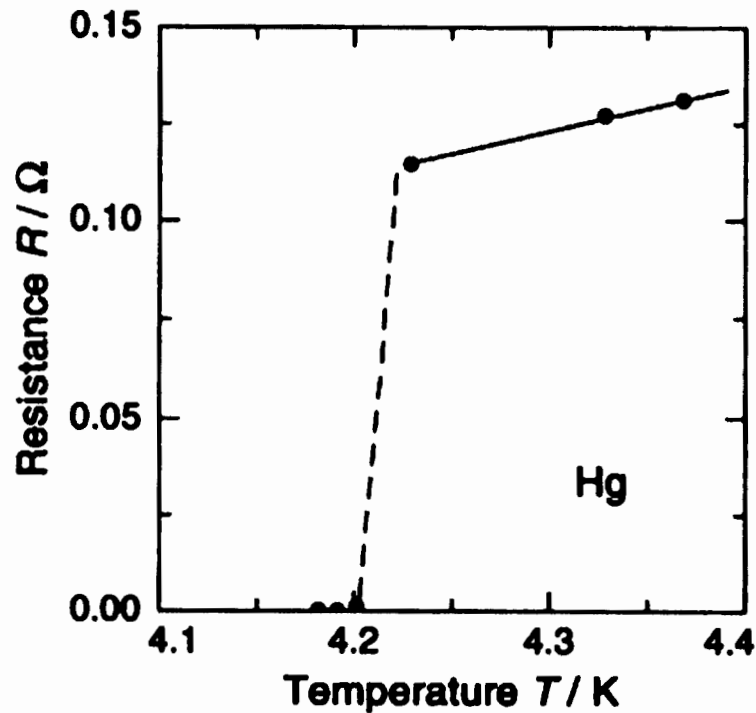


Fig. 1.1: Vanishing resistance at $0K$ as discovered by Onnes [1].

His further investigation showed that other metals such as tin and lead also enter the superconducting state if they are cooled below 3.8 K and 7.2 K, respectively. The temperature at which the shift takes place from the normal state to the state of superconductivity was called the “critical temperature” (T_c). Onnes also observed that although it was possible to pass a huge electric current through the superconducting mercury sample, there was a threshold value for the current density above which the sample would return to the normal state. This threshold value is called the “critical current density” (J_c). Moreover, he also discovered that magnetic fields higher than H_c , the “critical magnetic field”, can similarly destroy the superconducting state [7]. A significant breakthrough was made in 1986 by George Bednorz and Alex Müller, at the IBM Laboratory in Switzerland, when they made a ceramic superconductor from lanthanum, barium, copper, and oxygen (La – Ba – Cu – O) with a transition temperature of 35 K [16]. In 1987 superconductivity was also discovered by substitution of yttrium for lanthanum, another ceramic superconductor (Y – Ba – Cu – O), with a transition temperature of 92 K jointly by two groups namely Chu’s and Wu’s group [16]. This was significant because it had become possible to use cheap liquid nitrogen as refrigerant. Then the era of new exotic materials emerges they called these materials “High Temperature Superconductors” (HTSCs). Some compounds of superconductor, T_c versus year of finding are given in Fig. 1.2.

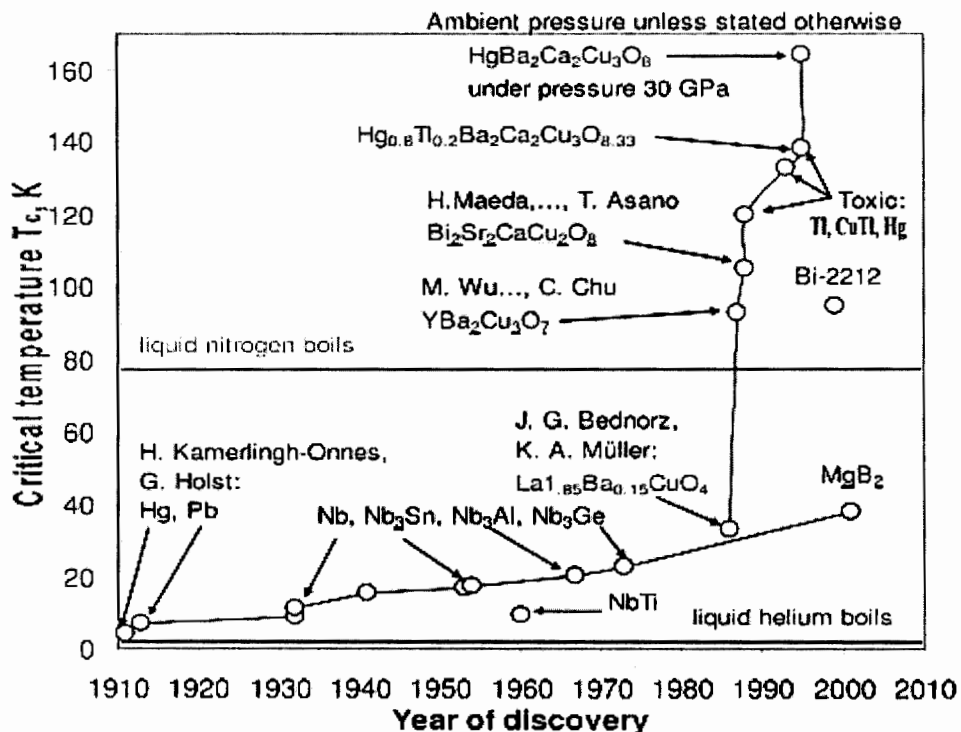


Fig. 1.2: History of superconductor development with year [7].

1.2. The Meissner Effect

Meissner and Ochsenfeld in 1933 discovered that superconductor in an external magnetic field expels it. They observed that when material is cooled below its critical temperature in a magnetic field, the electric current is generated due to the induced field near the surface of a sample which creates the field in such a way so as to cancel the outside field. Stated differently, the material becomes fully diamagnetic and is an intrinsic property of superconductors. This unique property sets the criterion for testing completely whether the sample is superconductor or not [2, 3] as shown in Fig. 1.3.

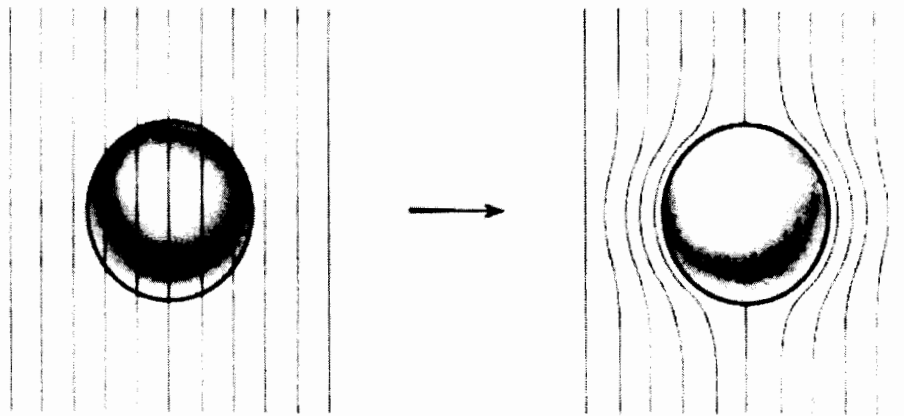


Fig. 1.3: Exclusion of magnetic field in the superconducting state [2, 3].

1.3. Diamagnetism in Superconductor

Interior to the superconducting material the induced magnetic field can be given as

$$B = \mu_0 (H + M) = \mu_0(1 + \chi)H \quad (1.1)$$

where H and M are the external magnetic field and magnetization respectively, and χ is the magnetic susceptibility. As, the material is in the superconducting state this implies that $B = 0$, which shows $M = -H$. Thus, this condition indicates the medium is perfect

diamagnetic; and its susceptibility is $\chi = -1$ [4, 5]. Fig. 1.4 indicates the paramagnetic and diamagnetic state.

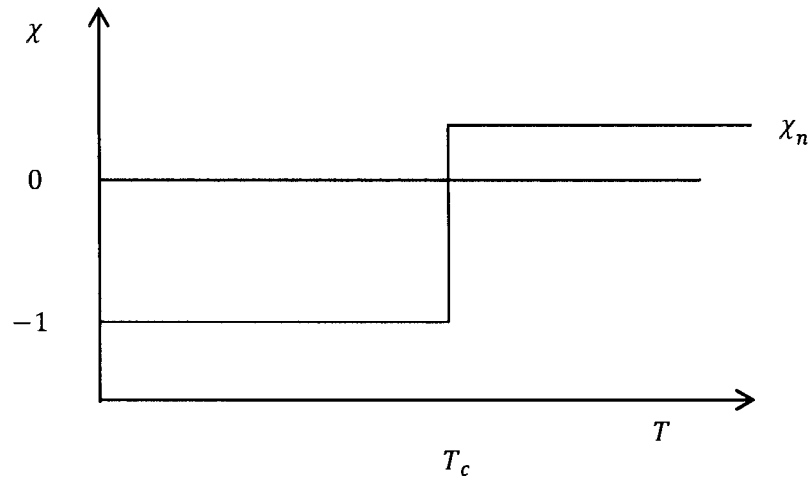


Fig. 1.4: Magnetic susceptibility of a superconductor as a function of temperature. Above T_c it is constant normal state value, χ_n , which is small and positive (paramagnetic). Below T_c the susceptibility is large and negative, $\chi = -1$, portraying perfect diamagnetism.

1.4. Critical parameters of Superconductivity

1.4.1 Critical Temperature (T_c)

The temperature at which superconductors lose its resistance is called a critical temperature. This temperature is denoted by T_c ; below this temperature electrical resistance of the superconductor is negligible [6].

1.4.2 Critical Magnetic Field (H_c)

The superconductivity may be destroyed and normal resistance can be restored with the application of magnetic field. This value of magnetic field for the destruction of superconductivity is known as “critical field” and is denoted by H_c . The relation between the critical field and the temperature is vital for describing the properties of any superconductor. Silsbee’s rules tell us the relation between H_c and temperature by the equation,

$$H_c = H_o \left[1 - \left(\frac{T}{T_c} \right)^2 \right] \quad (1.2)$$

The variation of field with temperature is shown in the Fig. 1.5.

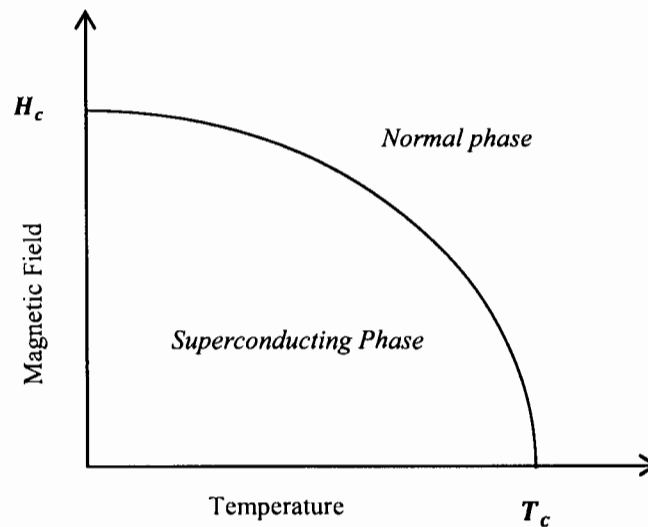


Fig. 1.5: Variation of critical magnetic field with temperature.

1.4.3 Critical Current (I_c)

Superconductivity is destroyed when the value of current I is increased beyond the certain limit. This limit is called the critical current I_c and it is important property for classifying the superconducting materials for wire technology [5].

1.5 Types of Superconductors

In general, there are two types of superconductor. In literature these are categorized by their dimensionality for example 3D organic superconductors (alkali-doped fullerene $RbCs_2C_{60}$), 2D Li_2CuO_2 and CNTs 1D superconductor. Other property of superconductors besides repelling magnetic fields includes “*enhanced thermal conductivity*”, “*higher optical reflectivity*” and “*reduced surface friction*” [8].

1.5.1 Type-I and Type-II Superconductors

Abrikosov, in his original paper, studied the properties of superconductors in external magnetic fields and discovered they can be separated into two groups [9]. His brilliant predictions were experimentally confirmed about three years later.

Type-I superconductors are those, which shows a sharp transition. These materials are composed of “*metals*” and “*metalloids*” and are characterized as “*soft*” superconductors and exhibit perfect diamagnetism [8]. Type-II superconductors do not have abrupt transition. They have a perovskites structure and are made up of metallic compounds and alloys. Up to H_{c1} , material is a perfect diamagnetic and between H_{c1} and H_{c2} , the material is partly diamagnetic, i.e. there is some flux penetration into the material and irreversible¹ effects are seen. Above H_{c2} , the material is in paramagnetic state. Type-II is characterized as “*hard*” superconductors [10] as shown in Fig. 1.6.

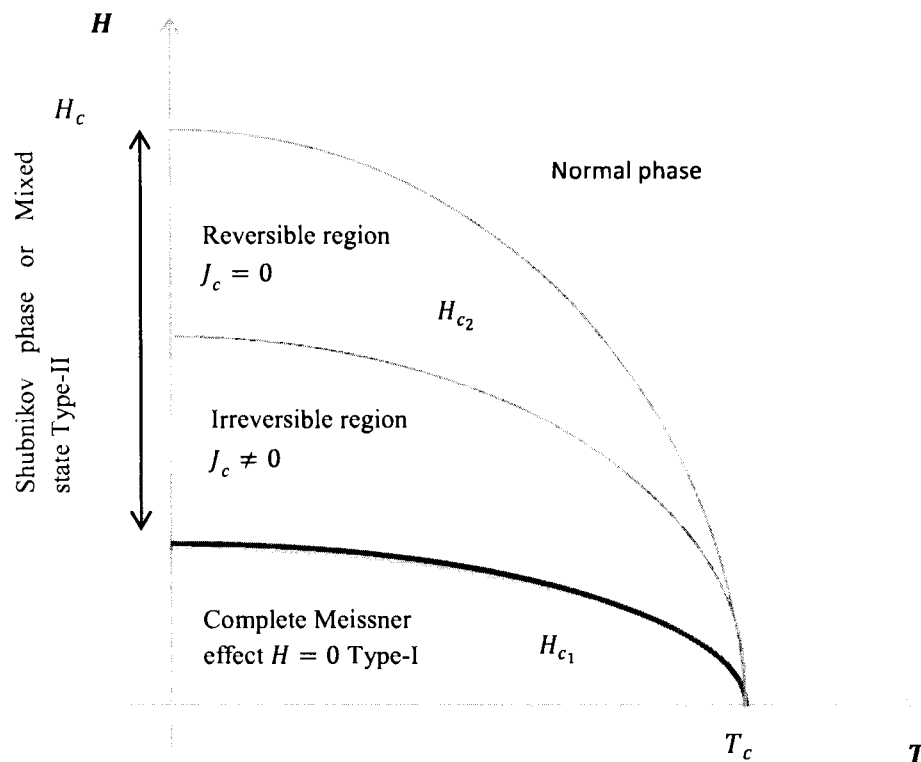


Fig. 1.6: Behaviour of Type-I and Type-II superconductor in magnetic field versus temperature [49].

¹ The region where the vortices cannot be impeded in the presence of magnetic field.

1.6 Theories for conventional Superconductors

Many theories were presented earlier after the discovery of conventional superconductivity but which became authoritative for explaining broad or specific phenomena are discussed here,

1.6.1 London Equations

Electrodynamics of superconductivity was mathematically done by Fritz and Heinz London in 1935 [12]. Their equations explain the Meissner effect; they predict how the magnetic field and surface current vary with distance from the surface of a superconductor. To introduce the Meissner effect, the London brothers suggested that Maxwell's Equation could be replaced by more restrictive relationship,

$$\text{curl } J_s = -\frac{n_s e^2}{m} B \quad (1.3)$$

$$\frac{\partial J_s}{\partial t} = \frac{n_s e^2}{m} E \quad (1.4)$$

Where n_s , e , m are the density of superconducting electrons, charge on an electron and mass of an electron respectively. As these equations are not the explanations of superconductivity phenomenon. They are introduced as a constraint on Maxwell's equations so that the behavior of superconductors inferred from these equations was consistent with experimental observations and in particular with the Meissner effect. To know how the London equations lead to the Meissner effect; first assume for the perfect conductor. We use Ampère's law, $\text{curl } B = \mu_0 J_s$ to substitute for J_s in above equation, and we obtain,

$$\text{curl}(\text{curl } B) = -\frac{\mu_0 n_s e^2}{m} B = -\frac{1}{\lambda^2} B \quad (1.5)$$

Where,

$$\lambda = \left(\frac{m}{\mu_0 n_s e^2} \right)^{\frac{1}{2}} \quad (1.6)$$

But,

$$\text{curl}(\text{curl } B) = \text{grad}(\text{div } B) - \nabla^2 B = -\nabla^2 B \text{ since, } \text{div } B = 0. \quad (1.7)$$

So,

$$\nabla^2 B = \frac{1}{\lambda^2} B \quad (1.8)$$

The important point to note about this equation is; the only solution which corresponds to a spatially uniform field (for which $\nabla^2 B = 0$) is the field that is identically zero everywhere. If B was not equal to zero, then $\nabla^2 B$ would not be zero, so B would depend on position. If we consider again the simple one-dimensional geometry shown in Fig. 1.7.

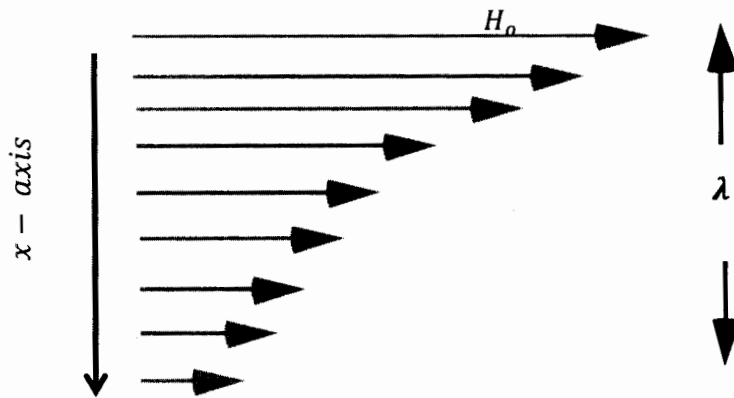


Fig. 1.7: Penetration depth of superconductor along one dimension.

we obtain the solution by separations of variables, which is,

$$B_x(z) = B_0 e^{-\frac{z}{\lambda}} \quad (1.9)$$

This solution has remarkable predictions associated with it. Firstly, it predicts the exponential decay. Secondly λ , penetration depth, describes the decay of magnetic field at the boundary of a superconductor. This decay depends on the density n_s of superconducting electrons [11].

1.6.2 Ginzburg Landau (GL) Theory

GL theory is a phenomenological theory that models superconductivity. It explains the mechanism behind superconductivity in terms of thermodynamics not the microscopic details governing superconductivity. The GL theory concentrates entirely on the superconducting electrons rather than on excitations. The uniqueness of this theory which is lacked by the London's theory is, the effects of nonlinearity in the presence of strong fields,

which as a consequences has the ability to alter the n_s or $|\psi|^2$ and the variation of the super-electrons in three-dimensional. A major triumph of this theory was to handle the intermediate state of superconductors in which superconducting and normal domains co-exist in the presence of $H = H_c$. A mode of their thinking begin when they reasoned that the complex order parameter ψ , can be written in terms of Gibbs free energy in the vicinity of transition temperature. The equation which relates these parameters is written as,

$$F = F_n + \alpha|\psi|^2 + \frac{\beta}{2}|\psi|^4 + \frac{1}{2m}|(-i\hbar\nabla - 2eA)\psi|^2 + \frac{|\psi|^2}{2\mu_0} \quad (1.10)$$

where F_n is the Gibbs free energy of the normal phase, α and β are phenomenological parameters, m is an effective mass, e is the charge of an electron, A is the magnetic vector potential (distribution of magnetic field in the area) and $B = \nabla \times A$ is the magnetic field. Taking derivative of free energy with respect to the order parameter and magnetic vector potential and thus minimizing one get,

$$\alpha|\psi| + \beta|\psi|^3 \psi + \frac{1}{2m}(-i\hbar\nabla - 2eA)^2\psi = 0 \quad (1.11)$$

$$j = \frac{2e}{m} \text{Re}\{\psi^*(-i\hbar\nabla - 2eA)\psi\} \quad (1.12)$$

Equation 1.12 shows the electrical current density j in terms of magnetic vector potential and equation 1.11 gives the relation of ψ in the vicinity of applied magnetic field [11, 13].

1.6.3 Coherence Length(ξ) and Penetration Depth(λ)

The results that predicted by the equations of GL were the *coherence length* “ ξ ”, and the *penetration depth* “ λ ”. The coherence length

$$\xi = \sqrt{\frac{\hbar^2}{2m|\alpha|}} \quad (1.10)$$

describes the size of thermodynamic fluctuations in the superconducting phase and the penetration depth

$$\lambda = \sqrt{\frac{m}{4\mu_0 e^2 \psi_0^2}} \quad (1.10)$$

(where ψ_0 is the equilibrium value in the absence of magnetic field) defines the depth to which an external magnetic field can penetrate at the surface of superconductor (SC). The

ratio $\kappa = \lambda/\xi$ is known as Ginzburg–Landau parameter [13]. where

$$\kappa = \begin{cases} 0 < \kappa < \frac{1}{\sqrt{2}}, & \text{Type-I} \\ \kappa > \frac{1}{\sqrt{2}}, & \text{Type-II} \end{cases} \text{ describes two phases of superconductor.}$$

1.6.4 BCS Theory of Superconductivity

The theoretical understanding of Type-I superconductors were showed by John Bardeen, Leon Cooper, and Robert Schrieffer or BCS. They explain it with the aid of electron phonon interaction. When electron moves through the lattice, it deforms the structure. The second electron sees this deformation try to pair with the electron, to minimize the energy of the system. Moreover, the paired electrons are termed as cooper pairs as shown in Fig. 1.8. In this theory, they explain that not all electrons takes part in forming cooper pairs instead those near the Fermi level take part and condense into same energy level forming boson state. The cooper pair's energy is less than the band gap energy, when its energy increases beyond the band gap cooper pairs breaks and the superconducting state vanishes [14].

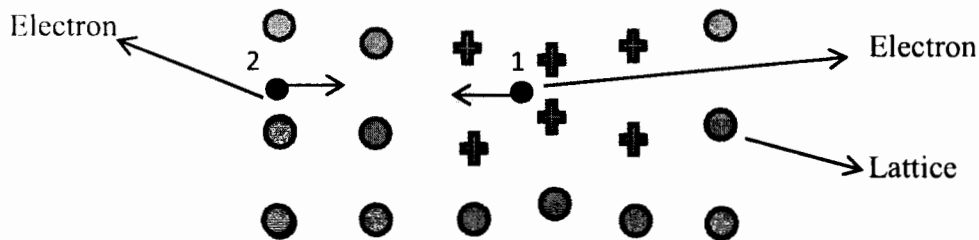


Fig. 1.8: Schematic picture of the electron-phonon interaction, electron 1 creates a polarized region in the lattice (blue) as it travels through the solid. In this deformed part of the lattice there will be an accumulation of positive charge that in turn attracts electron (black dot) 2.

1.7 Vortices and Flux pinning

Type-II superconductor has a mixed state or vortex state where magnetic field gradually penetrates the normal region in superconductor. The mixed state is in the region between H_{c1} and H_{c2} . Inhomogeneous Type-II superconductor contains various types of defects (grain boundaries, dislocation walls, dislocation tangles, voids, or second-phase precipitates) vortices can be pinned by the defects. A finite transport current (external source) is then required to set them moving, such that the Lorentz force produced by it is sufficient to split the vortices off the defects. $F_L = \frac{1}{c} \llbracket J_{tr} \times \boldsymbol{\varphi}_o \rrbracket$ (c.g.s units) where J_{tr} is the external super

current and $\varphi_o = i_v \varphi_o$ where i_v is a unit vector in the direction of magnetic field of the vortex and φ_o is the quantized flux expressed by $\varphi_o = h/2e = 2.0678 \times 10^{-15}$ webers. The latter are often referred to as pinning centres [15].

Vortices interact with many different types of defects. In many case the interaction between the vortex and defect is attractive. Therefore, the vortex is trapped or “*pinned*” at the defect. This will result in superconductor being able to carry some transport current without dissipation, until the Lorentz force from this current is less than the pinning force. If the current density is increased beyond the limit, critical current density, the normal state is restored implying that this transition follows finite dissipation of energy. Pinning of vortices on defects also illustrates Type-II superconductors in the presence of applied magnetic field as shown in the Fig. 1.9 [15].

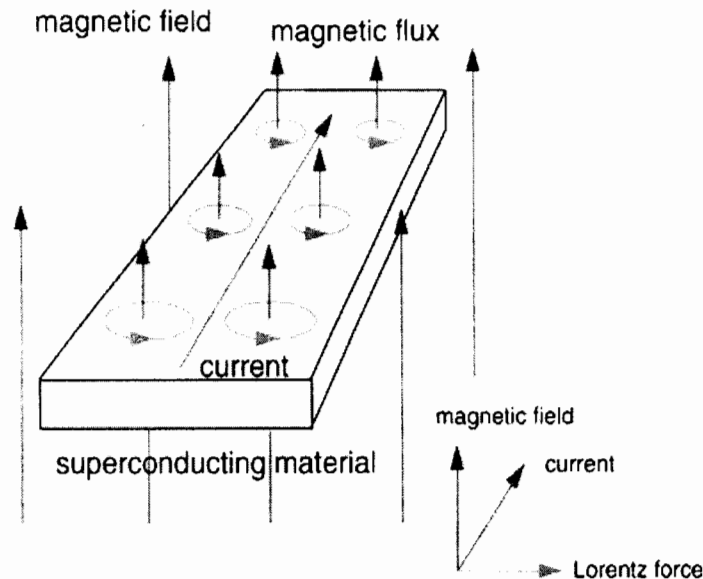


Fig. 1.9: Magnetic flux in the plane of HTSCs. When the superconductor plane is perpendicular to the magnetic field, the quantized magnetic flux starts to flow inside the plane. When the super-current flows parallel to the plane, flux starts to moves in the direction due to Lorentz force with a loss of energy which means that resistivity appears. If these flux movements can be prevented by introducing suitable pinning centres, the resistivity reduced by a considerable factor [15].

1.8 Josephson Effect

The British physicist Brian D. Josephson, in his Ph. D. thesis predicted the existence of a phenomenon where the cooper pairs in the form of current (*Josephson current*) tunnels through two superconducting materials, separated by a barrier (*Josephson Effect*). The

Josephson effects are the most unusual manifestation of the pair wave. They occur when two superconductors are in weak contact, e.g. by a constriction, an insulating tunneling barrier or a normal conducting barrier for the pairs. HTSCs junctions can be made by a grain boundary and there are “*intrinsic Josephson effects*” (IJE) when a current is forced normal to the CuO_2 layers [11] this is presented in Fig. 1.10.

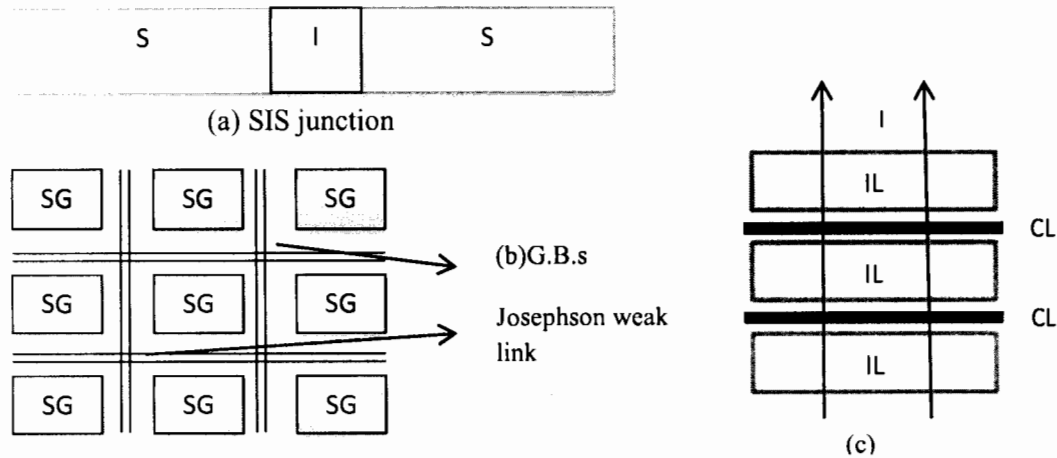


Fig. 1.10: Manifestation of Josephson Effect (a) SIS (b) Inter-grain coupling (c) Tunnelling between Cu planes.

1.9 Classification System to Describe Structure Types (Four Digits Naming Scheme)

Müller and Bednorz was the pioneer in creating a ceramic compound capable of superconducting at $30K$ [16]. There was a race for new material that conducts at room temperature. Then there was a break through at University of Alabama, they substituted Yttrium for Lanthanum in the Müller compound and achieved T_c , about $92K$. Since then it is known that all superconducting material are ceramic with chemical compounds mercuric-cuprates. The world record for high T_c is now held by mercuric-cuprates that are composed of Mercury, Thallium, Barium, Calcium, Copper, and Oxygen. Under extreme pressure its T_c can be improved.

The chemical formulas for High temperature superconductor are quite lengthy and complicated. In order to simplify the chemical formula, the *four-digit scheme* was coined. According to this system, “The first number tells the number of insulating layers between adjacent conducting blocks. The second tells the number of spacing layers between identical

CuO_2 blocks. Third gives the number of layers that separate adjacent CuO_2 planes within the conducting block and fourth gives the number of CuO_2 planes within a conducting block”.

1.10 Structure of HTSCs

In HTSCs, there are charge blocks and superconducting/active blocks. The charge block acts as a charge reservoir whereas, the other blocks, which usually are between the reservoirs, provide the path to the conducting electron. Its structure consists of $n = 1, 2, 3, \dots$ CuO_2 layers, these layers are on top of each other and in between these layer Ca layers are sandwiched $(CuO_2/Ca)_{n-1}CuO_2$ as shown in Fig. 1.11 [17-20]. The charge reservoir blocks consists of $EO/(AO_x)_m/EO$, where $m = 1, 2$ and AO_x ($A = (Bi, Tl, Hg, Cu)$) is monolayers oxides [21], (Pb, B, Al, Ga) [22], Au [23] Ca [24]; The HTSC's structure results from interchanging these stacks of block units.

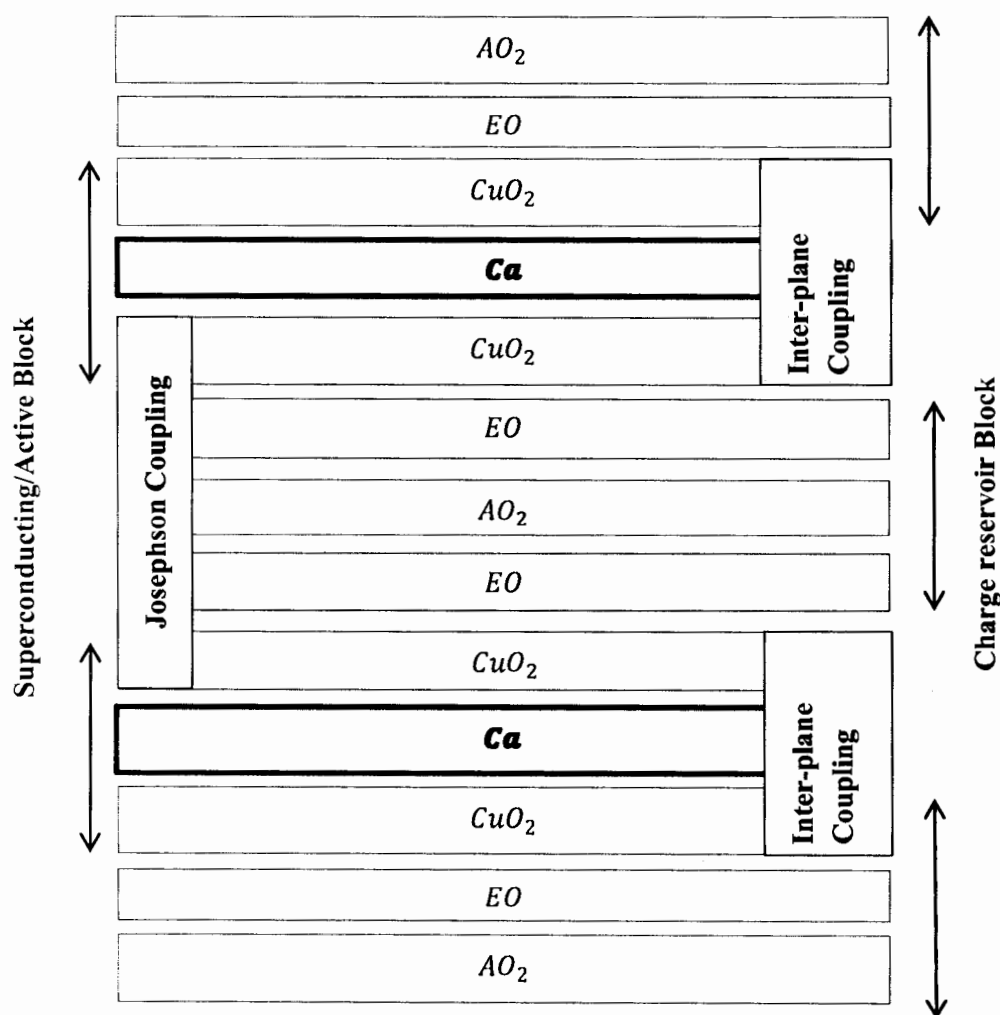


Fig. 1.11: General structure of a cuprates HTSC's $(A_m E_2 Ca_{n-1} Cu_n O_{2n+m+2+y})$ for $m = 1$. [25].

It is seen experimentally that for all HTSC's families the optimized T_c is found to increase from $n = 1$ to 4 and to decrease again for higher n . Therefore, there is a relation between T_c and the buckling angles of the CuO_2 layer [26]. Furthermore, it is seen that arrangement of AO_x layer results in deviations from tetragonal structure to another structure [27-29]. In understanding HTSC's it can be said that CuO_2 layers plays the major role in enhancing or reducing the critical temperature.

1.11 Material Imperfection

Material imperfection includes the phases which oppose the flow of super-current. Since, HTSC's materials are not homogeneous but it is a network of connected grains (see Fig. 1.12) which hinders the flow of current at various orientations. In the growth of crystal it is known that all the impurities and remnant of secondary phases are totally focused at the grain boundary and these boundaries hinders the flow super-current [38]. In order to eliminate these impurities, the crystal has to be grown carefully subject to the conditions.

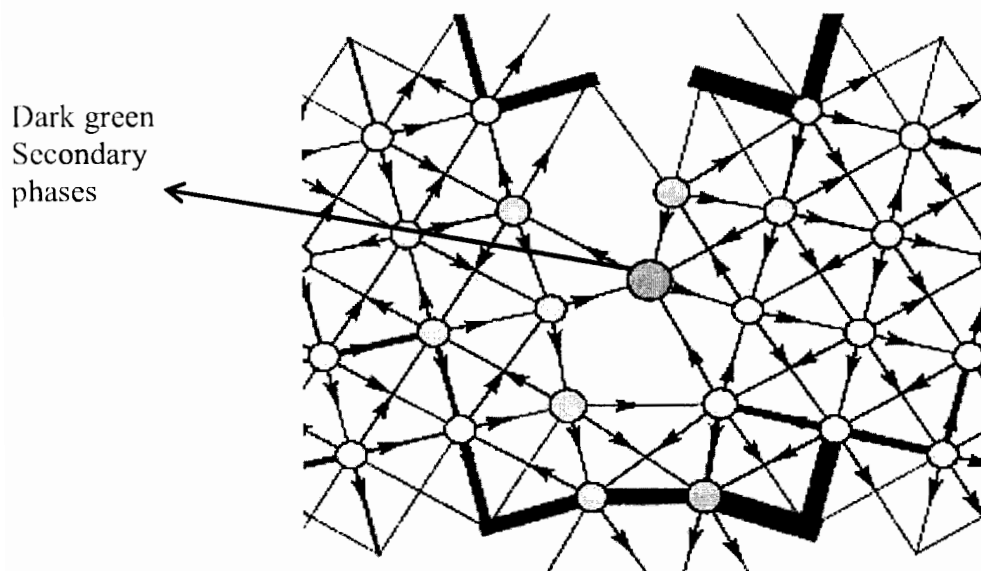


Fig. 1.12: The crystal boundary between two grains (HTSCs microstructure). The dark green dot indicates the secondary phases. Moreover, oxygen reduction can be controlled at grain boundaries [57].

Another hindrance for the flow of super-currents in HTSCs is the angle between the grains. It is seen, there is an exponential decrease of the super-current as a function of angle between the grains (see Fig. 1.13).

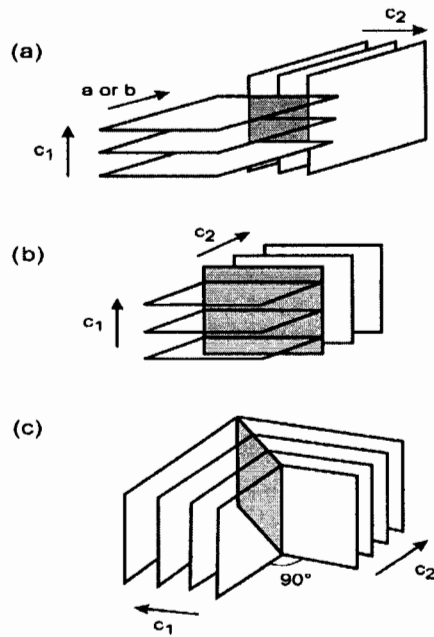


Fig. 1.13: Orientations of three types of grain boundaries (shaded region).

1.12 Phase Diagram

It has been observed experimentally that a relation between the critical temperature T_c and doping with substitution elements exists. The fluctuation of T_c can be described as a function of doping 'x', which can be shown by the phase diagram see Fig. 1.14 as “under-doped” and “over-doped” regions, respectively.

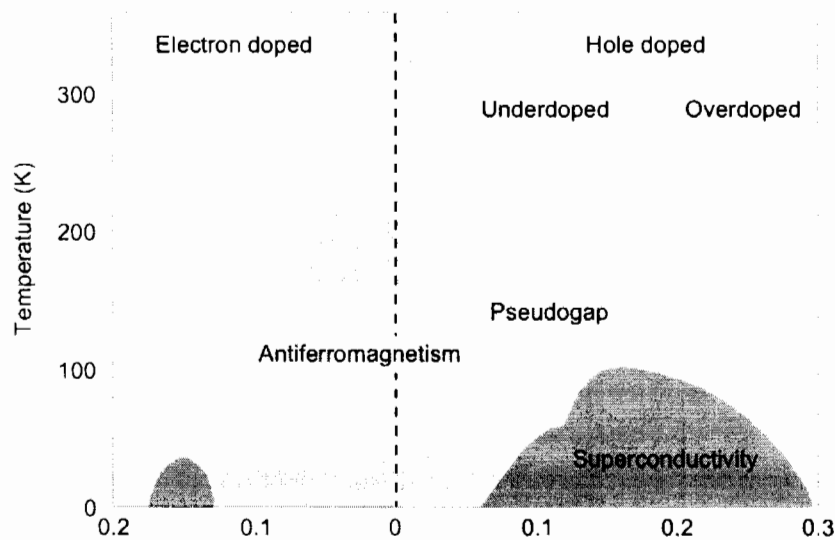


Fig. 1.14: Phase diagram of HTSCs. A competition exists between antiferromagnetic (AF) and superconductivity (SC) state. Pseudo-gap T^* is thought to be the precursor for superconducting state (SC).

The under-doped and over-doped region corresponds to the doping with substitution elements. It is believed that in HTSC's the phenomenon of superconductivity is due to the holes. As it can be seen from the diagram, when "holes" doping is increased, T_c decreases. There is a point between these domains where the properties of superconductor are optimum it is called the "optimum level" [39-45].

1.13 Discovery and Chemistry of Thallium-Barium-Calcium-Copper Oxide (TBCCO) System Superconductors

Thallium based superconductor $Tl-Ba-Cu-O$ system was experimentally discovered by *Sheng and Hermann* in October 1987. Initially during research their sample doesn't contain the elements Ca , and it was based on $Tl_2Ba_2Cu_3O_{8+x}$ and $TlBaCu_3O_{5.5+x}$ compounds. Surprisingly it showed zero resistance above 80K. When they added Ca to their samples the transition temperature reached to a remarkable 100K in $Tl-Ba-Ca-Cu-O$ system [46]. Then after wards, *Hazen et al.* and *Parkin et al.* went on to change the conditions under which thallium losses can be minimized and the involved cookery of different phases in sample to see which best shows the highest critical temperature. For example, they discovered the compound with significantly amount of $Tl_2Ba_2Ca_2Cu_3O_{10}$ phase and produced a material with bulk superconductivity at 125K. In $Tl-Ba-Ca-Cu-O$ related family and close resemblance to the perovskite structure ten well known structure have been found. These are and some of their unit cells structures are tabulated in Table 1.1 also the Fig. 1.15 depict different structures.

Table 1.1: Homologues series of Tl compounds.

$Tl_1Ba_2Cu_1O_5$ (Tl : 1201)	$Tl_1Ba_2Ca_1Cu_2O_7$ (Tl : 1212)	$TlBa_2Ca_2Cu_3O_9$ (Tl : 1223)
$Tl_1Ba_2Ca_3Cu_4O_{11}$ (Tl : 1234)	$Tl_1Ba_2Ca_4Cu_5O_{13}$ (Tl : 1245)	$Tl_1Ba_2Ca_5Cu_6O_{16}$ (Tl : 1256)
$Tl_2Ba_2Cu_1O_6$ (Tl : 2201)	$Tl_2Ba_2CaCu_2O_8$ (Tl : 2212)	$Tl_2Ba_2Ca_2Cu_3O_{10}$ (Tl : 2223)
$Tl_2Ba_2Ca_3Cu_4O_{12}$ (Tl : 2234)		

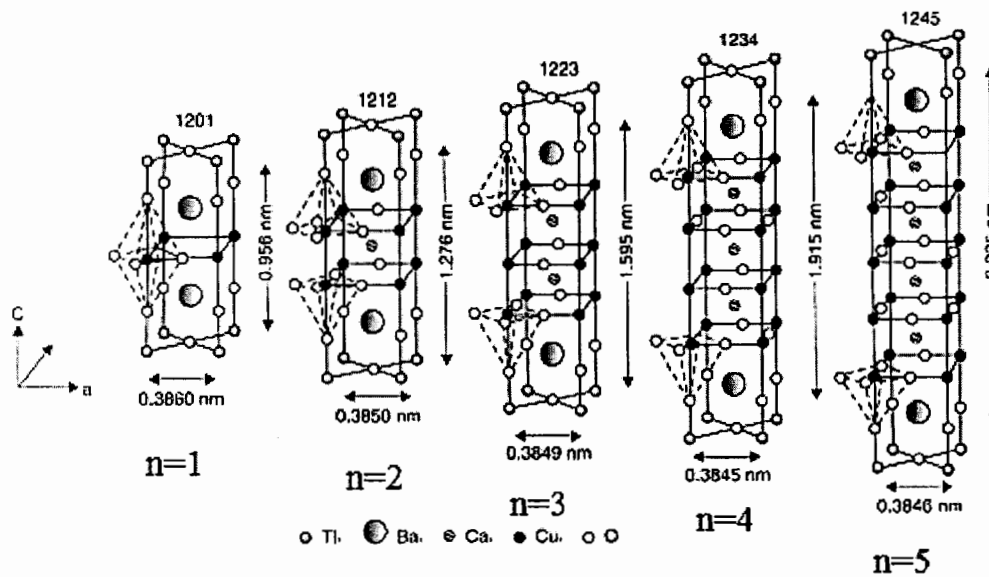


Fig. 1.15: Crystal structures of Tl based single-layer superconducting oxides for $TlBa_2Ca_{n-1}Cu_nO_{2(n+1)}$ ($n = 1 - 5$) family [37].

The crystal structures of these phases, which form the homologous series are represented by general formula $Tl_mBa_2Ca_{n-1}Cu_nO_{2(n+1)+m}$ where ($m = 1, 2$ and $n = 1 - 5$). All of these oxides have a tetragonal structure at room temperature. The oxides with $Tl-O$ single-layers have primitive tetragonal cells, whereas the oxides with $Tl-O$ double-layers have body-centered tetragonal cells.

In general, Tl based superconducting oxides can be considered to form oxygen deficient perovskite related structures [42]. The unit cell consists of alternation $nCu - O$ corner sharing square planar layers and single or double edge sharing $Tl - O$ octahedral layers. The edge shared $Tl - O$ octahedral are interconnected with $Cu - O$ square planar/square pyramidal layers. The Ba cations are located in the interstices of $Tl - O$ and $Cu - O$ slabs and the Ca ions are between the $Cu - O$ layers. The oxygen coordination number of Tl is 6, Cu is 4/5, Ca is 8, and Ca is 12 in single $Tl - O$ layered compounds. Two necessary but not sufficient-conditions for appearing high temperature superconductivity in the intergrowth copper oxides such as Tl family are:

- (i) Similar oxygen coordination at each Cu atom of a given concentration within a narrow range.
- (ii) Mixed valent CuO_2 planes having a mobile charge carrier concentration within a narrow range [30-34].

1.13.1 *CuTl*-based Superconductors

The two families of superconductors, $CuBa_2Ca_nCu_{n+1}$ and $TlBa_2Ca_nCu_{n+1}$ systems ($Cu - 12n(n + 1)$ and $Tl - 12n(n + 1)$ systems) have higher critical temperature. These compounds have a large anisotropy and same structure except for the position of oxygen atom in the charge reservoir layer. Since their discovery superconducting parameters has been studied extensively. Various substitutions of elements and controlling the amount of oxygen content also affect the superconducting parameters and assist to achieve the highest T_c . These compounds have large anisotropy and are not reliable. The substitution of Tl in $Cu - 12(n - 1)n$ compounds results of a new subfamily $Cu_{1-x}Tl_x - 12(n - 1)n$ compound, where $n = 2, 3, 4, 5 \dots$ [47]. As these compounds are easy to synthesize by single step method and have low anisotropy $\gamma = 5$, especially for the case $n = 3$ the charge distribution is homogenous in CuO_2 planes [48]. These compounds also shows high irreversibility H_{irr} and J_c . The structure of these derivatives of Tl compound consists of CuO_2 planes in the unit cell ranging from 1 to 5. If the number of CuO_2 planes is 3 the T_c increases, and decreases for $n > 4$. The $CuTl$ -based compounds has tetragonal structure with $P4/mmm$ space group and lattice constants $a = b = 4.37\text{\AA}$, $c = 14.82\text{\AA}$. Unit cell of $CuTl$ is depicted in Fig. 1.16.

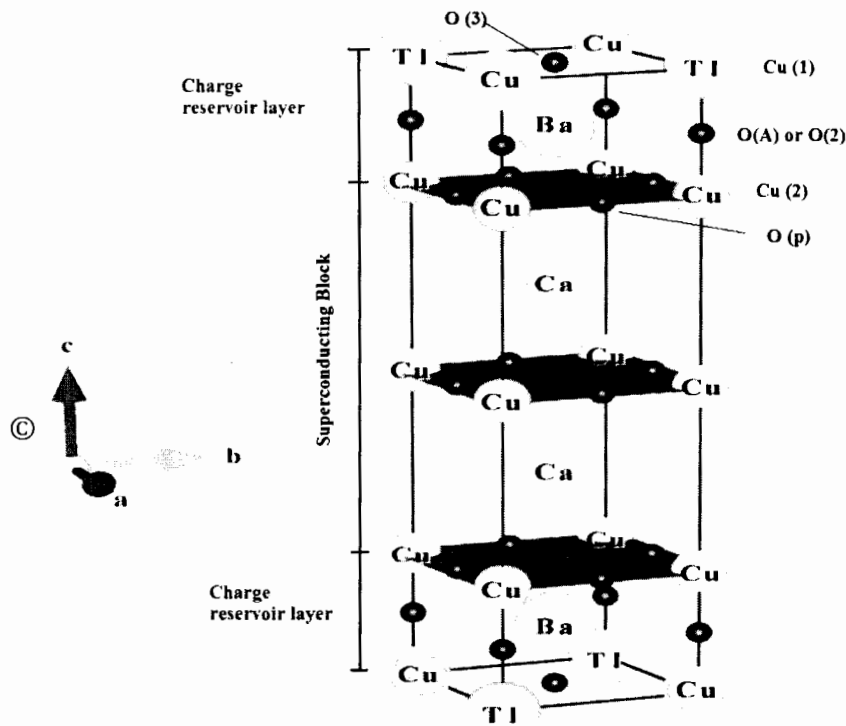


Fig. 1.16: Crystal structure of $CuTl$ – 1223 unit cell.

1.14 Effects of Oxygen Nonstoichiometric on Superconductivity

Oxygen nonstoichiometric is known to play an essential role in the geometric and electronic structure of high T_c superconducting cuprates. The oxygen is readily inserted into, or extracted from, the $Cu(1) - O(1)$ chains. The carrier's concentration and superconducting properties are essentially controlled by the oxygen content.

1.15 Nano-science

Nano science is the study of phenomenon and manipulation of materials at nano level where property differs from bulk materials for example; nano-structure at the nano level (Graphene, QD etc.) quantum effect starts to dominate, the electron transport behave like Dirac point. The crystal structure starts to change shape in such a way that it is not stable and this effect is seen in all nano-materials a low melting point and reduced lattice constant [35].

1.16 Types of Nano-structures

Different types of nanostructure which can be categorized as 1D (Dimension), 2D and 3D or 0D are shown in Fig.1.17. These dimensions can be said in different ways as confinement of flow electron. Broadly 2D structure includes thin films, quantum wells and super-lattice. 1D structure includes carbon nanotubes and its derivatives that is nano-wire, nano-rods and graphene. 0D structure includes quantum dots, Bucky-ball and fullerene. At small scale quantum phenomenon starts to play a dominant rule.

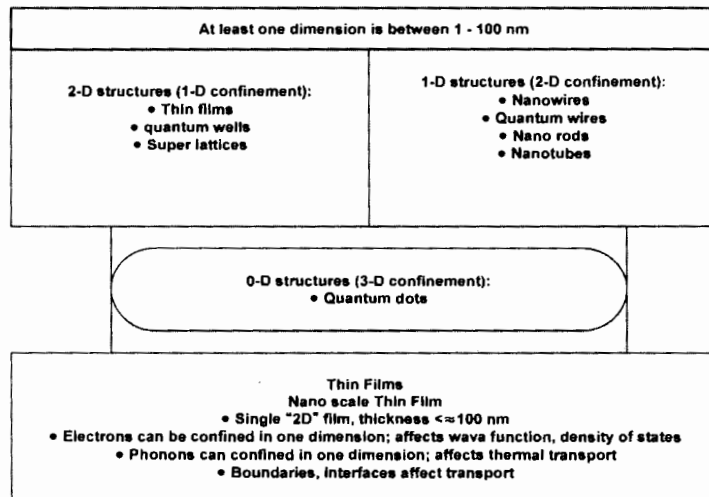


Fig. 1.17: Nano-structures broadly categorized as 1D, 2D and 3D.

1.17 Morphology of Nano-particle

In the assembly of nano-particle, small size is not the prerequisite. For any practical purposes, synthesis of nano-particle should be done thoroughly in an environment where the parameters can be controlled so as to achieve the following characteristics [35]

- (i). Uniformity in particles size.
- (ii). Consistent shape or morphology.
- (iii). Same chemical composition and crystal structure.
- (iv). No agglomeration.

1.18 Properties of Cupric oxide (CuO) Nano-particles

- (i) All anti-ferromagnetic nano-particles have net magnetic moment due to an imbalance of spins up and down at and near the surface. The transition metal monoxides MnO , FeO , CoO , NiO and CuO are all anti-ferromagnetic. The crystal structure of CuO nanoparticles is the same as that of bulk CuO if $< 17nm$. Figure 1.18 shows the crystal structure of CuO .
- (ii) CuO is unique among the monoxides having a monoclinic unit cell and coordination of copper-oxygen atoms.
- (iii) It is a p-type semiconductor.
- (iv) It shows a strong low-dimensional nature.
- (v) It has an indirect bandgap of charge transfer nature(1.21 – 1.5 eV).

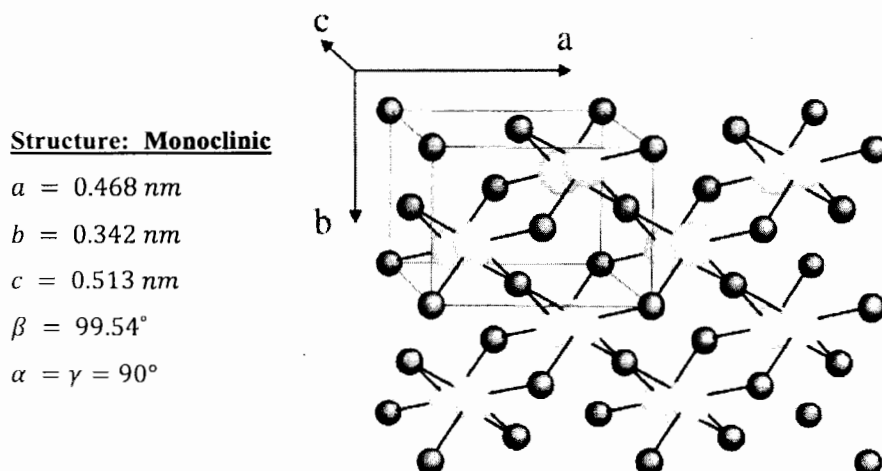


Fig. 1.18: A perspective view of the crystal structure of bulk CuO [36].

1.19 Small-Scale Superconductivity

It is a new branch of superconductivity where research is being done on the nano-scale. In this branch, HTSC superconductors are scaled down to a nano range and the resistance is measured along with other parameters. Experiments are being done on CNTs and have been verified that superconductivity still exists [37].

Chapter 2

THEORY OF FIC AND LITERATURE REVIEW

2.1 Fluctuation Induced Conductivity (FIC)

In 1960, Ginzburg numerically, calculated the fluctuation contribution to the heat capacity of superconductor in the vicinity of T_c . Near and above the transition region fluctuation increases the heat capacity which is already present above the transition temperature. This was the new confirmation to the theoretical understanding of superconductivity. Ginzburg-Landau macroscopic theory of second order phase requires the assumption of fluctuations to increase the heat capacity at T_c which was in agreement with the theoretical predictions. He estimated the corrections of fluctuations in Type-I superconductor (in bulk as well as clean) which becomes significant in the temperature regime,

$$\frac{\Delta T}{T_c} \sim \left[\frac{(T_c)^4}{\epsilon f} \right] \sim \left[\frac{(a)^4}{\xi} \right] \sim 10^{-14} \text{ to } 10^{-16} \quad (2.1)$$

Where 'a' is the inter-atomic distance and 'ξ' is the coherence length. These extremely small values explain why for a long time, the fluctuation phenomenon was considered isolated to experimental study in superconductors. Superconductor is composed of different layers which are stacked on one another, this layering hinders the property of superconductivity, which makes them anisotropic. Due to large anisotropy (the normal and superconducting-state) fluctuations in the "order-parameter" stimulates the effect on Cooper pairs where the transports of pairs are compelled to travel along c-axis and ab-plane with rivalry along the major axis.

The resistivity $\rho(T)$ versus temperature T curve illustrates a bending of a curve from linear state to a non-linear state. The bending of curve is mainly due to the superconducting fluctuations present above the critical region. The fluctuation induced in this region can be approximated by,

$$\Delta\sigma(T) = \frac{1}{\rho} - \frac{1}{\rho_n} = \frac{\sigma_N(T) - \sigma(T)}{\sigma_N(T)\sigma(T)} \quad (2.2)$$

Where $\rho(T) = 1/\sigma(T)$ is the actually measured resistivity, $\rho_N(T) = 1/\sigma_N(T) = \alpha + \beta T$ is the extrapolated normal state resistivity and β the gradient of the extrapolated curve. For the excess conductivity analysis $\Delta\sigma(T)$ we usually resort to some theoretical models to extract the parameter which cause the conductivity. The models are Aslamazov-Larkin (AL) and Lawrence-Donaich (LD) models; this contribution arises from excess current carried by fluctuation-created Cooper pairs above T_c [49]. The rest of indirect contribution is due to Maki-Thompson (MT) which reveals the effect of fluctuation on the “normal electrons” [50]. Since HTSC’s are layered structure which is the main hurdle for the transport of cooper pairs or in some sense d-wave pairing along the c -axis. Lawrence-Doniach (LD) model [51] predicted that a crossover from three dimensional (3D) electronic state of the system to a two dimensional (2D) one with increasing temperature must exist. FIC analysis provides the simple tool to get information at the micro level about $\xi_c(T)$, t_ϕ and dimensionality of the electronic system of the superconductor and to see the congruency with the predicted models. Explanation of different section of resistivity $\rho(T)$ versus temperature T curve as explained by different models is shown in Fig. 2.1.

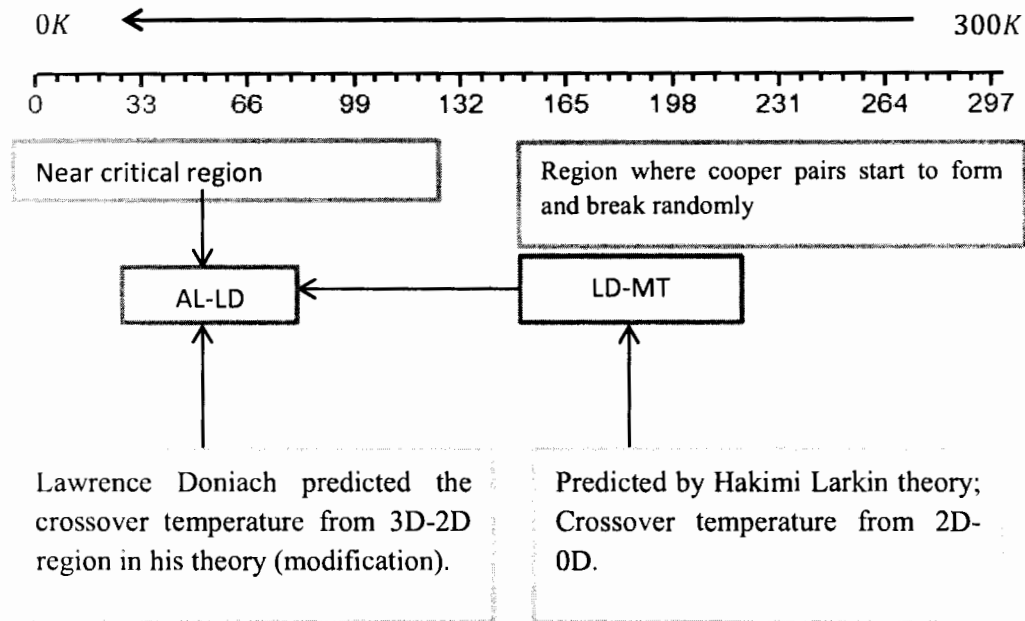


Fig. 2.1: Schematic representation of FIC theory. The AL term dominates close to T_c whereas; the MT term is related to the 2D region, where the formation of normal electrons starts to form or moderate pair-breaking and corresponding to this the phase-relaxation time t_ϕ of the normal electron [52].

2.2 Mean Field Theory (MFT)

It is an approximation theory which is used to simplify the interaction between many body problems in particular the phase transition. MFT is used in super-fluidity, superconductivity and in Bose-Einstein condensations (BEC) to simplify the interaction between the particles, and observe solely how a particular particle can affect other particles in its immediate locality [53]. MFT is based on the following assumptions which are,

- (i) A dense portion of particles in one region of the state inclines to influence other particles, resulting into the flow from low region to a high concentrated region.
- (ii) A low density region causes the neighbouring regions to have density lower as compared to usual state.

2.3 Literature Review

M. Farbod *et al.* [54] prepared the silver (*Ag*) nano-particles in an alcohol solution. They found that the particle size could be controlled by aging the solution. The superconducting bulk samples were doped by *Ag* nano-particles with different sizes and concentrations. The results showed that the J_c increases monotonically by increasing of *Ag* nano-particles size up to 700 nm. Also J_c is greater for samples with higher *Ag* concentration. The enhancement of critical current density is attributed to the improvement of link between the grains and better crystallization of the grains.

M. Annabi *et al.* [55] examined the effects of Al_2O_3 nano-particles doping in (*Bi, Pb*) – 2223 superconductor. The additions of large amount of Al_2O_3 nano-particles reduce (*Bi, Pb*) – 2223 phase formation and also decreased current density. The small amount of Al_2O_3 nano-particles within superconducting grains produced defects such as dislocations and stacking faults, which also enhanced the flux pinning and critical current density.

M. M. Eloker *et al.* [56] examined the effect of doped *ZnO* nano-particles on the physical properties of bulk sample, $(Cu_{0.5}Tl_{0.5}Pb_{0.25})Ba_2Ca_2Cu_3O_{10-\delta}$. Co-precipitation method was used to synthesize *ZnO* nano-particle. They added *ZnO* nanoparticle by percentage of weight to the $(Cu_{0.5}Tl_{0.5}Pb_{0.25})-1223$. XRD Analysis showed that nanoparticle of *ZnO* have a wurtzite structure with crystallite size of about 35.4nm. Particle size analyser results showed that powder has a particle size of about 23.7nm with ranging from 1nm to 120nm. XRD pattern shows superconducting phase with tetragonal structure

and $P4/mmm$ symmetry few peaks of (Cu,Tl) -1212, $Ba_2Cu_3O_6$ and $BaCuO_2$ were observed. No peak corresponding to ZnO or Zn based compound was observed for all prepared samples. The percentage of volume fraction and melting point of the major $(Cu_{0.5}Tl_{0.5}Pb_{0.25})$ -1223, is found to increase up to $y = 0.8$ wt. % resulting into increase in T_c and J_c . However, the grain boundary resistance reduced. Further increase in above 0.8 wt. % reduced the volume fraction, melting point and T_c and J_c and increase grain boundary resistance. EDXA (energy dispersive X-ray Analysis) of $(ZnO)_y(Cu_{0.5}Tl_{0.5}Pb_{0.25})Ba_2Ca_2Cu_3O_{10-\delta}$ with $y = 0.8$ wt. % indicates that Nano particle of ZnO just occupy the interstitial places between the grains, whereas low concentration provide ($y < 0.8$ wt. %) strong pinning and high concentration provide ($y > 0.8$ wt. %) induced large agglomeration between the superconducting grains.

S. Graser *et al.* [57] studied the effects of grain boundary on the super-currents in HTSCs. They modelled the grain boundary of bulk sample of YBCO using Molecular Dynamics (MD). They calculated the tight binding Hamiltonian model for the d-wave SC, from their analyses the results were with the orientation of boundary angle the critical current density decay exponentially. The parameters, which they fitted to their model, were obtained from the reference mentioned in their paper. Their findings suggested that the cause for the dependence on the disorientation of the angle is the build-up of charge near the defects.

N. H. Muhammad *et al.* [58] examined the mechanical properties of SnO_2 nanoparticles doped $(Cu_{0.5}Tl_{0.5})$ -1223 superconductor. They prepared this sample $(Cu_{0.5}Tl_{0.5})$ -1223 by solid state reaction method. Nano-particles of SnO_2 with wt. % from 0.0 to 1.0 wt. % was added to the shifted powder. XRD analysis of $(SnO_2)_pCu_{0.5}Tl_{0.5}Ba_2Ca_2Cu_3O_{10-\delta}$, where p is 0.0, 0.1, 0.6 and 1.0 wt. % samples shows the tetragonal structure of $(Cu_{0.5}Tl_{0.5})$ - 1223 and few peaks of secondary phases for instance (Cu,Tl) - 1212 and $BaCuO_2$. There was no peaks related to SnO or Sn based compound in the XRD analysis. From the XRD analysis the volume fraction calculation indicates that the percentage of main phase $(Cu_{0.5}Tl_{0.5})$ - 1223 increases up to 0.6 wt. % beyond that superconducting grains starts to shrinking. EDXA of $(SnO_2)_pCu_{0.5}Tl_{0.5}Ba_2Ca_2Cu_3O_{10-\delta}$ with $p = 0.2$ wt. % showed that SnO_2 nanoparticle just sits between the grains i.e., occupies between the superconducting grains. Porosity decreases with SnO_2 nanoparticle addition. SEM micrographs showed the formation of elongated grains it increases from $p = 0.0$ to 0.4 wt. %. Small amount of nanoparticle of SnO_2 connects the $(Cu_{0.5}Tl_{0.5})$ -1223 grains. The spherical nano-particle observed at

$p = 0.4$ wt. % sits between the $(Cu_{0.5}Tl_{0.5})-1223$ grains which indicates that they maintain their separate identity after the sintering process. Micro hardness of $(Cu_{0.5}Tl_{0.5})-1223$ phase increased gradually with nano particle SnO_2 addition and with load up to 1.96N micro hardness values decreases.

A. A. Khurram *et al.* [59] examined excess conductivity of $Cu_{0.5}Tl_{0.5}Ba_2Ca_1Cu_2O_{8-\delta}$ thin films by Aslamazov-Larkin (AL) model. They showed through FIC that variation of oxygen in the charge reservoir layer alter the dimensional constant. They observe, samples post-annealed in nitrogen have higher $T_c(0)$ whereas; samples post-annealed in oxygen have smaller $T_c(0)$. They reasoned, the cause of dimensional fluctuation was due to two reasons; one was the intra grain and the second was the nature of the grain boundary and size. They concluded that optimum carrier concentration enhanced the critical temperature to higher values.

I. A. Ansari *et al.* [60] studies the MgB_2 properties. They doped ZnO and Al_2O_3 nano particle separately in MgB_2 superconductor phase. Their XRD analysis revealed the hexagonal structure belonging to the space group P6/mmm. Al substitution resulted in a decrease in T_c . They synthesized nano- Al_2O_3 doped $Mg_{1-x}Al_xB_2$ (where $x = 0\%, 2\%, 4\%$ and 6%) and nano- ZnO doped $Mg_{1-x}Al_xB_2$ ($x = 0\%, 2\%, 4\%$ and 6%), separately. In case of Al_2O_3 doped $Mg_{1-x}Al_xB_2$ superconducting parameters were seems to decrease with increasing doping level. J_c value were found to be increased for all temperatures and higher magnetic fields. At $x = 2\%$ the sample exhibited the excellent J_c-H properties. The irreversibility line H_{irr} and J_c were systematically enhanced by doping nano-alumina. SEM analysis reveals the trivial improvement of flux pinning at various temperatures and magnetic fields. Lattice parameter was observed to decrease, which indicates Zn is substituted at Mg site and with increase doping of ZnO nano-particle, T_c reduces. Higher J_c was found when the sample with $x = 2\%$ ($Mg_{1-x}Al_xB_2$) was doped. With increasing magnetic field, fluctuation induced conductivity (FIC) parameters, T_c and T_c^{mf} , were analysed near transition temperature of polycrystalline MgB_2 superconductor, and found to be decreasing. For FIC analysis, they used Aslamazov-Larkin (AL) model.

P. K. Nayak *et al.* [61] examined the original and doping of Ag in $(La_{1-x}Y_x)_2Ba_2CaCu_5O_z$ superconductor and analyse the excess conductivity in the Para-coherence region. Analysis of this compound, pure and doped with 5 wt. %, was made in the vacuuous and proximity of 1T magnetics field. With no magnetic field the material showed the fluctuation from an ordered state to a disordered state. For Ag doped samples, disordered

fluctuations were at various ranges of temperature. They observed that with the increase in doping level the host matrix begins to shrink. In the presence of magnetic field the more ordered phase was observed which was attributed to the intra-granular interaction. The conclusion of their results suggested that dimensional exponent matched to the $YBa_2Cu_3O_7$ (YBCO) sample.

Gingasu *et al.* [62] prepared copper ferrites nano-particle with tetragonal structure by two chemical methods. One is Self-propagating combustion method and the other is Complexion method. For preparation by these methods the precursor materials were polynuclear. The copper ferrites were characterized by X-ray diffraction, Infrared spectroscopy, UV-visible spectroscopy, and magnetic measurements. The data recorded for magnetization versus temperature (H/T) were 43.5 emu/g and 21.5 emu/g .

P. K. Khanna *et al.* [63] prepared and characterize copper nanoparticles by using hydrazine hydrate (HH) and sodium formaldehyde-sulfoxylate (SFS). Characterization by UV-visible absorption spectroscopy revealed that HH and SFS have absorption about 600nm due to surface plasmon resonance (SPR). Copper nanoparticle prepared by HH method reveals, the size of nanoparticles distribution at wide spectrum. Whereas nano-composites prepared with the use of SFS have shown improved particles size distribution. X-ray diffraction analysis of powder prepared with the use of carboxylates confirmed the metallic copper formation in the end product. Crystallite size calculated to be 30 nm by use of Scherrer equation.

K. Singh *et al.* [64] examined the effects of Cu doping in MgB_2 superconductor at different temperatures. They prepared the superconducting samples in argon atmosphere with a controlled temperature ranging from $800\text{--}900^\circ\text{C}$. They characterize the sample through different techniques that is X-ray diffraction (XRD) and Scanning Electron Microscopy (SEM). The XRD analysis of $Mg_{1-x}Cu_xB_2$ revealed single nature of the sample prepared at 850°C with $x = 0.05$ and Cu doping doesn't affect the transition temperature. SEM analysis reveals grains were compressed with a size of $1\mu\text{m}$.

J. Zhu *et al.* [65] prepared the CuO nanoparticle by the co precipitation method. The result showed that the as-prepared CuO nanoparticle have narrow size distribution. Average size of CuO nanoparticle is expected by Scherer equation to be 6 nm . TEM image of the as-prepared CuO nano particle showed the spherical particles with high dispersion.

S. X. Dou *et al.* [66] studies the effect of CNTs doping on J_c of MgB_2 superconductors. Their analysis reveals that the flux pinning was improved but T_c was seems

to decrease. The optimal doping level were $y = 0.05$ (2.5% of B). While this level increased to $y = 0.2$ (10% of B) for CNTs doping. The doping effect overall, increases the J_c twice the original. The results were 8T and 5K and 7T and 10K. J_c was more than 10,000 A/cm² at 20K for 4T and 5K for 8.5T respectively.

G. Hammerl *et al.* [67] studied the properties of high temperature polycrystalline material. They have tried to resolve some issue regarding the hindrance from grain boundary from the application point of view. In their study, they propose the design to coat the conductor at micro-level also the alignment of the grains within few degrees and suitability of doping for enhancing the critical current. They analyse the density of grains versus the critical current of conductors, by mouse algorithms, considering the simulation of 10⁴ to 10⁶ grains. Results by the simulation indicate critical current increases linearly with the increase of grains density.

Z. Y. Jia *et al.* [68] studied how to pin down the flux from application point of view. They artificially introduced nanometre-sized ZrO_2 to bulk Pb -doped Bi-2223 HTSC. They prepared this sample by solid-state reaction method; y mol.% nano particles of ZrO_2 with size of 10nm were introduced into $Bi_{1.8}Pb_{0.4}Sr_2Ca_{2.2}Cu_3O_{10+\delta}$ (where $y = 0, 5, 10, 20, 30$ and 50 mole %). XRD analysis showed that Bi – 2223 phase formed contain few peaks of Bi – 2212 and other non-superconducting phases and these non-superconducting phases serve as pinning centres. From the XRD analysis peaks of ZrO_2 were not observed. The increase in the doping level triggers the reduction of T_c^{onset} . Whereas, critical current density, J_c , shows the enhancement in the presence of magnetic field. SEM studies nanoparticles ZrO_2 dispersed homogenously in Bi – 2223 matrices. EDXS showed there were 50 to 100nm features containing Zr with traces of Sr and Cu from the BSCCO matrix.

F. Fedirici *et al.* [69] examined the crossover temperature between Aslamazov-Larkin (AL) and short-wavelength fluctuation (SWF) regions in HTSCs experiments. They analysed Para-conductivity measurements in three HTSCs first is the melt textured $YBa_2Cu_3O_7$ sample, second one is the $Bi_2Sr_2CaCu_2O_8$ epitaxial thick film thirdly, highly textured $Bi_2Sr_2Ca_2Cu_3O_{10}$ tape. Crossover temperature were analysed in different temperature regimes in the state of Para-conductivity. It was noticed LD crossover shifts from lower to higher temperatures with the decreases in anisotropy of the compound. They observed that all the samples shows this behaviour $= \ln(T/T_c) > 0.23$, all the curves bend down according to the l/ϵ^3 law.

Y. Jia *et al.* [70] prepared *Co/Cu* nano-particles in hydrazine solution of copper chloride and cobalt chloride by a sono-chemical method for the formation of FCC cobalt structure.

R. Awad [71] investigated the doping of *MgO* nano-particles on the electrical and mechanical particles of $Cu_{0.25}Tl_{0.75}Ba_2Ca_3Cu_4O_{12-\delta}$ ($Cu_{0.25}Tl_{0.75}$)-1234 superconductor. The superconducting $(MgO)_x Cu_{0.25}Tl_{0.75}Ba_2Ca_3Cu_4O_{12-\delta}$ samples with various concentrations of *MgO* nano-particles (i.e. $x = 0.0, 0.2, 0.4, 0.6$ and 1.0 wt.%) were created by a single step solid-state reaction method. The *MgO* nanoparticles in the size range of $40 - 60$ nm were added by simple mixing and grinding. XRD analysis shows the dominant phase of $(Cu_{0.25}Tl_{0.75})-1234$ along with few peaks of other phases. SEM studies show *MgO* nano-particles sits between the grains. The addition of *MgO* nano-particles up to $x = 0.6$ wt. % upgraded the formation of phase, grain-link, transport critical current density and micro hardness. However, with increase in concentration it decreases the grain connectivity, phase formation, micro hardness and critical current density but the secondary faces helps to act as pinning centres with the increase in J_c

L. B. Ioffe *et al.* [72] analysed the normal state conductivity of polycrystalline *Hg - 1223* superconductor under different hydrostatic pressures. They discovered that with increasing pressure linearly cross-over and mean field critical temperature increases. Their results showed that increasing the pressure on the sample, the adjacent CuO_2 planes, starts to close up as a result coherence length and coupling strength J starts to increases.

Zhao *et al.* [73] examined the doping of *Ti* nano-particles in *MgB₂* bulk superconductor improves J_c , which was due to improved connections established between grains during sintering process. Zhao and Cheng have also examined the doping effect on J_c in YBCO bulk superconductor [74] and found noteworthy improvement in J_c by doping of *Ag* at grain boundaries.

L. G. Aslamazov *et al.* [75] analysed the fluctuation effect on the conductivity of normal electrons. Theoretically they found the effect of fluctuation pairing on the conductivity of a normal film, the governing equation which they derived fits very well with experimental data

TH 9334

2.4 Motivation

The motivation for the present study is to see the effect of doping oxide nanoparticle in $CuTl - 1223$ superconductor. In our work, we have taken $CuTl - 1223$ superconductor and doped CuO nanoparticle. The doped nano-particle has become a novel approach in the area of advanced research in superconductivity. The inclusion of nano-particle is one of the methods to create magnetic flux pinning centres. The efficient pinning centres improve the superconducting properties such as J_c , H_c , H_{irr} etc. The synthesis of particle at nano-scale has unusual properties; their surface to volume ratio becomes important in determining the physical properties at low temperatures. We have intended to analyse the doping effect of oxides nano-particle (CuO) on $CuTl - 1223$ superconductor. Since, these are polycrystalline ceramic materials; and have defects such as planar faults, dislocations, and grain boundaries. These defects occur due to synthesis process or impurities present due to different compounds. In order to heal the gaps, nano-particles fills the voids between the grains as a result enhances the flux pinning centres, connectivity between the superconducting grains and critical current density J_c , since these are two limitations of HTSCs.

In this work, we have carried out FIC (fluctuation-induced conductivity) analysis on resistivity versus temperature data. The parameters that is coherence length, inter-plane coupling, grain coupling were extracted above the transition region using Aslamazov-Larkin (AL) and Lawrence-Donaich (LD) model. Since these theories are applicable to single crystals. However, for the approximation case we still resort to the AL and LD equation for their simplicity. Since these models helps us to see microscopically what is happening in the critical region. The parameters qualitatively describe the effect of doped nano-particles, above the transition temperature. The results obtained through this study will be compared, analysed with existing literature and experimental outcomes

Chapter 3

SYNTHESIS AND EXPERIMENTAL TECHNIQUES

3.1 Synthesis Techniques

3.1.1 Solid State reaction method

(i) One-step method

The most straightforward synthesis method is to calcine the starting powder mixture containing the elemental oxides in one step to form the Tl based superconductive oxides. Alkaline earth metal dioxides, such as BaO_2 and CaO_2 , are often employed to replace the corresponding monoxides as the starting ingredients because the dioxides are less hygroscopic and easier to handle.

(ii) Multi-step method

The multi-step method is a process in which the synthesis of the desired superconductive phase is achieved through a series of calcination steps conducted at different temperatures. The required starting ingredients are either mixed all together at the very beginning of the first calcination step or introduced separately between consecutive calcination steps. The advantage of multistep method is the reduction in the Tl loss, same consistency and melting of powder to less extent.

For the synthesis of Tl based superconductive oxides, the multi-step approach was first developed in the processes in which alkaline earth metal carbonates, rather than oxides, were employed as the starting ingredients. The carbonates are frequently employed in the synthesis of high T_c superconductors because of their superior chemical stabilities, which allow easier handling and storage, to those of oxides. Decomposition of these carbonates, however, is slow even above $900^\circ C$ [76]. To reduce the Tl loss caused by excessive heat treatment when carbonates are used, the complete solid reaction has often been divided into two stages: a pre-calcination of a mixture containing CuO and alkaline earth metal carbonates above $900^\circ C$ in the first stage and a subsequent reaction of the resulted oxide mixture with a

Tl_2O_3 at a lower temperature in the second stage. The fact that for calcinations conducted at temperatures above $860^\circ C$, the single $Tl - O$ layer compounds are not formed until significant Tl loss takes place suggests that these compounds may not be thermodynamically stable for the compositions corresponding to their stoichiometry's but stable only under Tl -deficient situations. That is the single phase powders of these compounds cannot be synthesized from stoichiometric reactant powders at these temperatures. One possible cause for such instability is the incongruent melting.

3.2 Techniques to synthesize Nano-particle

There are different techniques to synthesize nano-particles like Co-precipitation and Sol-gel method but in our work we have opted Co-precipitation method.

3.2.1 Co-precipitation method

Co-precipitation is a wet chemical synthesis method. During the reaction different process starts simultaneously for the growth of nano-particle for example, nucleation, growth, coarsening, and agglomeration process [77] because, of this reason they have uniform size distribution and on average are less scattered [78]. The main advantages of Co-precipitation are,

- (i) Greater homogeneity
- (ii) Nano particle size distribution
- (iii) High purity, no grinding
- (iv) Greater reactivity
- (v) Low cost as compared to other methods.

3.3 Sample preparation

3.3.1 Synthesis of $(Cu, Tl) - 1223$ Superconductor

Solid-state reaction method was used to prepare bulk superconductor $Cu_{0.5}Tl_{0.5}Ba_2Ca_2Cu_3O_{10-\delta}$ with a mixture of $Ba(NO_3)_2$, $Ca(NO_3)_2$, $Cu(CN)$ and Tl_2O_3 compounds. During the formation, CuO nano-particles were added in order 0%, 10%, 15% and 20% for the formation of bulk superconductor, the compounds were mixed by the

stoichiometric formula, after synthesis it was grinded. $Cu_{0.5}Tl_{0.5}Ba_2Ca_2Cu_3O_{10-\delta}$, precursor material was synthesized using $Ba(NO_3)_2$, $Ca(NO_3)_2$, $Cu(CN)$ as starting compounds. These compounds were mixed in appropriate ratios in an agate mortar and pestle. Flowchart of preparation of $CuTl - 1223$ superconductor sample is shown in Fig. 3.1.

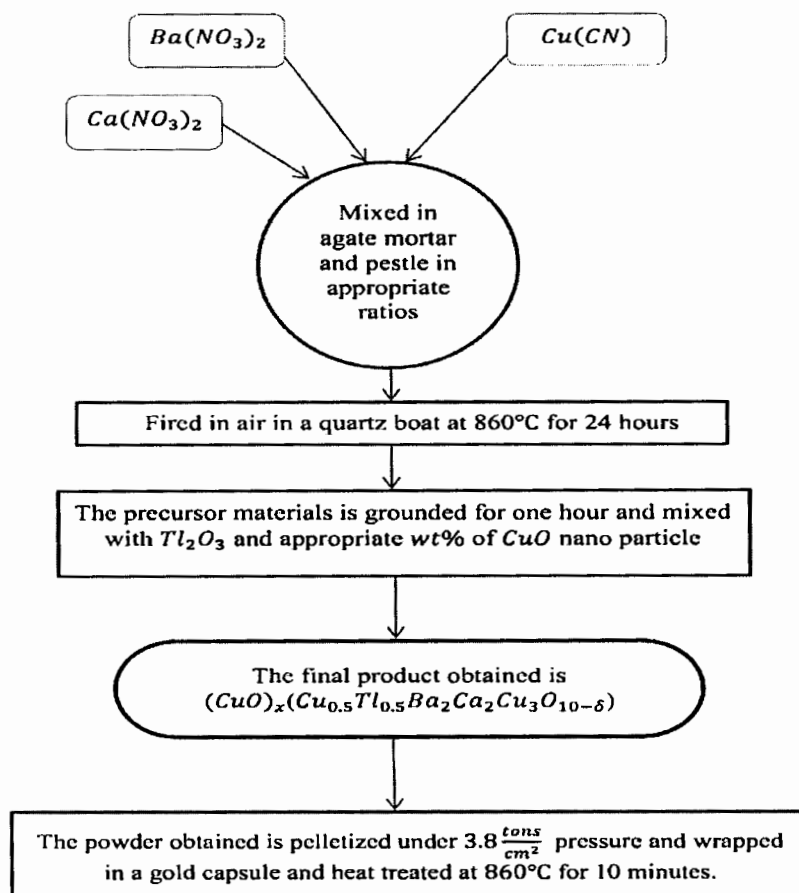


Fig. 3.1: Flow chart for preparation of HTSC sample.

The created sample was mixed thoroughly and placed in a quartz boat in a furnace at 860°C for 24 hours then it was cooled down to room temperature slowly. The precursor materials was then grinded for one hour and mixed with Tl_2O_3 (99%, Merck) and appropriate wt. % of CuO nano-particle to give $(CuO)_x(Cu_{0.5}Tl_{0.5}Ba_2Ca_2Cu_3O_{10-\delta})$ where $x = 0, 10, 15, 20\%$, as final reactants composition. The powder obtained was pelletized under 3.8 tons/cm^2 pressure and was enfolded in a layer of gold sheet because during the sintering process thallium is vulnerable to react. In the next process, the fresh pellet was set aside in a preheated furnace, which was kept at 860°C for 10 minutes. After heat treatment it was allowed to quench to room temperature.

3.3.2 Synthesis of *CuO* nano-particles

The synthesis of *CuO* nano-particles was carried out by Co-precipitation method. The chemicals $Cu(NO_3)_2 \cdot 3H_2O$, HNO_3 and $NaOH$ were used for preparation of *CuO* nano-particles. The aqueous solution of $Cu(NO_3)_2 \cdot 3H_2O$ and 2M HNO_3 was stirred for 5 minutes and then 1M $NaOH$ was added drop wise along with continuous stirring at room temperature. After 2 hours continuous stirring at room temperature precipitation was started and the pH of final solution was nearly 13. The precipitates were collected, washed with distilled water and dried at 100°C for 24 hours. The dried powder was calcinated at 200°C for 5 hours in oven to obtain required *CuO* nano-particles.

In our work we determined the structure of the material by XRD test (*D/Max III C* Rigaku with a CuK_α source of wavelength 1.54056 Å) and cell parameters by a software program. The compositional analysis was performed using energy dispersive X-ray (EDX) spectroscopy by JOEL Jed-2300, and the morphology of the material was studied through scanning electron microscopy (SEM). Dc-resistivity measurements were taken by four probe method and the value of current during the measurements was kept at 1mA. Resistivity measurements were taken from 77K to room temperature i.e. nearly 300K. The rate of heating was kept 1K/min to 3K/min during these measurements. The microscopic parameters {i.e. zero temperature coherence length along *c*-axis (ξ_c), critical constants (λ), inter-layer coupling constant (J), etc.} have been calculated from the FIC analysis on resistivity versus temperature curves.

3.4 Characterization techniques:

- X-ray diffraction (XRD)
- Scanning electron microscope (SEM)
- Energy dispersive X-ray analysis (EDX)
- DC-electrical resistivity measurements

3.4.1 X-ray Diffraction

It is used to analyze the crystalline structure of a sample and to measure the lattice parameters. X-ray usually has wavelength in the range (0.5Å – 2.5Å) which is equivalent to the spacing between the atomic planes in solids. When it falls on the sample the reflected

wave interfere constructively or destructively according to the spacing between the planes. Generation of X-ray takes place from the K-shell transitions and this is used for the diffraction analysis. Figure 3.2 shows X-ray of wavelength ' λ ' which are in phase is incident on a crystalline material.

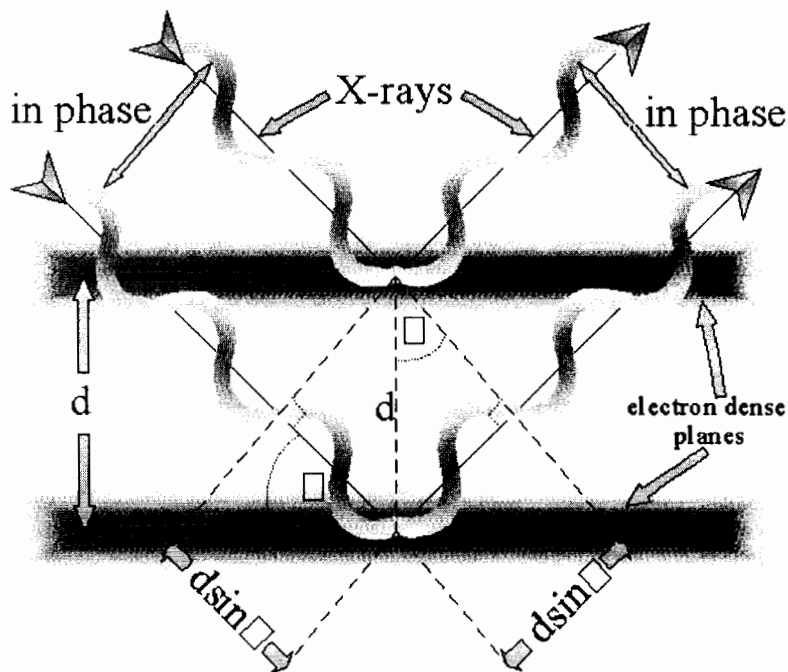


Fig. 3.2: Diffraction of X-rays from crystal planes.

The spacing between the material is ' d '. The rays will interfere constructively when the resulting waves are in phase.

$$2d\sin\theta = n\lambda, \quad (3.1)$$

where $n = 0, 1, 2 \dots$ is the order of diffraction. The above equation is known as Bragg's law and the waves which are satisfied by this law will give diffraction pattern of the sample. This technique can be used for finding the lattice parameters, atomic position and degree of crystallinity [80, 81]. Now we discuss the powder method,

The powder method includes the target X-rays of fixed wavelength and in the path of ray a sample is placed which is varied through θ and d . The peaks are observed for those values which are satisfied by Bragg's equation. We have in our case employed this method because superconducting sample is polycrystalline. From this analysis we can measure the diffraction angles, the spacing of planes, and the unit cell dimensions [82]. The Sherrer

equation relates peak width to crystalline domain size (analysis of crystallite size), through this equation,

$$l = \frac{k \lambda}{B_{size}(2\theta) \cos \theta} \quad (3.2)$$

Where l is particle size, λ , θ and B are the wavelength of X -ray radiation, diffraction angle of the reflection and FWHM, respectively. Sherrer constant k depend on crystal shape. The schematic diagram of an X -ray diffractometer is shown in Fig. 3.3.

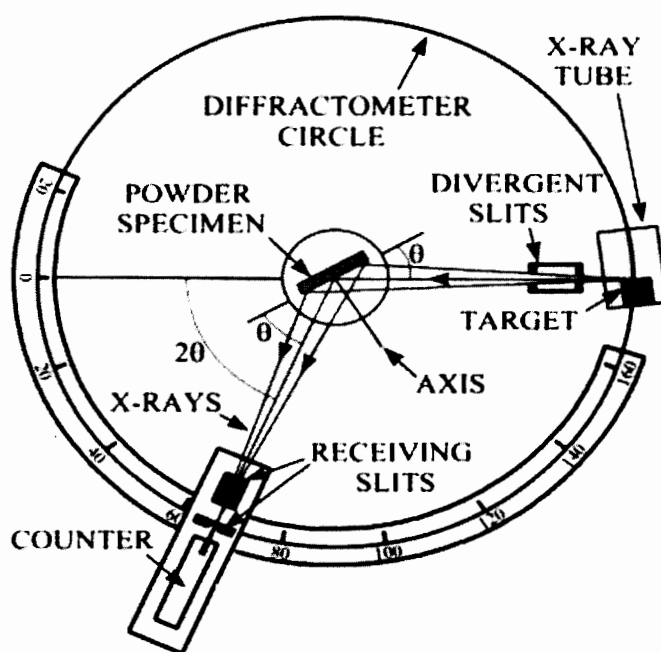


Fig. 3.3: Illustration of the working of X -ray diffractometer.

The peaks obtained is analysed by the computer program, which than compares with the existing known crystal structure so as to fits with it.

3.4.2 Scanning Electron Microscopy (SEM) and Energy Dispersive X -ray Analysis (EDS)

SEM produces high quality image with high resolving power by exploiting the wave nature of electrons. The electrons are generated by heated filament and are accelerated toward

the target; the beam produced travels in a vacuum so as to cancel any interference with the outside environment and passed through the lens to the target. When targeted with the specimen electrons, X-rays are ejected as shown in Fig. 3.4.

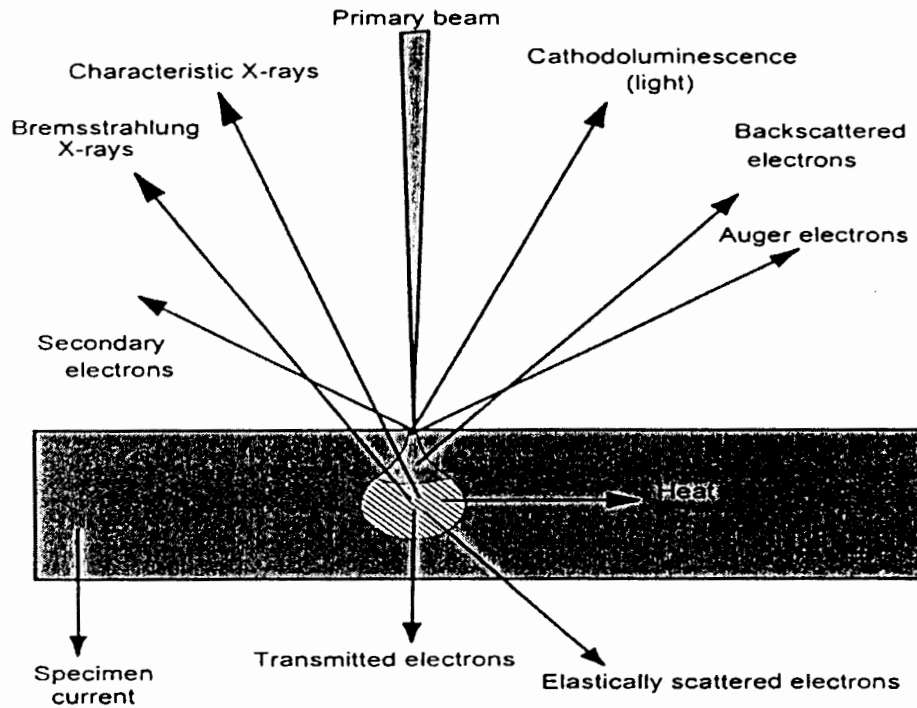


Fig. 3.4: Different Types of electrons emitted from a specimen. The EDS analysis determines the characteristics X-ray whereas SEM scans determines back scattered electrons (BSE).

The scattered particles are collected by the sensors and are converted into an electrical signal which is sent as a digital image. The specimen itself emits secondary electrons. Some of the primary electrons are reflected backscattered electrons (BSE). These backscattered electrons also cause the emission of secondary electrons as they travel through the sample and exit the sample surface. The BSE signal is used primarily for its strong atomic number contrast.

Characteristic X-rays are also widely used in SEM for elemental microanalysis (EDS). EDS works with the help of scanning electron microscope. The incoming rays bombard with the element present in the sample as a result knock of the electron near the nucleus so to fill this position electrons from the higher level occupies the ground level. The emitted rays are

characteristic rays and falls in the X-ray regime. The transition between the levels determines the specific peaks corresponding to the atom and it is unique. This analysis is quantitative it means the counts determines how much is present in area of which we are interested. JOEL Jed-2300 was used for this analysis. The transition from the L-shell to K-shell is identified as K_{α} peak as shown in Fig. 3.5.

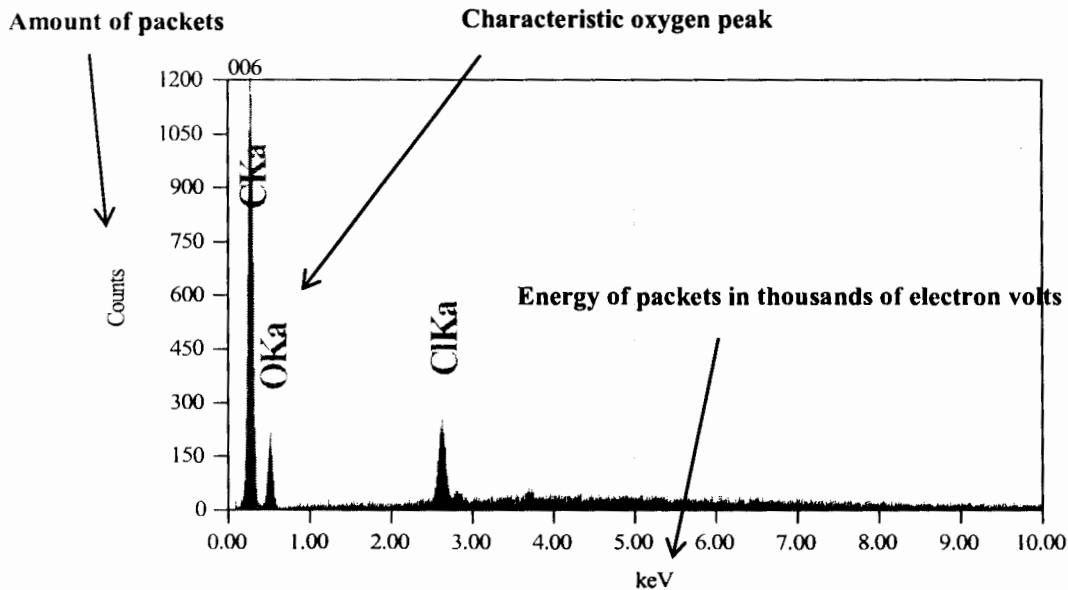


Fig. 3.5: EDS output from X-rays.

3.4.3 DC resistivity

The resistance of any substance can be measured by using Ohm's law, by using $R = V/I$, Where V is the applied voltage and ' I ' is the current flowing through the circuit and R is the resistance offered by the conductor to the moving electrons that constitute the current. Experiments have shown that the resistance of the conductor also depends upon the geometry of the conductor along with the temperature. The geometry independent measure of resistance is given by resistivity (ρ). If ' L ' is the length of a certain conductor and ' A ' is the area of cross section of it, then we can write $R = \rho l/A$. The resistivity of a material depends upon the temperature as discussed earlier. So the temperature dependent resistivity in terms of Ohm's law can be written as given by equation 3.3. The SI unit of the resistivity is $\Omega - \text{cm}$. Resistivity of the superconducting materials is measured using the four-probe method. This method is used for measurements of resistivity in metals, semiconductors and

superconductors around the world. Fig. 3.5 shows the experimental arrangement for four-probe method.

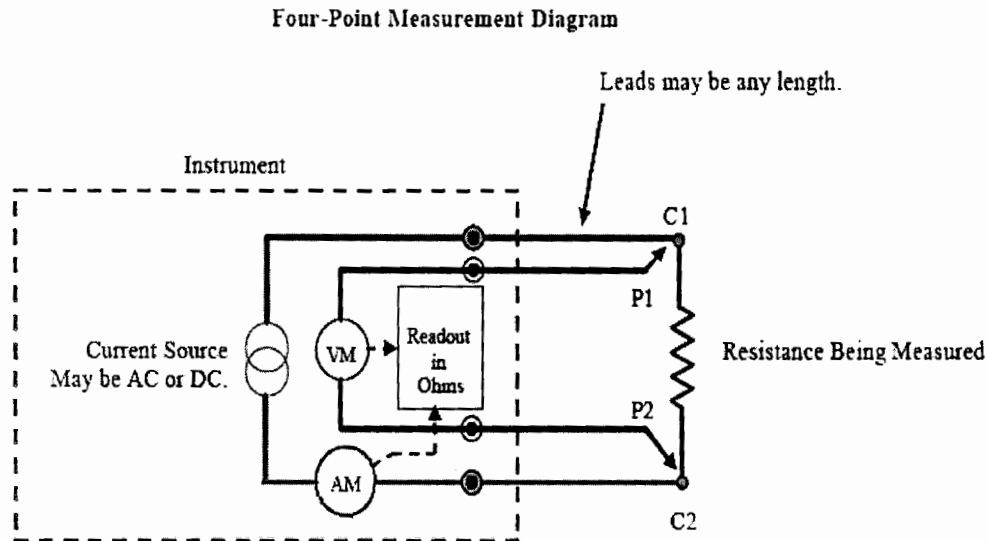


Fig. 3.6: Arrangement for resistivity measurements.

The four-probe method is a technique for measuring the resistivity of a superconducting sample. In this method four leads are attached to the sample surface at equal distance by silver paint (because of low contact resistance) [83]. The resistivity is measured by the relation given below,

$$\rho(T) = AV/LI \quad (3.3)$$

Where, V = Voltage drop across the sample, L = Length of the sample, I = Current through the sample, and A = cross-sectional area of the sample. Figure 3.6 shows the arrangement for four-probe method.

Chapter 4

RESULTS AND DISCUSSION

4.1 Introduction

The synthesis of nano-particles and superconductors (SC) has become a novel approach in the area of advance research in superconductivity. The family of $CuBa_2Ca_{n-1}Cu_nO_{2n+4-\delta}$ [$Cu - 12(n-1)n$] ($n = 1, 2, 3 \dots$) HTSCs rank with the other SC family due to less noxiousness and great $T_c(\rho = 0)$ [84]. These compounds have high zero resistivity critical temperature $\{T_c(R = 0) > 117 K\}$ even if the hole doping exceeds the optimum level. It has a low superconducting anisotropy ($\gamma = \xi_{ab}/\xi_c = 1.6$), a long coherence length along c -axis ($\xi_c = 1nm$), a small penetration depth ($\lambda = 220 nm$), a high critical current density $\{J_c = 500.5 MA/cm^2(77 K, 0 T), J_c = 0.5 MA/cm^2(77 K, 10 T)\}$, a high irreversible field $\{H_{irr} = 30 T(77 K)\}$ and low surface resistance $\{R_s = 30 \mu\Omega(77 K)\}$ [85]. However, from the application point of view its synthesis at 5 GPa at 1100°C for 3 hours is inconvenient for large scale production.

Since the discovery of Tl -based high T_c superconductor family in 1998 by Sheng and Hermann, several new phases of $Tl_mBa_2Ca_{n-1}Cu_nO_{2n+2}$ ($m = 1, 2; n = 1, 2, 3, 4, 5$) have been synthesized [86-95]. Most important phases of two layer thallium compounds includes $Tl_2Ba_2Cu_1O_6$ ($Tl - 2202$), $Tl_2Ba_2Ca_1Cu_2O_8$ ($Tl - 2212$), $Tl_2Ba_2Ca_2Cu_3O_{10}$ ($Tl - 2223$), $Tl_2Ba_2Ca_3Cu_4O_{12}$ ($Tl - 2224$), and $Tl_2Ba_2Ca_4Cu_5O_{15}$ ($Tl - 2245$) with critical temperatures of 95, 118, 127, 112 and 105 K respectively [96-97]. Whereas, single layer of Tl -based system includes $TlBa_2Ca_1Cu_2O_7$ ($Tl - 1212$), $TlBa_2Ca_2Cu_3O_9$ ($Tl - 1223$), $TlBa_2Ca_3Cu_4O_{11}$ ($Tl - 1234$) and $TlBa_2Ca_4Cu_5O_{13}$ ($Tl - 1245$) superconductor phases, with critical temperatures 103, 123, 112 and 107 K respectively. These families are represented by a generic form $Tl - 22(n-1)n$, where 'n' is the CuO_2 planes sandwiched between insulating layer. The structure of single and double $Tl - O$ layer consists of primitive tetragonal structure with $I4/mmm$ space group and body centered tetragonal structure respectively. Compared to double $Tl - O$ layers, single layers have low anisotropy, higher $T_c(R = 0)$, higher critical current densities (J_c) and irreversibility field (H_{irr}) [98-106].

The substitution of *Cu* with *Tl* in the charge reservoir layer (CRL) of $Cu - 12(n - 1)n$ produces $Cu_{1-x}Tl_x - 12(n - 1)n$ ($x = 0.5 \sim 0.8$) superconducting phases [107, 108]. As, this new family of superconductor have close resemblance to $Cu - 12(n - 1)n$ family. From the application point of view, these are easy to synthesize at low as well as great pressure [109]. The anisotropy of this compound to some extent is less than $Tl - 12(n - 1)n$ compounds [110-113]; the reason for this is the CRL of $Cu_{1-x}Tl_xBa_2O_{4n-\delta}$ during the formation slightly increases (see § 1.15). Enhancement in these superconducting compounds can be increased by post annealing in different environment and substitution of different cations [114-116]. FIC model helps to deduce theoretically the microscopic parameters and this in a way assist us to examine the correlation between different superconductivity parameters. This analysis is usually done on resistivity versus temperature data [117, 118-120]. The substitution method in the superconducting material also helps us to create pinning centres to enhance J_c .

Nano-science deals with the fabrication of nano-particle zoo from scratch. It involves, controlling of size and shape through various techniques. The use of terms nanotechnology and nano-science have a wide spread because they have a vast range of discipline and technologies [121]. Particle at the nano-scale is dominated by quantum effects and the usual behaviour is no longer comparable to particles at the larger scale. So, these quantum effects considerably change the physical and chemical properties into a new level [122]. Nano-particles have large surface area as compared to larger particles ($> 100 \text{ nm}$). The surface of nano-particles becomes important in determining the physical properties at low temperatures. In fine nano-particles ($< 5 \text{ nm}$), more atoms reside on the surface of nano-particles as compared to the core of nano-particles [123, 124]. The term nano is used for the materials having particles size in the range of $1 - 100 \text{ nm}$. Therefore, this field of research is motivating mainly due to novel and significantly improved physical and chemical properties exhibited by the nano-materials [125]. Electronic and atomic interactions are influenced by variations at the nano-meter scale. Therefore, it is possible to control the elementary properties of materials by structuring them at nano-scale [126].

The purpose of this study is to improve the inter-grain connectivity by doping the *CuO* nano-particles in $CuTl - 1223$ superconductor. The FIC analysis helps us to unearth the microscopic parameters associated above the transition temperature. In literature, few groups working in this research area have studied the doping effects of nano-structures (i.e. nano-particles, nano-rods etc.) of different materials, sizes, and concentration in high T_c

superconductor families in order to reduce the weak links and to improve the inter-grain connections for higher J_c [127-131]. In this research work, we have tried to improve superconductivity of $CuTl - 1223$ superconductor by filling the pores with CuO nanoparticles to reduce the inter-grain gaps.

4.2 Results and discussion

4.2.1 X-ray diffraction (XRD)

The X-ray diffraction (XRD) patterns of $(CuO)_x/CuTl - 1223$ composites are shown in Fig. 4.1 (a) for $x = 0\%$ and in Fig. 4.1 (b) for $x = 15\%$. XRD reveals a large amount of diffraction peaks are indexed to $CuTl - 1223$ tetragonal structure and the calculated cell parameters are $a = 3.79 \text{ \AA}$ and $c = 14.96 \text{ \AA}$ for $x = 0\%$ and $a = 3.80 \text{ \AA}$ and $c = 14.95 \text{ \AA}$ for $x = 15\%$. There are very few un-indexed peaks of very low intensity represent the presence of impurities or some other phases. This shows that the addition of CuO nanoparticles has not changed the stoichiometry of the final compound. This gives us a clue that CuO nano-particles added in the final stage of two-step solid-state reaction method remain at the inter-grain boundaries of $CuTl - 1223$ superconductor material.

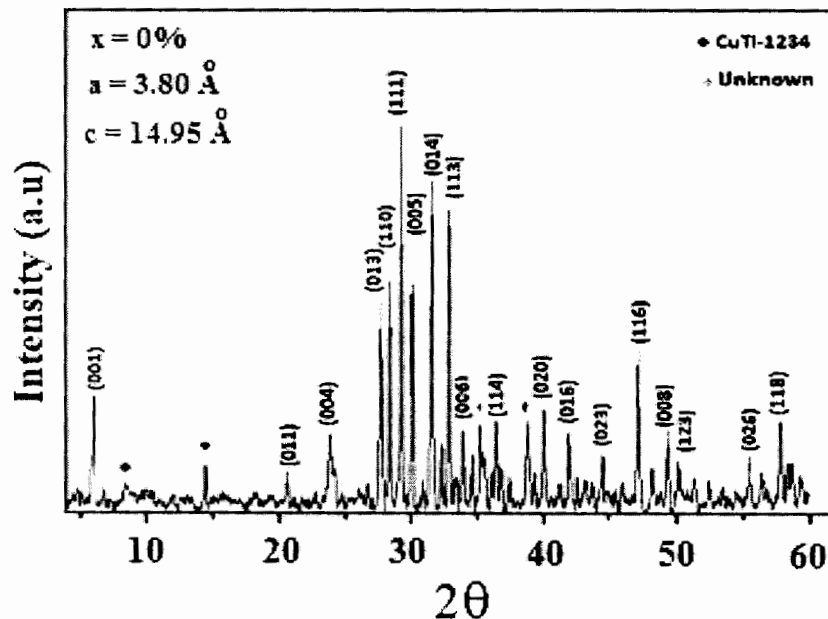


Fig. 4.1 (a): The X-ray diffraction (XRD) patterns of $(CuO)_x/CuTl - 1223$ composites for $x = 0\%$.

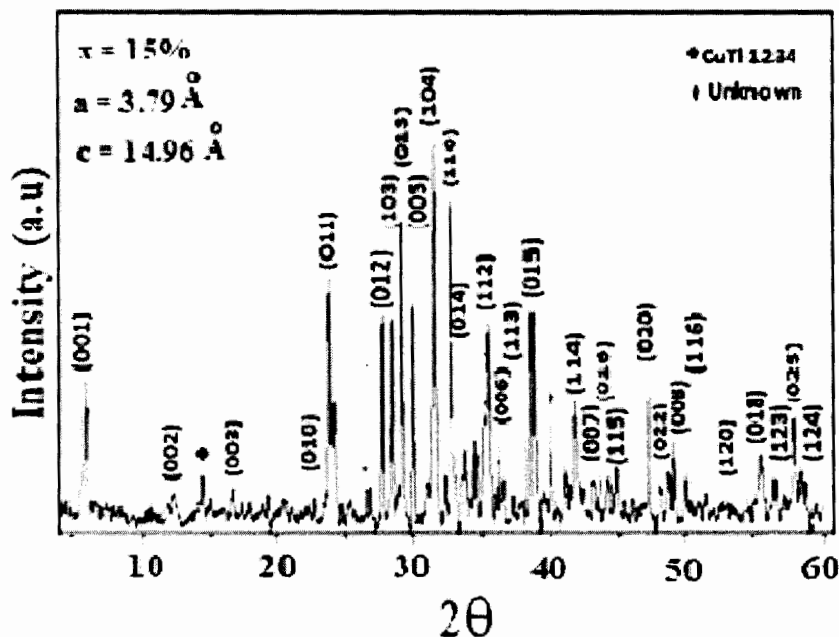


Fig. 4.1 (b): The X-ray diffraction (XRD) patterns of $(\text{CuO})_x/\text{CuTl} - 1223$ composites for $x = 15\%$.

4.2.2 Scanning Electron Microscopy (SEM) and Energy Dispersive X-ray (EDX) Analysis

The SEM of $(\text{CuO})_x/\text{CuTl} - 1223$ composites is shown in Fig. 4.2 (a) for $x = 0\%$ and Fig. 4.2 (b) for $x = 15\%$. These micrographs show that the population of inter-grain voids decreases with the increase of CuO nano-particles concentration. These micrographs show the presence of CuO nano-particles at grain boundaries and they have just occupied the voids regions resulting in an improved inter-grain connectivity. The significant texturing after CuO nano-particles addition shows the importance of CuO nano-particles in improving the inter-grain coupling. The energy dispersive X-ray (EDX) analysis of $(\text{CuO})_x/\text{CuTl} - 1223$; $x = 15\%$ shows the stoichiometry of compositional elements as shown in Fig. 4.3 (a, b). The weight percentages of compositional elements are given in Table 4.1.

Table 4.1: The energy dispersive X-ray (EDX) analysis of $(CuO)_x/CuTl - 1223$; $x = 15\%$ composite showing % of different parameters.

ZAF Method Standard-less Quantitative Analysis

Fitting co-efficient: 0.6045

Element	(KeV)	Mass %	Error %	Atom %	K
O K	0.525	11.84	0.89	39.05	11.4421
Ca K	3.690	6.91	0.76	9.10	8.2991
Cu K	8.040	47.09	3.34	39.10	47.7578
Ba L	4.464	31.25	2.28	12.00	30.0951
Tl M	2.267	2.91	2.46	0.75	2.4059
Total		100.00		100.00	

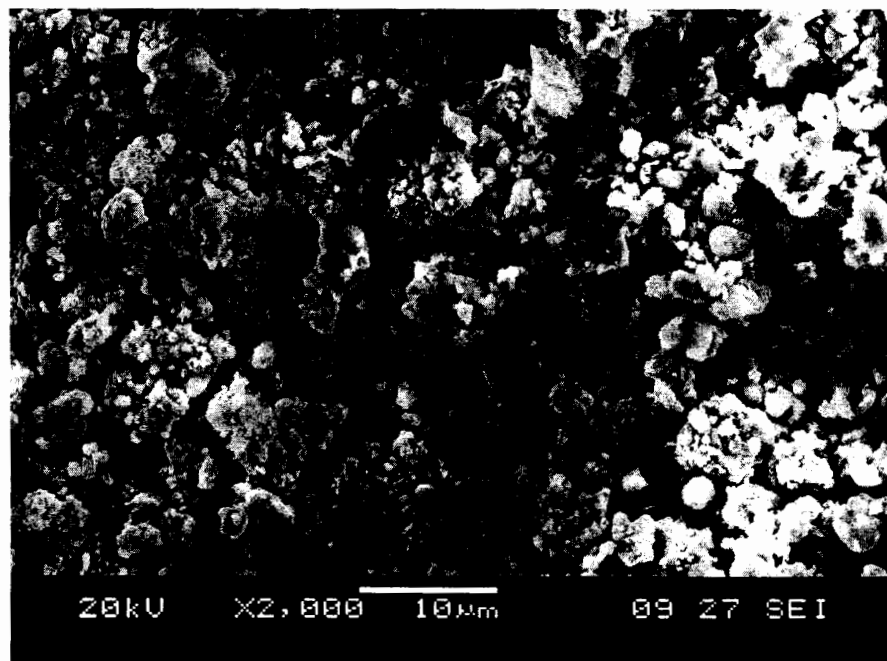


Fig. 4.2 (a): The scanning electron microscopy (SEM) of $(CuO)_x/CuTl - 1223$ composites $x = 0\%$.

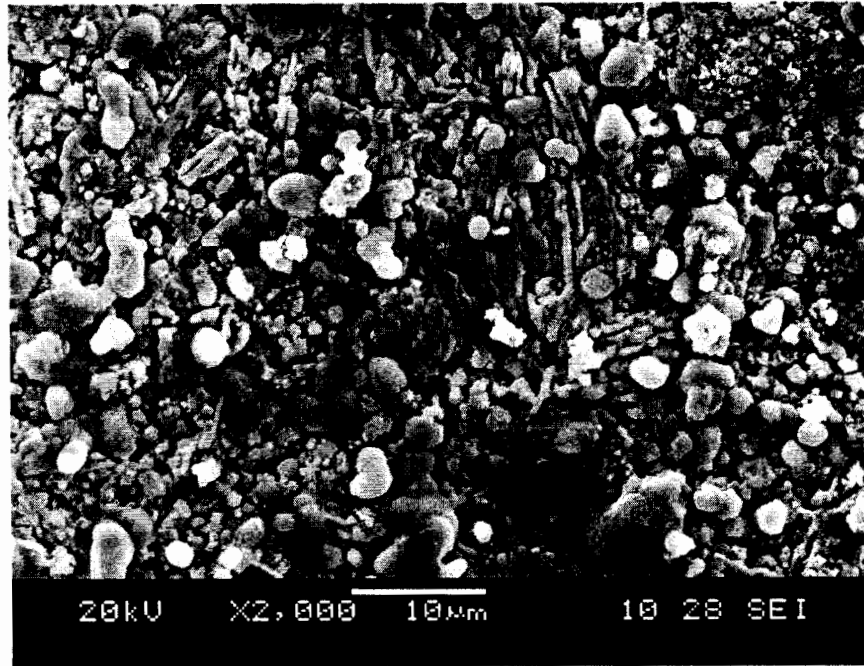


Fig. 4.2 (b): The scanning electron microscopy (SEM) of $(\text{CuO})_x/\text{CuTl}-1223$ composites $x = 15\%$.

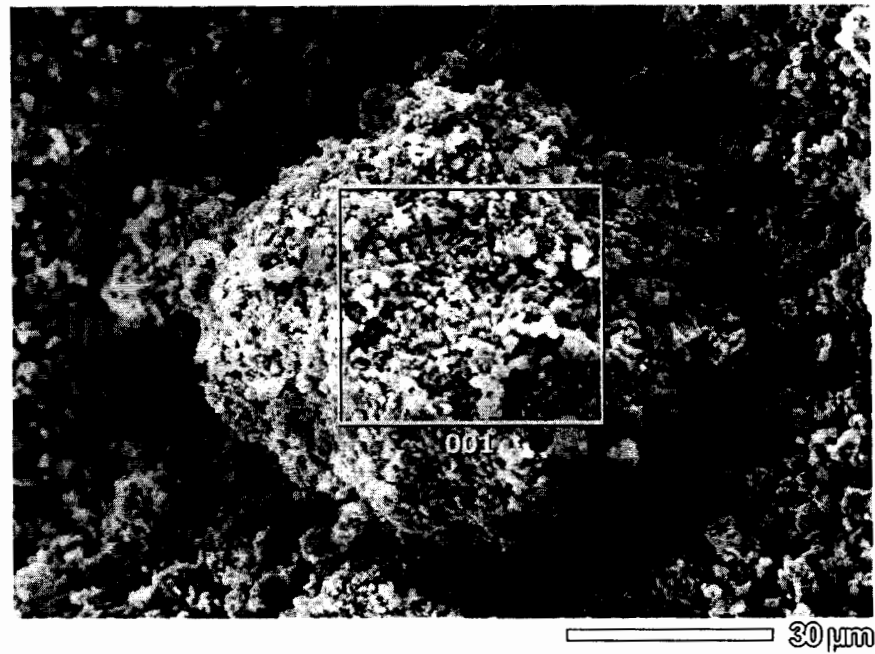


Fig. 4.3 (a): The Energy Dispersive X-ray (EDX) analysis of $(\text{CuO})_x/\text{CuTl}-1223$; $x = 15\%$ composite. SEM showing the square portion for EDX. The square box shows the region where EDX analysis was done.

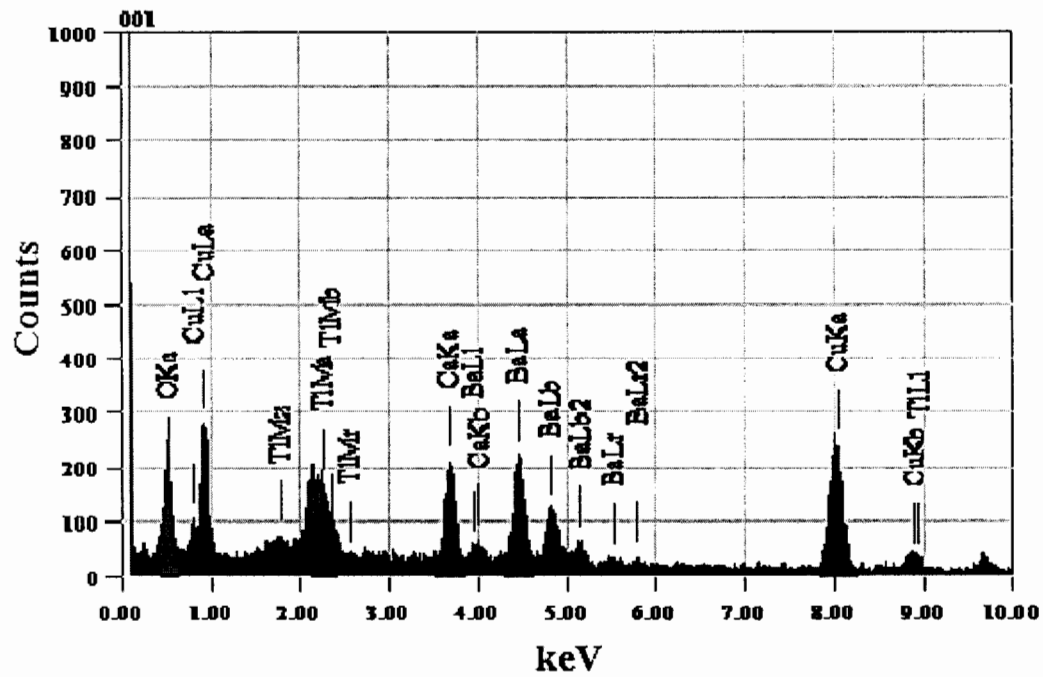


Fig. 4.3 (b): The Energy Dispersive X-ray (EDX) analysis of $(CuO)_x/CuTi - 1223$ $x = 15\%$ composite.

4.2.3 Resistivity measurements

The resistivity versus temperature measurements of as prepared and oxygen post-annealed $(CuO)_x/CuTi - 1223$ composites with $x = 0\%$, 10% , 15% and 20% are shown in Fig. 4.4 and Fig. 4.5, respectively.

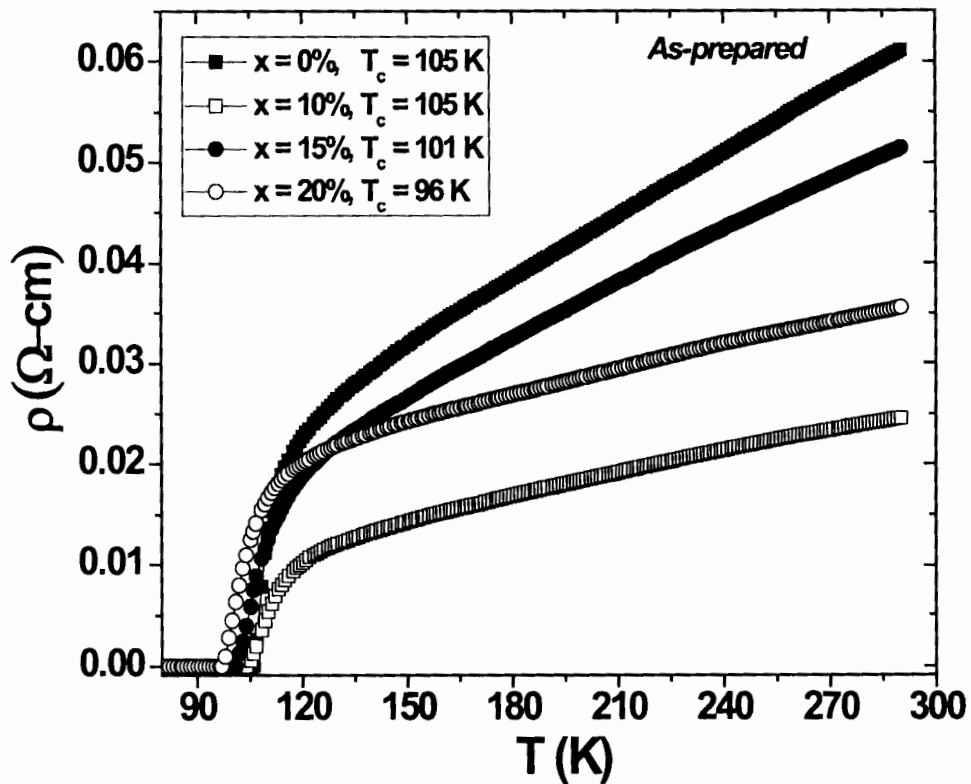


Fig. 4.4: The resistivity versus temperature measurements of as-prepared $(\text{CuO})_x/\text{CuTl} - 1223$ composites with $x = 0\%$, 10% , 15% and 20% .

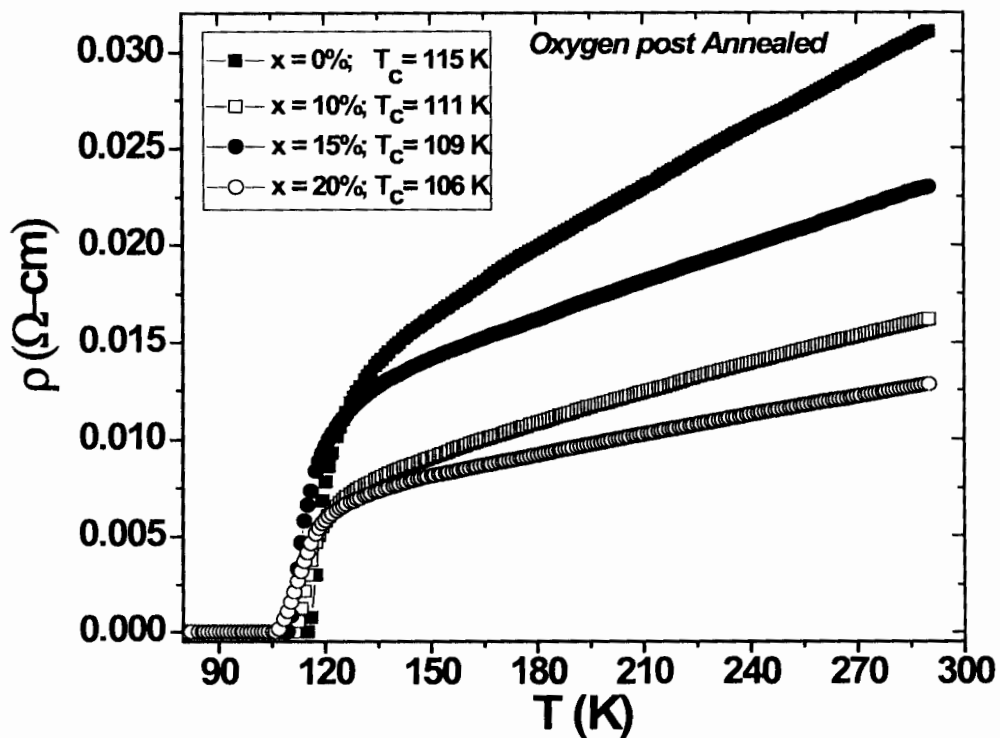


Fig. 4.5: The resistivity versus temperature measurements of oxygen post-annealed $(\text{CuO})_x/\text{CuTl} - 1223$ composites with $x = 0\%$, 10% , 15% and 20% .

These measurements show that T_c^{onset} and $T_c(R = 0)$ of as-prepared $(CuO)_x/CuTl - 1223$ samples are 123 K, 117 K, 120 K, 111 K and 105 K, 105 K, 101 K, 96 K for $x = 0\%$, 10%, 15% and 20%, respectively. The normal state resistivity $\{\rho(\Omega - cm)\}$ at room temperature has been decreased from 0.061 $\Omega - cm$ to 0.025, 0.051 and 0.036 $\Omega - cm$ with the increased wt. % of CuO nano-particles from $x = 0\%$ to $x = 10\%$, 15% and 20% respectively. The decrease in the normal state resistivity is the evidence of improved inter-grain connections after CuO nano-particles doping in $(CuO)_x/CuTl - 1223$ composites, which is also evident from SEM scans (see Fig. 4.2 (a, b)). The resistivity versus temperature measurements of oxygen post-annealed $(CuO)_x/CuTl - 1223$ samples show that T_c^{onset} and $T_c(R = 0)$ are around 123, 118, 120, 120 K and 115, 111, 109, 106 K for $x = 0\%$, 10%, 15%, 20% respectively. Almost both T_c^{onset} and $T_c(R = 0)$ have been increased after oxygen post-annealing. After oxygen post-annealing, the values of $\rho(\Omega - cm)$ at room temperature have been decreased from 0.061, 0.025, 0.051, 0.036 $\Omega - cm$ to 0.031, 0.016, 0.023, 0.013 $\Omega - cm$ for $x = 0\%$, 10%, 15% and 20%, respectively. These observations show the improvement of inter-grain coupling due to filling of oxygen vacancies in the material after oxygen post-annealing.

4.2.4 Fluctuation Induced Conductivity (FIC) analysis

The FIC analysis has been done through the use of Aslamazov-Larkin (AL) model in the mean field region [132]. AL develops the theory by assuming the materials of single phase but for the analysis of multiphase its approach is limited. AL model for FIC of crystallites have been derived within the domain of Ginzburg-Landau theory. In the framework of AL model the excess conductivity ' $\Delta\sigma$ ' is given as,

$$\Delta\sigma = A^x \varepsilon^{-\lambda} \quad (4.1)$$

where ' λ ' is the critical exponent, whose value is 0.5 for 3D fluctuations and 1.0 for 2D fluctuations and 'A' is the fluctuation amplitude in 2D and 3D regions.

$$A^{3D} = \frac{e^2}{32\hbar\xi_c(0)} \quad (4.2)$$

$$A^{2D} = \frac{e^2}{16\hbar d} \quad (4.3)$$

where ‘ d ’ is effective inter-layer thickness, ‘ e ’ is electronic charge and ‘ $\xi_c(0)$ ’ is zero temperature c -axis coherence length. The FIC in 2D and 3D regions can be calculated by $\Delta\sigma_{2D}$ and $\Delta\sigma_{3D}$ respectively as,

$$\Delta\sigma_{2D} = \frac{e^2}{16\hbar d} \varepsilon^{-\lambda} \quad (4.4)$$

$$\Delta\sigma_{3D} = \frac{e^2}{32\hbar\xi_c(0)} \varepsilon^{-\lambda} \quad (4.5)$$

The reduced temperature (ε) is given by the relation,

$$\varepsilon = \left[\frac{T - T_c^{mf}}{T_c^{mf}} \right] \quad (4.6)$$

where T_c^{mf} is the mean field critical temperature at which $d\rho/dt$ is maximum. The dimensional critical exponent ‘ λ ’ has been deduced from the slopes of $\ln(\Delta\sigma)$ versus $\ln(\varepsilon)$ plots. Lawrence-Doniach (LD) generalized AL theory, by introducing the cross-over temperature (T_o) which mainly deals with fluctuation of cooper pairs between 2D to 3D region and this value is different for different samples. Further they introduced the concept of inter-layer coupling (J) near T_c by means of Josephson coupling [132, 133]. The excess conductivity ($\Delta\sigma$) caused by thermal fluctuations according to LD is,

$$\Delta\sigma = \left(\frac{e^2}{16\hbar d} \right) \varepsilon^{-1} \left[1 + \left(\frac{2\xi_c(0)}{d} \right)^2 \right] \quad (4.7)$$

However, in a special case when $\xi_c(\varepsilon) \ll d$ and $\xi_c(\varepsilon) \gg d$ in 2D and 3D regions respectively, they govern the same AL equations. The expression for T_o according to LD model is,

$$T_o = T_{LD} = T_c^{mf} \left[1 + \left(\frac{2\xi_c(0)}{d} \right)^2 \right] \quad (4.8)$$

In equation 4.8 the term in the small bracket is called the inter-layer coupling strength (J), where this term is associated with the reduced crossover temperature ε^* by $J = \varepsilon^*/4$. In polycrystalline sample, inter-grain along with intra-grain fluctuations is described by AL theory whereas; intra-grains fluctuations are only tackled by LD theory [134]. The excess conductivity induced by thermal fluctuations for the AL case is given by

$$\Delta\sigma_{AL} = \frac{1}{\rho} - \frac{1}{\rho_n} \quad (4.9)$$

where ' ρ ' measures the actual resistivity and ' ρ_n ' is the extrapolated normal state resistivity which is approximated by the linear equation,

$$\rho_n = \alpha + \beta T \quad (4.10)$$

where ' α ' is a resistivity intercept i.e., $\alpha = \rho_n(0K)$ and ' β ' is a gradient of straight line. In the present work for FIC analysis, AL and LD expressions have been used to fit the resistivity versus temperature data near the domain of transition region. The values of λ_{2D} and λ_{3D} for as-prepared and oxygen post-annealed $(CuO)_x/CuTl - 1223$ samples are given in Table II.

The microscopic parameters such as cross-over temperature (T_o), zero temperature coherence length along c -axis $\{\xi_c(0)\}$, interlayer coupling strength (J), mean field critical temperature (T_c^{mf}) and dimensionality of conduction etc., are also calculated by FIC analysis and observed to be improved with doping of CuO nano-particles. Also the parameter ' α ' induced by FIC signifies the inter-grain coupling, whose lower values are responsible for better inter-grain connectivity and the decrease in the values of ' α ' is also in agreement with the decreased experimental normal state resistivity of the material. The value of ' α ' has been decreased with the increase of CuO nano-particles content in $(CuO)_x/CuTl - 1223$ samples and normal state resistivity $\rho(T)$ has also been decreased, which may be due to improved inter-grain connectivity.

The plots of $\ln(\Delta\sigma_{AL})$ versus $\ln(\varepsilon)$ of as-prepared $(CuO)_x/CuTl - 1223$ samples are shown in Fig. 4.6 (a) for $x = 0\%$, Fig. 4.6 (b) for $x = 10\%$, Fig. 4.6 (c) for $x = 15\%$ and Fig. 4.6 (d) for $x = 20\%$. The fitting of experimental $\ln(\Delta\sigma_{AL})$ versus $\ln(\varepsilon)$ plot by AL theory shows two distinct regions of fluctuations. These fluctuations are represented by dimensional exponent. These exponents ' λ ' corresponding to the 3D and 2D fluctuations are 0.53 and 1.2 respectively, for the un-doped ($x = 0\%$) sample, Fig. 4.6 (a). The rest of the values for 3D and 2D fluctuations are (0.49, 1.3), (0.49, 1.2) and (0.48, 1.3) respectively. However, from this analysis only one cross-over temperatures (T_o) is seen to found. This cross-over temperatures (T_o) have been observed in all doped samples which indicates that FIC is considerably changed from 3D to 2D regions in low temperature region.

Table 4.2: The critical exponents (λ_{2D} and λ_{3D}), extracted from the FIC analysis of as-prepared and oxygen post-annealed $(CuO)_x/CuTl - 1223$ composites with $x = 0\%, 10\%, 15\%$ and 20% .

$(CuO)_x/CuTl - 1223$	λ_{3D}	λ_{2D}
As-prepared		
$x = 0\%$	0.53	1.2
$x = 10\%$	0.49	1.3
$x = 15\%$	0.49	1.2
$x = 20\%$	0.48	1.3
Oxygen post-annealed		
$x = 0\%$	0.48	1.3
$x = 10\%$	0.49	1.1
$x = 15\%$	0.50	1.3
$x = 20\%$	0.48	1.3

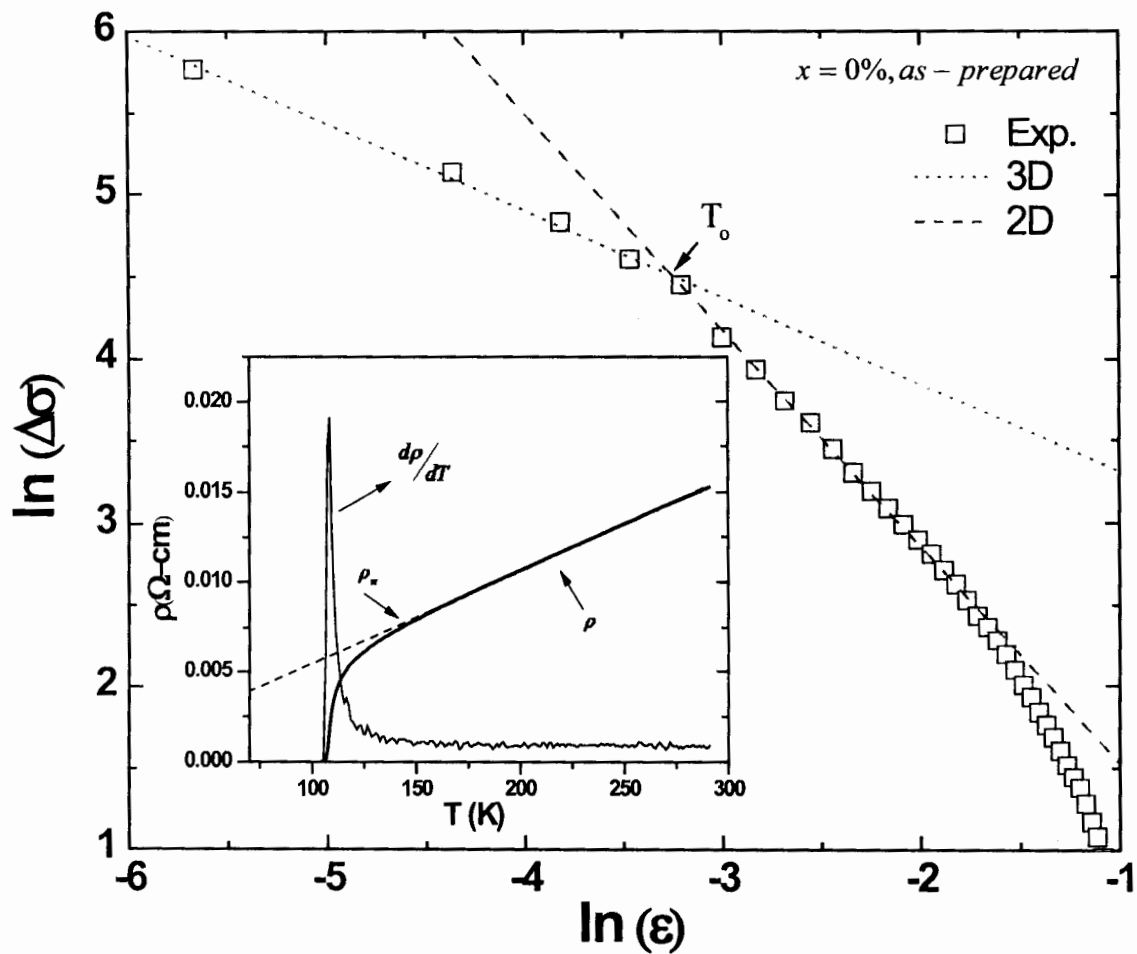


Fig. 4.6 (a): $\ln(\Delta\sigma)$ versus $\ln(\epsilon)$ plot of as-prepared $(CuO)_x/CuTl - 1223$ composite with $x = 0\%$.

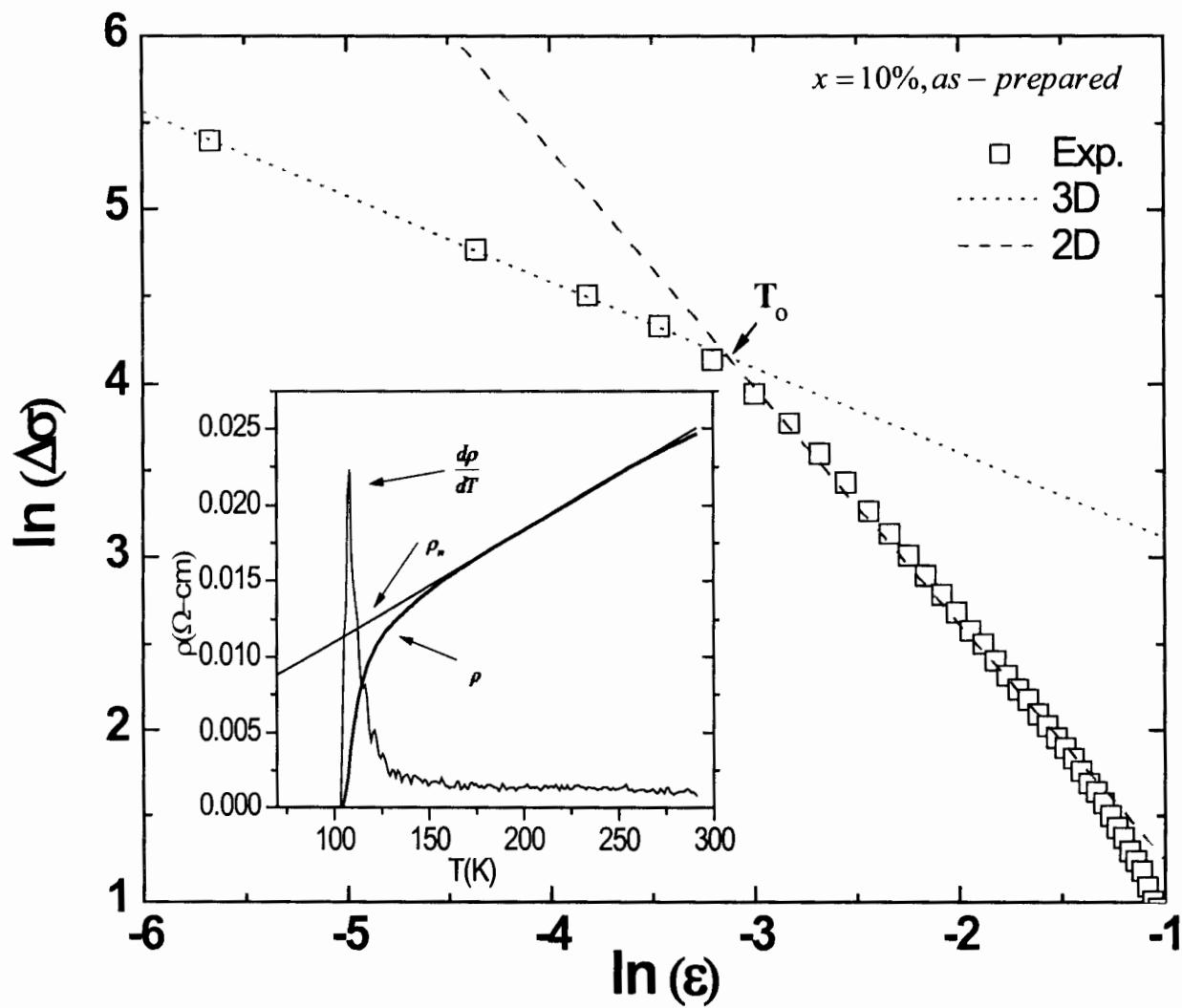


Fig. 4.6 (b): $\ln(\Delta\sigma)$ versus $\ln(\epsilon)$ plot of as-prepared $(\text{CuO})_x/\text{CuTl} - 1223$ composite with $x = 10\%$.

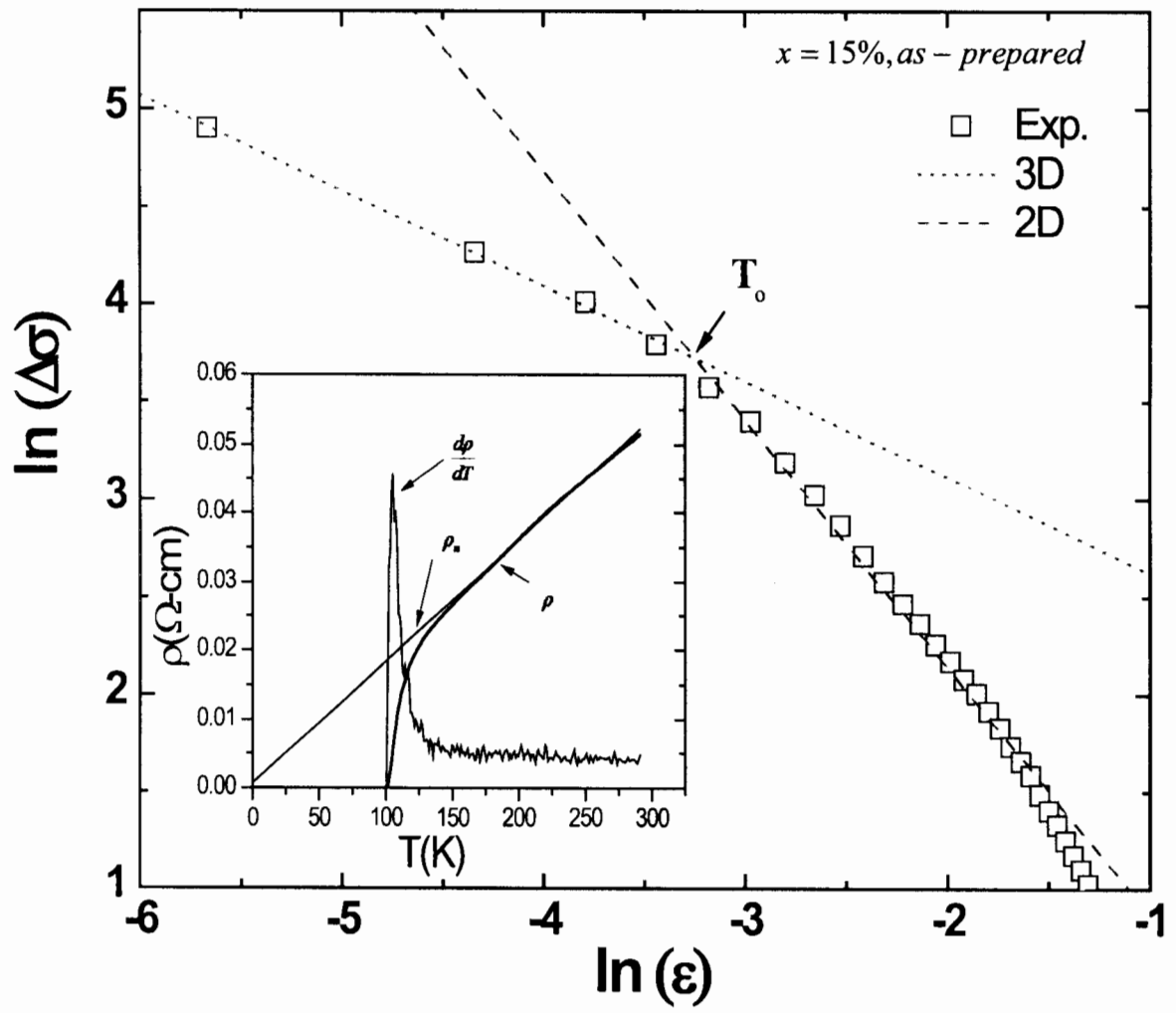


Fig. 4.6 (c): $\ln(\Delta\sigma)$ versus $\ln(\epsilon)$ plot of as-prepared $(\text{CuO})_x/\text{CuTl} - 1223$ composite with $x = 15\%$.

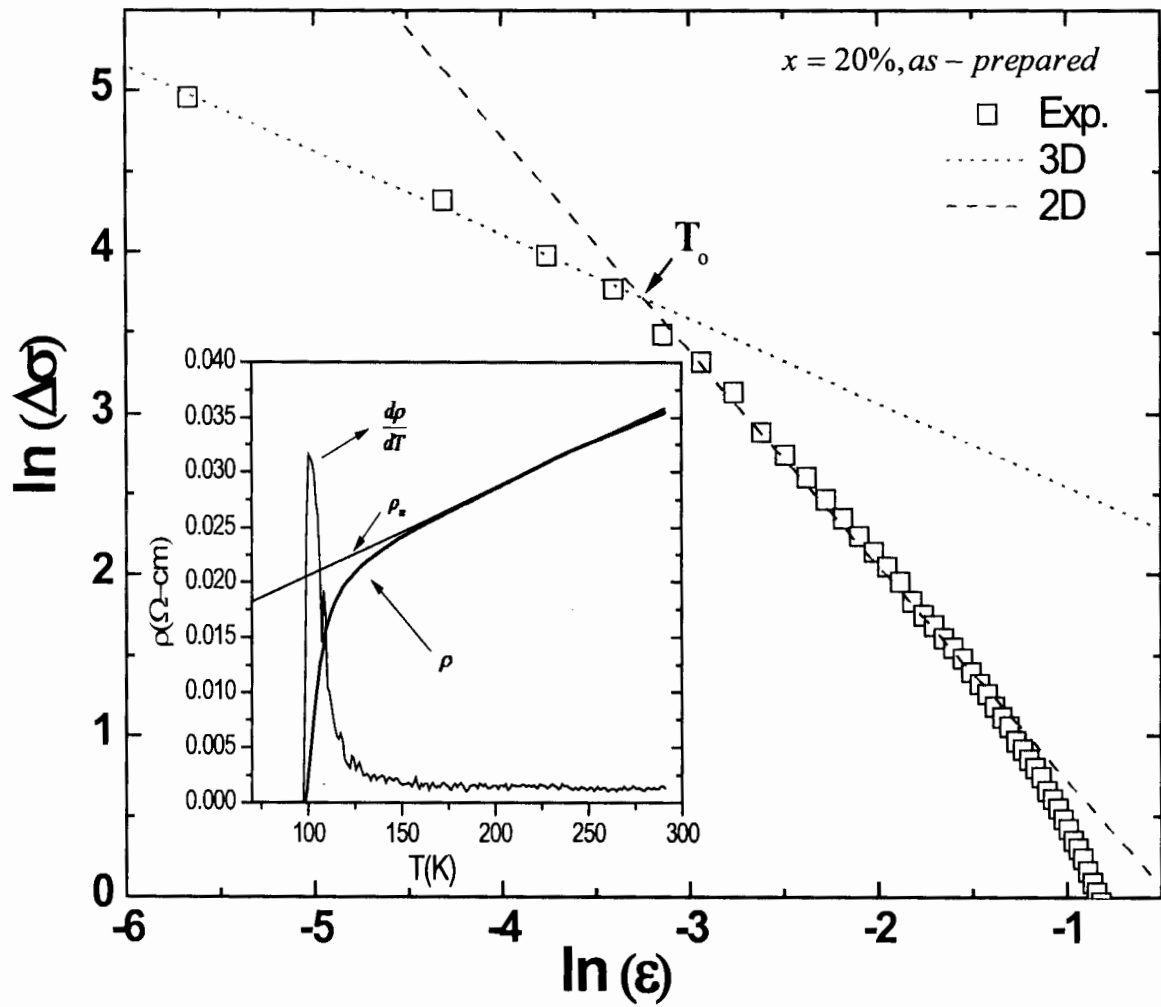


Fig. 4.6 (d): $\ln(\Delta\sigma)$ versus $\ln(\epsilon)$ plot of as-prepared $(\text{CuO})_x/\text{CuTl} - 1223$ composite with $x = 20\%$.

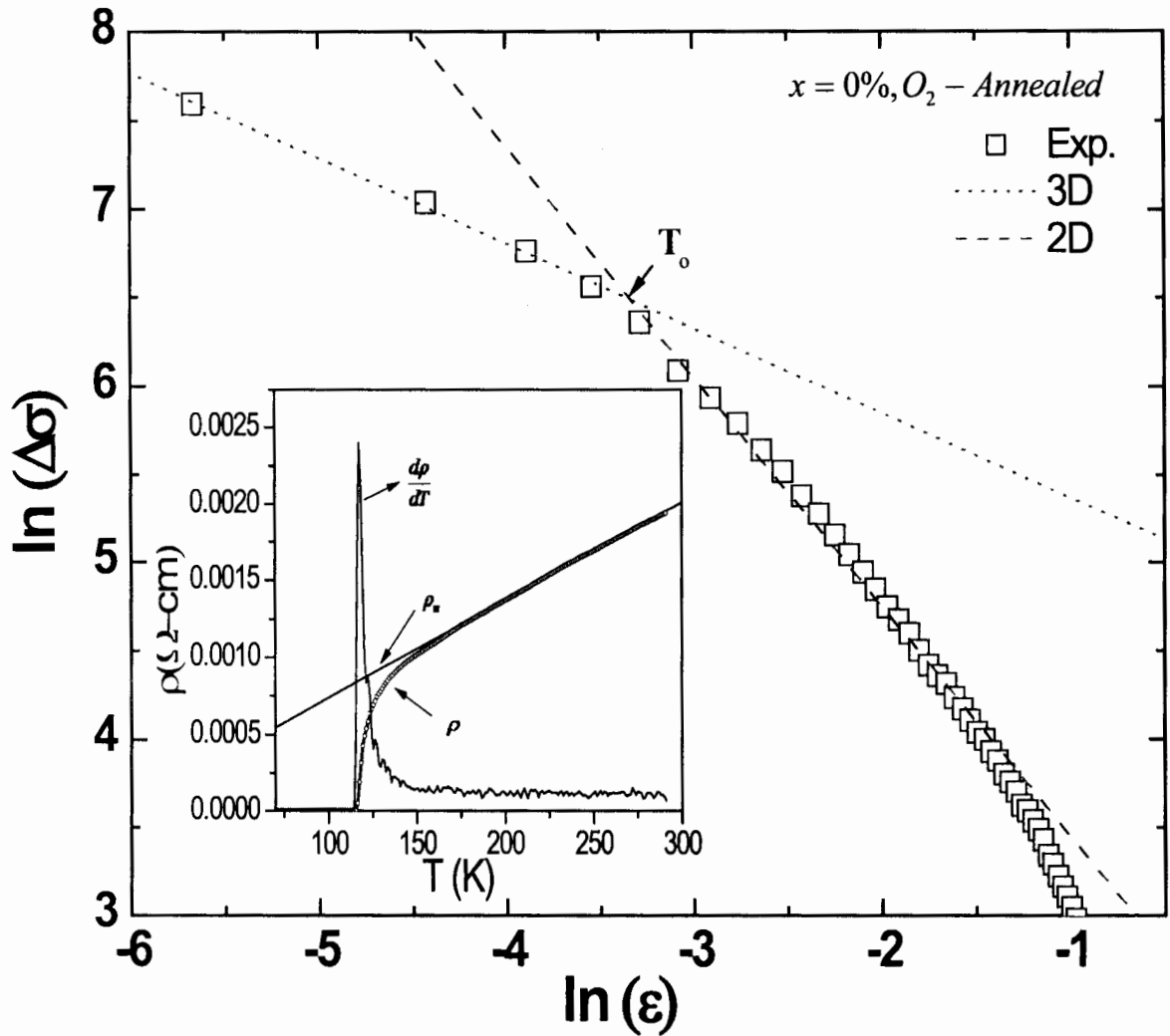


Fig. 4.7 (a): $\ln(\Delta\sigma)$ versus $\ln(\epsilon)$ plot of oxygen post-annealed $(CuO)_x/CuTl - 1223$ composite with $x = 0\%$.

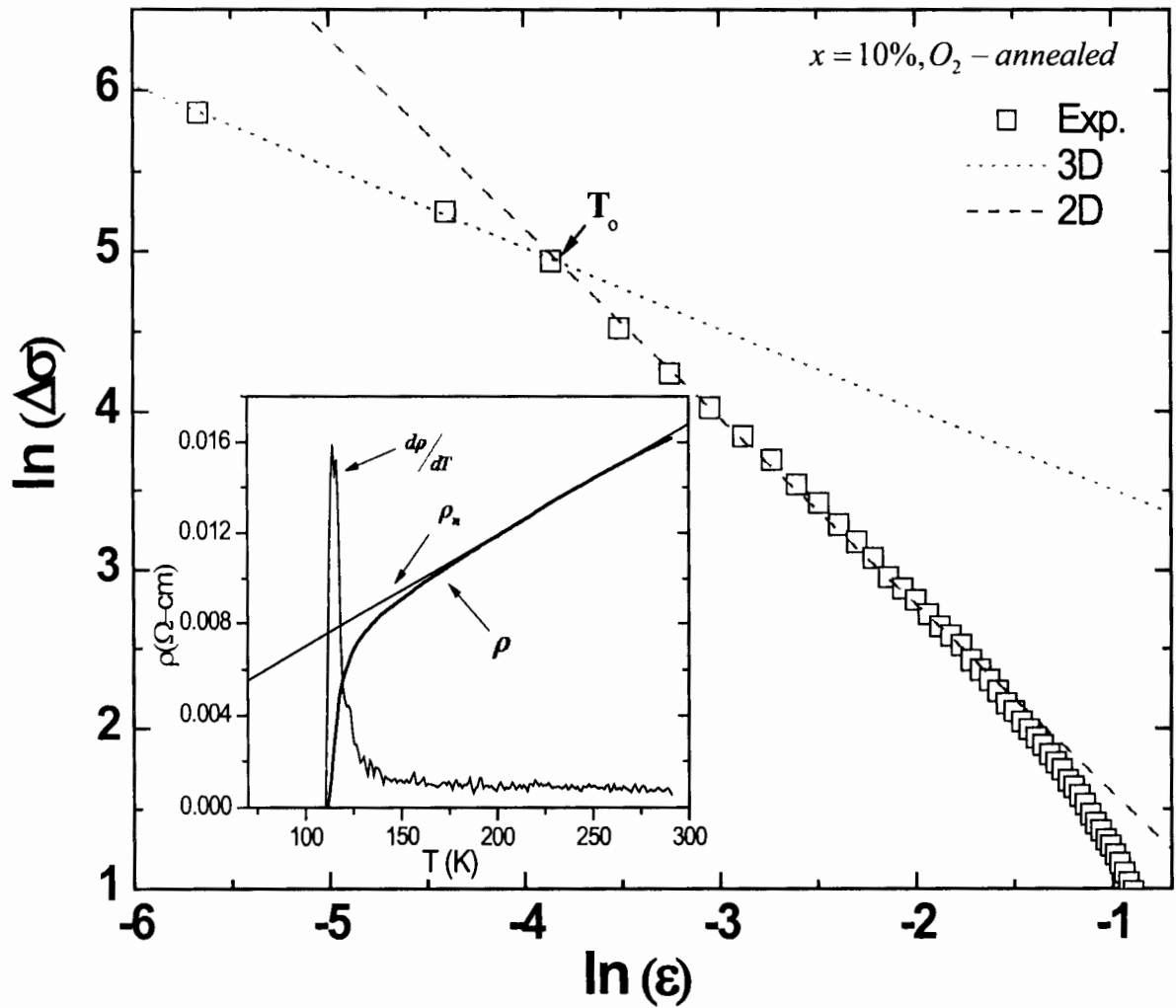


Fig. 4.7 (b): $\ln(\Delta\sigma)$ versus $\ln(\epsilon)$ plot of oxygen post-annealed $(CuO)_x/CuTl - 1223$ composite with $x = 10\%$.

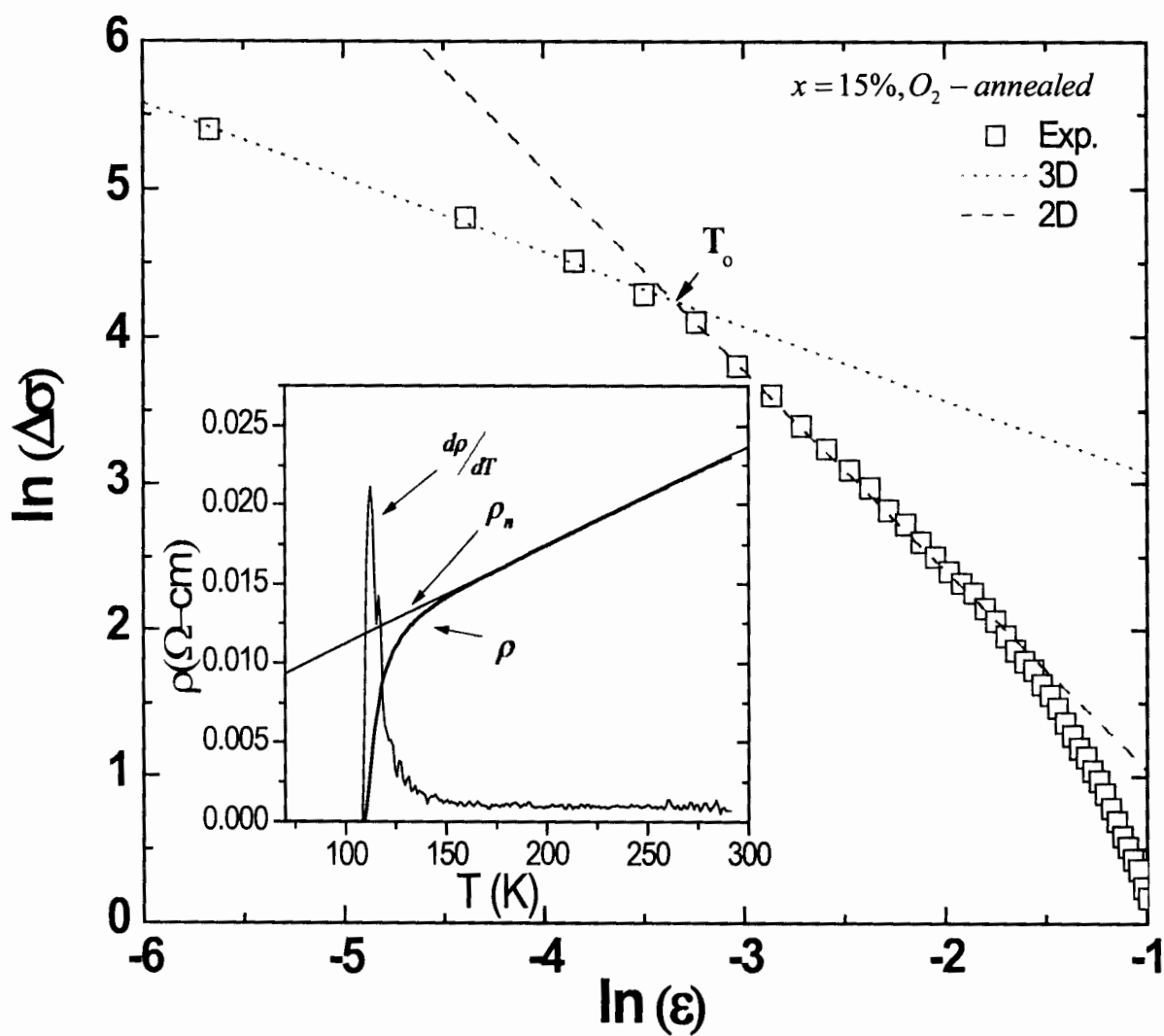


Fig. 4.7 (c): $\ln(\Delta\sigma)$ versus $\ln(\varepsilon)$ plot of oxygen post-annealed $(CuO)_x/CuTl - 1223$ composite with $x = 15\%$.

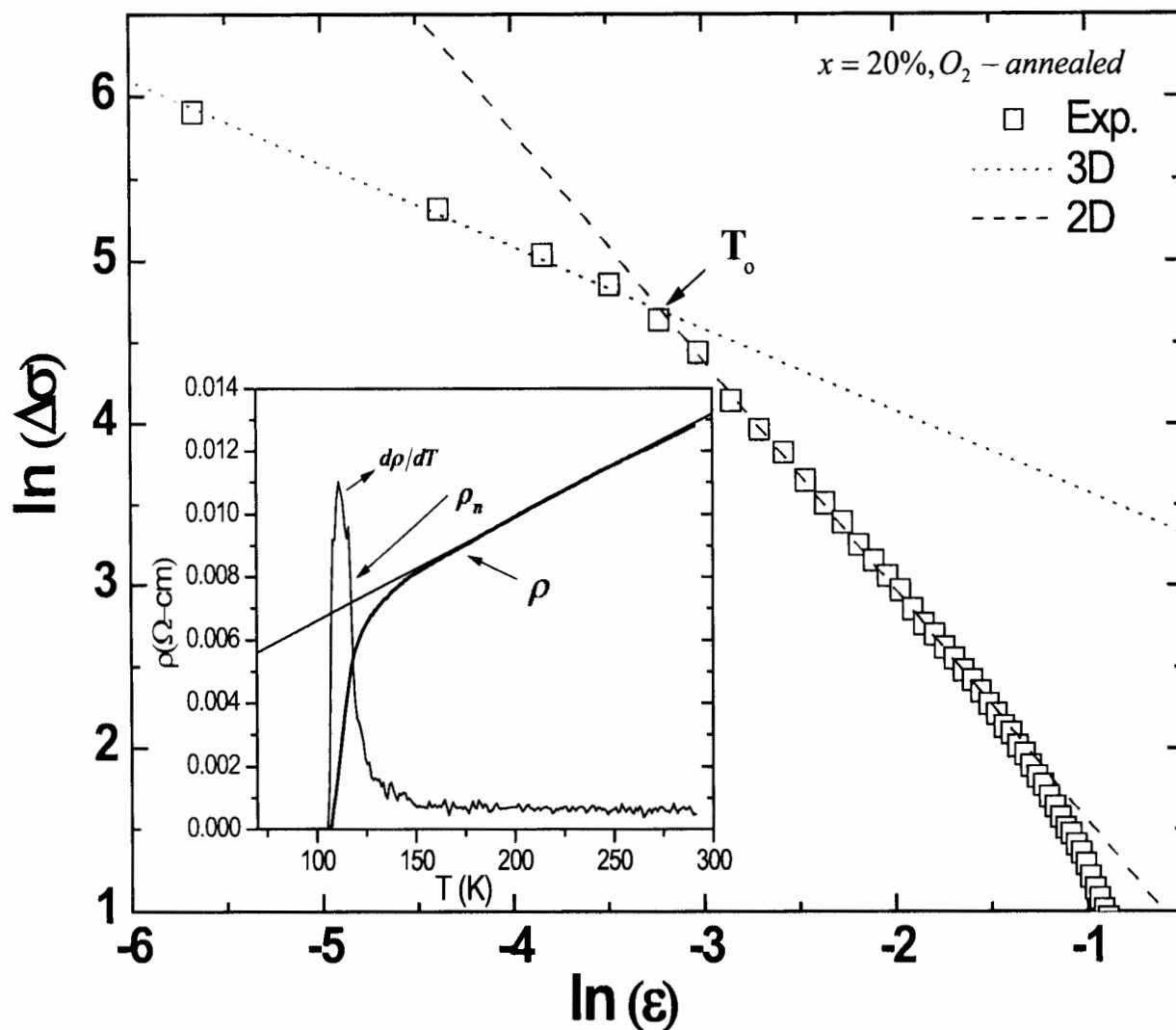


Fig. 4.7 (d): $\ln(\Delta\sigma)$ versus $\ln(\epsilon)$ plot of oxygen post-annealed $(CuO)_x/CuTl - 1223$ composite with $x = 20\%$.

The plots of $\ln(\Delta\sigma_{AL})$ versus $\ln(\epsilon)$ of oxygen post-annealed $(CuO)_x/CuTl - 1223$ samples are shown in Fig. 4.7 (a) for $x = 0\%$, Fig. 4.7 (b) for $x = 10\%$, Fig. 4.7 (c) for $x = 15\%$ and Fig. 4.7 (c) for $x = 20\%$. The exponent value ' λ ' for the oxygen post-annealed have been deduced from the slopes of \ln plot and are found to be (0.48, 1.3), (0.49, 1.1), (0.50, 1.3) and (0.48, 1.3) for the sample with $x = 0\%$, $x = 10\%$, $x = 15\%$, and $x = 20\%$, respectively. This analysis also shows the existence of only one cross-over temperature corresponding to 3D and 2D fluctuations, respectively.

The other microscopic parameters such as T_o , T_c^{mf} , J , α and $\xi_c(0)$ extricated from FIC analysis for the case of as-prepared and oxygen post-annealed samples are given in Table 4.3 and Table 4.5, whereas, fluctuation widths are given in Table 4.4 and Table 4.6 respectively. It can be seen from Table 4.3 and Table 4.5 that T_o change to higher temperature values after oxygen post-annealing. On the other hand $\xi_c(0)$ and J have been increased with the increase of doping percentage of CuO nano-particles in $(CuO)_x/CuTl - 1223$ samples, which reflects the improved inter-layer coupling strength in the material. The decrease in $\rho(T)$ with the increase of CuO nano-particles content in $(CuO)_x/CuTl - 1223$ samples is the fingerprint of improved inter-layer coupling. The increased value of $\xi_c(0)$ shows the improved three-dimensional conductivity with the increase concentration of CuO nano-particles in $(CuO)_x/CuTl - 1223$ samples. All the properties are observed to be improved after oxygen post-annealing, which is the evidence of oxygen intercalation with material. The superconducting properties start to suppress when the doping concentration of CuO nano-particles increases beyond $x = 15\%$. The excessive concentration of CuO nano-particles in $CuTl - 1223$ superconductor may cause the agglomeration of CuO nano-particles in the matrix of superconducting material that may increase the resistance to the tunnelling of carriers through the grain boundaries.

Table 4.3: The parameters such as normal state resistivity $\rho_n(290K)$, the zero resistivity critical temperature (T_c), onset of superconductivity (T_c^{onset}), cross-over temperatures (T_o), mean field critical temperature (T_c^{mf}), inter-grain coupling constant (α), zero temperature coherence length along c-axis $\{\xi_c(0)\}$ and inter-plane coupling (J) take out from the FIC analysis of as-prepared $(CuO)_x/CuTl - 1223$ composites with $x = 0\%, 10\%, 15\%$ and 20% .

wt. % of nano- particles	$\rho_n(290K)$ ($\Omega - cm$)	T_c (K)	T_c^{onset} (K)	ΔT_c (K)	T_o (K)	T_c^{mf} (K)	$\alpha = \rho_n(0 K)$ ($\Omega - cm$)	$\xi_c(0)$ (\AA)	$J = \left\{ \frac{2\xi_c(0)}{d} \right\}^2$
0%	0.061	105	123	17	113	108	0.0011	1.927	0.066
10%	0.025	105	117	12	112	108	0.0010	1.936	0.067
15%	0.051	101	120	19	109	105	0.0004	2.110	0.079
20%	0.036	96	111	15	105	101	0.0009	2.153	0.082

Table 4.4: The fluctuation widths of 3D and 2D regions observed by the fitting of experimental data using AL model, on resistivity data of as-prepared $(CuO)_x/CuTl - 1223$ composites with $x = 0\%$, 10% , 15% and 20% .

wt. % of nano- particles	λ_{3D} Temperature	$Ln(\epsilon)$ (range in 3D)	λ_{2D} Temperature	$Ln(\epsilon)$ (range in 2D)
0%	109 – 113	$-5.6 < \ln(\epsilon) < -3.2$	113 – 129	$-3.2 < \ln(\epsilon) < -1.6$
10%	109 – 112	$-5.6 < \ln(\epsilon) < -3.4$	112 – 134	$-3.4 < \ln(\epsilon) < -1.4$
15%	106 – 109	$-5.6 < \ln(\epsilon) < -3.4$	109 – 130	$-3.4 < \ln(\epsilon) < -1.4$
20%	102 – 105	$-5.6 < \ln(\epsilon) < -3.4$	105 – 130	$-3.4 < \ln(\epsilon) < -1.3$

The contribution of FIC to 2D and 3D excess conductivities has been calculated by using the coherence length formula along c -axes. The values of $\xi_c(0)$ for as-prepared samples are 1.927, 1.936, 2.110 and 2.153Å, whereas for the oxygen post-annealed samples are 1.850, 1.891, 1.900 and 2.314Å for $x = 0\%$, 10% , 15% and 20% , respectively. In both cases, the increased $\xi_c(0)$ is witnessed that the doped CuO nano-particles bridge the gaps and ease the path for the cooper pairs. The broadening of transition width ΔT_c indicates presence of impurities and multiphase as indicated in XRD patterns. The value of critical exponent λ_{3D} for as-prepared samples are 0.53, 0.49, 0.49 and 0.48 in the temperature regimes of 109 – 113, 109 – 112, 106 – 109, and 102 – 105K respectively, while for oxygen post annealed samples are 0.48, 0.49, 0.50 and 0.48 in the temperature regimes 119 – 122, 115 – 117, 113 – 116, and 112 – 115K respectively, Table 4.2, 4.4 and Table 4.2, 4.6. The dimensional exponent shows a little deviation from the theoretical values given by the AL model that may be due to polycrystalline nature of samples. The shift of 3D AL regime to lower temperature values indicates that the excessive doping of CuO nano-particles reduces the superconducting grain size resulting in the suppression of T_c and T_0 . The values of exponent λ_{2D} for as-prepared samples are 1.2, 1.3, 1.2 and 1.3 in the temperature regimes of 113 – 129, 112 – 134, 109 – 130, and 105 – 130K respectively, while for oxygen post annealed samples are 1.3, 1.1, 1.3 and 1.3 in the temperature regimes 122 – 149, 117 – 138, 116 – 136, and 115 – 140K, respectively, Table 4.2, 4.4 and Table 4.2, 4.6. The superconductivity parameters have been improved after CuO nano-particles doping in $(CuO)_x/CuTl - 1223$ composites up to $x = 15\%$ and superconductivity

starts to deteriorate beyond $x = 15\%$ concentration. The superconductivity has been further improved by oxygen post-annealing.

Table 4.5: The parameters such as normal state resistivity $\rho_n(290K)$, the zero resistivity critical temperature (T_c), onset of superconductivity (T_c^{onset}), cross-over temperatures (T_o), mean field critical temperature (T_c^{mf}), inter-grain coupling constant (α), zero temperature coherence length along c -axis $\{\xi_c(0)\}$ and inter-plane coupling (J) take out from the FIC analysis of oxygen post-annealed $(CuO)_x/CuTl - 1223$ composites with $x = 0\%, 10\%, 15\%$ and 20% .

wt. % of nano-particles	$\rho_n(290K)$ ($\Omega - cm$)	T_c (K)	T_c^{onset} (K)	ΔT_c (K)	T_o (K)	T_c^{mf} (K)	α $= \rho_n(0K)$ ($\Omega - cm$)	$\xi_c(0)$ (\AA)	$J = \left\{ \frac{2\xi_c(0)}{d} \right\}^2$
0%	0.031	115	123	8	122	118	0.0054	1.850	0.0608
10%	0.016	111	118	7	117	114	0.0051	1.891	0.0636
15%	0.023	109	120	11	116	112	0.0050	1.900	0.0642
20%	0.013	106	120	14	115	111	0.0048	2.314	0.0952

Table 4.6: The fluctuation widths of 3D and 2D regions observed from the fitting of the experimental data using AL model, on resistivity data of oxygen post-annealed $(CuO)_x/CuTl - 1223$ composites with $x = 0\%, 10\%, 15\%$ and 20% .

wt. % of nano-particles	λ_{3D} Temperature	$Ln(\epsilon)$ (range in 3D)	λ_{2D} Temperature	$Ln(\epsilon)$ (range in 2D)
0%	119 – 122	$-5.6 < ln(\epsilon) < -3.5$	122 – 149	$-3.5 < ln(\epsilon) < -1.4$
10%	115 – 117	$-5.6 < ln(\epsilon) < -3.8$	117 – 138	$-3.8 < ln(\epsilon) < -1.5$
15%	113 – 116	$-5.6 < ln(\epsilon) < -3.4$	116 – 136	$-3.4 < ln(\epsilon) < -1.5$
20%	112 – 115	$-5.6 < ln(\epsilon) < -3.4$	115 – 140	$-3.4 < ln(\epsilon) < -1.4$

CONCLUSION

The ceramic polycrystalline $(CuO)_x/CuTl - 1223$ composites have been successfully synthesized and studied. The microscopic parameters such as T_o , T_c^{mf} , J , α , and $\xi_c(0)$ etc. have been extracted from FIC analysis of $(CuO)_x/CuTl - 1223$ composites. The cross-over temperature (T_o) fits the two-dimensional (2D) and three-dimensional (3D) AL equations and shifts towards the lower temperature regimes with the increased concentration of CuO nano-particles in these as-prepared composites. After oxygen post-annealing, the shifting of 3D AL region to higher temperature values indicates the restoration of the oxygen and optimization of charge carriers in conducting CuO_2 planes. The decrease in the value of “ α ” reflects the improvement of inter-grain coupling with the increase of CuO nano-particles content in these composites resulting into an increase in the coherence length (ξ_c) along the c -axis. The superconductivity parameters have also been further improved by oxygen post-annealing the samples. In these studies the suppression of superconductivity parameters beyond $x = 15\%$ doping of CuO nano-particles limits the optimum level of doping of these nanoparticles. The composite with $x = 15\%$ have shown textured elongated crystalline with low population of voids as evidence by SEM images. Due to the granularity and porous character of $CuTl - 1223$ superconductor, its exhibits lower superconductivity parameters such as J_c values. The better inter-grain coupling may improve J_c by suppressing the Josephson losses across the Josephson junctions, which is an important parameter in the course of superconductor device fabrication and wire applications.

REFERENCES

- [1] Kimberling Onnes, *Comm. Phys. Lab. Univ. Leiden*, **122-124** (1911) 1226.
- [2] James F. Annett, *Superconductivity, Superfluid's, and condensates*, (Oxford University Press, 1st ed., 2004, pp. 49-52).
- [3] V.V Schmidt, P. Muller, A.V. Ostinov, *the Physics of Superconductors*, 1st ed., (1997).
- [4] M. A. Omar, *Elementary Solid State Physics*, 3rd ed. Addison Wesley, 2007.
- [5] Meissner, W. and R. Ochsenfeld, *Naturwissenschaften* **21** (1933) 787-788.
- [6] James F. Annett, *Superconductivity, Superfluid's and condensates*, (Oxford University Press, 1st ed., 2004, pp. 49-52).
- [7] C. Kittel, *Introduction to Solid State Physics* (New York, NY: Wiley, 2nd ed., 1976).
- [8] *The Physics of Organic Superconductors and Conductors*, A.G. Lebed, 1st ed., Springer Series in Materials Science 110, 2008.
- [9] A.A Abrikosov, *Soviet Physics JETP* **5** (1957) 1174-1182.
- [10] O. Ieksanr Bakai and Yuriy Raniuk, *History of Physics Research in Ukraine*", Kharkov Institute of Science and Technology, 1993.
- [11] Charles P. Poole, *Superconductivity* (Elsevier, New York, 2nd ed., 15-70)
- [12] London, F. and H. London, *Proc. Roy. Soc. A* **149** (1935) 71-88.
- [13] V.L. Ginzburg and L.D. Landau, *Zh. Eksp. Theor. Fiz.* **20** (1950) 1064. English translation in: L. D. Landau, *Collected papers* (Oxford: Pergamon Press, 1965, pp. 546).
- [14] Bardeen J., *et al.*, *Phys. Rev.* **108** (1957) 1175-1204; Cooper, L.N., *Phys. Rev.*, **104** (1956) 1189-1190.
- [15] Shoji Tanaka, *Jap. J. App. Phys.* **45** (2006) 12.
- [16] J. G. Bednorz and K. A. Müller, *Z. Phys.* **64** (1986) 189; M. K. Wu, J. R. Ashburn, C. J. Torng, P. H. Hor, R. L. Meng, L. Gao, Z. J. Huang, Y. Q. Wang and C. W. Chu, *Phys. Rev. Lett.* **58** (1987) 908.
- [17] C. W. Chu, *J. Superconductivity* **12** (1999) 85.
- [18] C. W. Chu, *IEEE Trans. Appl. Superconductivity* **7** (1997) 80.
- [19] H. Yamauchi, M. Karppinen, S. Tanaka, *Physica C* **263** (1996) 146.
- [20] H. Yamauchi, M. Karppinen, *Supercond. Sci. Technol.* **13** (2000) R33.
- [21] P. Bordet *et al.*, *Physica C* **276** (1997) 237.
- [22] N. L. Wu *et al.* *Mater. Chem. Phys.* **78** (2003) 785.
- [23] O. Chmaissem *et al.*, *Nature* **397** (1999) 45.
- [24] P. W. Anderson, *Science* **235** (1987) 1196.
- [25] K. Yvon and M. François., *Z. Phys. B* **76** (1989) 413-444.
- [26] L. Gao *et al.* *Phys. Rev. B* **50** (1994) 4260.
- [27] T. H. Geballe and B. Y. Mozhes, *Physica C* **341-348** (2000) 1821.
- [28] J. Orenstein and A. J. Millis, *Science* **288** (2000) 468.
- [29] G. Grasso and R. Flükiger, *Supercond. Sci. Technol.* **10** (1997) 223.
- [30] H. Ihara, *et al.*, *Nature* (London) **334** (1988) 510.
- [31] H. Ihara, R. Sugise, K. Hayashi, N. Terada, M. Jo, M. Hirabayashi, A. Nigishi, N. Atod H. Oyanagi, T. Shimomura, S. Ohashi, *Phys. Rev. B* **38** (1988) 11952.
- [32] R. Sugise, M. Hirabayashi, N. Terada, M. Jo., T. Shimomura and H. Ihara, *J. Appl.* **27** (1988) 1709.
- [33] S. S. P. Parkin, V. Y. Lee, A. I. Nazzal, R. Savoy, R. Beyers and J. La. Placa, *Phys. Rev. Lett.* **61** (1988) 750.

References

- [34] H. Ihara, K. Tokiwa, K. Tanaka, T. Tsukamoto, T. Watanabe, H. Yamamoto, A. Iyo, M. Tokumoto and M. Umeda, *Physica C* **957** (1997) 282-287.
- [35] Cuo Zhang Cao, (Nanomaterials and nanostructure, 1st ed., p: 10-50).
- [36] A. B. Kuz'menko, D. van der Marel *Phys. Rev. B* **63** (2001) 094303.
- [37] Ajay Kumar Sexsana, High temperature superconductor, (New York, Springer, 2010).
- [38] M. Okada, *Supercond. Sci. Technol.* **13** (2000) 29.
- [39] L. Alff *et al.*, *Rep. Prog. Phys.* **62** (1999) 61.
- [40] M. Buchanan, *Nature* **409** (2001) 11.
- [41] C. Meingast *et al.*, *Phys. Rev. Lett.* **86** (2001) 1606.
- [42] E. Dagotto, *Rev. Mod. Phys.*, **66** (1994) 763.
- [43] B. Batlogg, *Solid State Commun.* **107** (1998) 639.
- [44] J. Ruvalds, *Supercond. Sci. Technol.* **9** (1996) 905.
- [45] B. Batlogg, *Solid State Commun.* **107** (1998) 639.
- [46] Z. Z. Sheng, A. M. Hermann, *Nature* **332** (1988) 55.
- [47] K. Tokiwa, H. Aota, C. Kunugi, K. Tanaka, Y. Tanaka, A. Iyo, H. Ihara, and T. Watanabe, *Physica B* **284** (2000) 1077.
- [48] K. Tanaka, A. Iyo, Y. Tanaka, K. Tokiwa, M. Tokumoto, M. Ariyama, T. Tsukamoto, T. Watanabe, and H. Ihara, *Physica B* **284** (2001) 1081.
- [49] L. G. Aslamazov and A. L. Larkin, *Phys. Lett. A* **26** (1968) 238.
- [50] K. Maki, *Prog. Theo. Phys.* **39** (1968) 897; R. S. Thompson, *Phys. Rev. B* **1** (1970) 327.
- [51] W. E. Lawrence and S. Doniach, of Proceedings of the Twelfth International Conference on *Low Temperature Physics*, Kyoto, 1970, (edited by Eizo Kanda) Keigaku, Tokyo (1971) p. 361.
- [52] S. Hikami and A. I. Larkin, *Mod. Phys. Lett. B* **2** (1998) 693.
- [53] P. Weiss, *J. De physique* **6** (1907) 661.
- [54] M. Farbod, M. R. Batvandi, *Physica C* **471** (2011) 112-117.
- [55] S. Rehman, A. Mumtaz, S. K. Hasanain *J. Nanopart. Res.* **13** (2011) 2497-2507.
- [56] M. M. Elokr, R. Awad, Asmaa Abd El-Ghany, A. Abou Shama and A. Abd El-wanis, *J. Supercond. Nov. Magn.* **24** (2010) 1345.
- [57] S. Graser, P. J. Hirschfeld, T. Kopp, R. Gutser, B. M. Andersen and J. Mannhart, *Nature Physics* **6** (2010) 609; H. Hilgenkamp, J. Mannhart *Rev. Mod. Phys.* **74** (2002).
- [58] N. H. Mohamed, A. I. Abou-Aly, I. H. Ibrahim, R. Awad and M. Rkaby, *J. Alloys compd.* **486** (2009) 733.
- [59] Khurram, Nawazish A. Khan, *J. Phys. Condens. Matter* **20** (2008) 045216.
- [60] I. A. Ansari, V. P. S Awana, R. Rawat, M. Shahabuddin, M. Hussain, H. Kishan, and A. V. Narlikar; *J. Mater. Sci.* **42** (2007) 6306-6309 (PhD thesis).
- [61] P. K. Nayak, S. Ravi, *Solid State Commun.* **140** (2006) 464-468.
- [62] D. Gingasu, I. Mindru, L. Patron, O. Carp, D. Matei, C. Neagu and I. Balint, *J. Alloys Compd.* **425** (2006) 357.
- [63] P. K. Khanna, S. Gaikwad, P. V. Adhyapak, N. Singh, and R. Marimuthu, *Mater. Lett.* **61** (2007) 4711.
- [64] K. Singh, R. Mohan, N. Kaur, N. K. Gaur, M. Dixit, V. Shelke, R.K. Singh *Physica C* **450** (2006) 124-128.
- [65] J. Zhu, D. Li, H. Chen, X. Yang, *J. Mater. Sci.* **58** (2004) 3324.
- [66] S. X. Dou, W. K. Yeoh, J. Horvat, and M. Ionescu *Appl. Phys. Lett.* **83** (2003) 4996.
- [67] G. Hammerl, H. Bielefeldt, S. Leitenmeier, A. Schmehl, C. W. Schneider, A. Weber, and J. Mannhart, *Eur. Phys. J. B* **27** (2002) 11.

- [68] Z. Y. Jia, H. Tang, Z.Q. Yang, Y.T. Xing, Y.Z. Wang, G.W. Qiao, *Physica C* **337** (2000) 130–132.
- [69] K. Ghosh, S. K. Bandyopadhyay, A. N. Basu, *J. App. Phys.* **86** (1999) 6
- [70] F. Fedirici, A. Varlamov, *Phy. Rev B* **55** (1997) 22.
- [71] S. V. Sharma, G. Sinha, T. K. Nath, S. Chakraborty, A.K. Majumda, *Physica C* **242** (1995) 351-359.
- [72] K. Pradhan, S. B. Roy, P. Chaddah, *Phy. Rev B* **50** (1994) 10.
- [73] L. B. Ioffe, A. I. Larkin, A. A. Varlamov, and L. Yu, *Phys. Rev. B* **47** (1993) 8936.
- [74] R. K. Nkum and W. R. Datars, *Phys. Rev. B* **44** (1991) 12.
- [75] Makoto Hikita, Minoru Suzuki, *Phys. Rev B* **41** (1990) 1.
- [76] L. G. Aslamazov and A. L. Larkin, *Phys. Lett. A* **26** (1968) 238.
- [77] A. M. Hermann, Thallium-Based High-Temperature Superconductors, (Marcel Dekker, Inc. (1994) p 41).
- [78] Torardi *et al.*, *Science* **240** (1988) 631.
- [79] N. L. Wu *et al.*, *Mater. Lett.* **7** (1988) 169.
- [80] N. L. Wu *et al.*, *Jpn. J. Appl. Phys.* **28** (1989) L1349.
- [81] N. L. Wu *et al.*, *Physica C* **161** (1989) 302.
- [82] E. Ruckenstein and C. T. Cheung, *J. Mater. Res.* **4** (1989) 1116.
- [83] E. Ruckenstein and S. Narain, *Mater. Lett.* **8** (1989) 421.
- [84] P. Barboux *et al.*, *J. Appl. Phys.* **63** (1988) 2725.
- [85] N. P. Ong, R. J. Cava, *Science* **305** (2004) 52.
- [86] X. Verma *et al.*, *Jpn. J. Appl. Phys.* **29** (1990) L880.
- [87] L. M. Liz-Marzan, P. V. Kamat, *Nanoscale Materials*, (Kluwer Academic Publishers, Boston, 2003).
- [88] Rath, N. C. Mishra, S. Anand, R. P. Das, K. K. Sahu, C. Upadhyay, and H. C. Verma, *Appl. Phys. Lett.* **76** (2000) 475.
- [89] G. A. Olah, N. Laureate, and H. S. Nalwa, *Handbook of Nanostructured Materials and Nanotechnology* (Academic Press, San Diego, Vol. 1, 2000).
- [90] S. C. Tjong, and H. Chen, *Mater. Sci. Eng.* **45** (2004) 1.
- [91] J. Sjoblom, R. Lindberg, and S. E. Friberg, *Adv. Colloid Interface Sci.* **65** (2005) 125.
- [92] M. Yushimura, and S. Somiya, *Mater. Chem. Phys.* **1** (1999) 61.
- [93] H. J. Hah, *J. Sol-Gel Sci. Technol.* **26** (2003) 467.
- [94] D. Cullity, *Element of X-ray Diffraction*, Second edition, (Addision-Wesely Publishing company, Inc. London 1977).
- [95] M. Ali Omer, *Elementary Solid State Physics*, First edition, (Wesley Publishing Company, 1974).
- [96] http://www.sciencebuddies.org/mentoring/project_ideas/Elec_p025.shtml
- [97] N. Ashcroft, N. Mermin *Solid State Physics* (Orlando, FL: Saunders, 31, 1976, pp:346).
- [98] P. Nozieres *Theory of Interacting Fermi Systems* (New York, NY: Benjamin, 1964, pp:92).
- [99] Kittel *Introduction to Solid State Physics* (New York, NY: Wiley, 1976).
- [100] H. Ihara, K. Tokiwa, H. Ozawa, M. Hirabayashi, A. Negishi, H. Matuhata, and Y. S. Song, *Jpn. J. Appl. Phys.* **33** (1994) L503.
- [101] H. Ihara, *Physica C* **364-365** (2001) 289.
- [102] Z. Z. Sheng and A. M. Hermann, *Nature* **332** (1988) 55.
- [103] Z. Z. Sheng, A. M. Hermann, A. E. Ali, C. Almasan, J. Estrada, T. Datta, and R. J. Matson, *Phys. Rev. Lett.* **60** (1988) 937.
- [104] Z. Z. Sheng, and A. M. Hermann, *Nature* **332** (1988) 138.

- [105] G. Malandrino, D. S. Richeson, T. J. Marks, D. C. De Groot, J. L. Schindler, and C. R. Kannewurf, *Appl. Phys. Lett.* **58** (1991) 182.
- [106] M. L. Chu, H. L. Chang, C. Wang, J. Y. Juang, T. M. Uen, and Y. S. Gou, *Appl. Phys. Lett.* **59** (1991) 1123.
- [107] W. L. Oslon, M. M. Eddy, T. W. James, R. B. Hammond, G. Gruner, and L. Drabeck, *Appl. Phys. Lett.* **55** (1989) 188.
- [108] M. Kikuchi, T. Kajitani, T. Suzuki, S. Nakajima, K. Hiraga, N. Kobayashi, H. Iwasaki, Y. Syono, and Y. Muto, *Jpn. J. Appl. Phys.* **28** (1989) L382.
- [109] S. S. P. Parkin, V. Y. Lee, E. M. Engler, A. I. Nazzal, T. C. Huang, G. Gormau, R. Savoy, and R. Beyer, *Phys. Rev. Lett.* **60** (1988) 2539.
- [110] K. Schuller, and J. D. Jorgensen, *Mater. Res. Bull.* **XIV** (1989) 27.
- [111] W. Sleight, M. A. Subramanian, and C. C. Torardi, *Mater. Res. Bull.* **XIV** (1989) 45.
- [112] J. B. Parise, J. Gopalkrishnan, M. A. Subramanian, and A. W. Sleight, *J. Solid State Chem.* **76** (1988) 432.
- [113] Y. Tang, B. Lin, D. Zhou, W. Zhu, F. Chen, N. Li, K. Chen, and G. Lu, *Mod. Phys. Lett. B* **3** (1989) 853.
- [114] Sundaresan, H. Asada, A. Crisan, J. C. Nie, H. Kito, A. Iyo, Y. Tanaka, M. Kusunoki, and S. Ohshima, *IEEE Trans Appl. Supercond.* **13** (2003) 2913.
- [115] J. Y. Juang, J. H. Horng, S. P. Chen, C. M. Fu, K. H. Wu, T. M. Uen, and Y. S. Gou, *Appl. Phys. Lett.* **60** (1995) 885.
- [116] Sundaresan, H. Asada, A. Crisan, J. C. Nie, H. Kito, A. Iyo, T. Tanaka, M. Kusunoki, and S. Oshima, *Physica C* **388** (2003) 473.
- [117] J. Miller, J. G. Hu, J. D. Hettinger, K. E. Gray, J. E. Tkaczyk, J. Deluca, P. L. Karas, J. A. Sutliff, and M. F. Garauskas, *Appl. Phys. Lett.* **63** (1993) 556.
- [118] Iyo, Y. Ishiura, Y. Tanaka, P. Badica, K. Tokiwa, T. Watanabe, and H. Ihara, *Physica C* **370** (2002) 205.
- [119] W. Mexner, J. Hoffmann, S. Heede, K. Heinemann, H. C. Freyhardt, F. Ladenberger, and E. Schwarzmann, *Z. Phys. B* **101** (1996) 181.
- [120] N. Zheng, J. D. Johnson, A. R. Jones, A. M. Campbell, W. Y. Liang, T. Doi, M. Okada, and K. Higashiyama, *J. Appl. Phys.* **77** (1995) 5287.
- [121] R. T. Liu, S. L. Yan, L. Fang, and M. He, *Supercond. Sci. Technol.* **14** (2001) 948.
- [122] R. S. Liu, D. N. Zheng, J. W. Loram, K. A. Mirza, A. M. Campbell, and P. P. Edwards, *Appl. Phys. Lett.* **60** (1992) 1019.
- [123] S. H. Yun and J.Z. Wu, *Appl. Phys. Lett.* **68** (1996) 862.
- [124] Nawazish A. Khan, M. Mumtaz, A. A. Khurram, and P. Kameli, *Physica C* **468** (2008) 233.
- [125] N. A. Khan, M. Mumtaz, K. Sabeeh, M. I. A. Khan, and M. Ahmed, *Physica C* **407** (2004) 103.
- [126] K. Semba, A. Matsuda, and T. Ishii, *Phys. Rev. B* **49** (1996) 10043.
- [127] M. K. Wu, J. R. Ashburn, C. J. Torng, P. H. Hor, R. L. Meng, L. Gao, Z. J. Huang, Y. Q. Wang, and C. W. Chu, *Phys. Rev. Lett.* **58** (1987) 908.
- [128] K. Heine, J. Tenbrink, M. Thoner, *Appl. Phys. Lett.* **55** (1989) 2441.
- [129] J. Y. Yuang, J. H. Horng, S. P. Chen, C. M. Fu, K. H. Wu, T. M. Uen, and Y. S. Gou, *Appl. Phys. Lett.* **66** (1995) 885.
- [130] M. Mumtaz, Nawazish A. Khan, and S. Khan, *J. Appl. Phys.* **107** (2010) 103905.
- [131] M. Mumtaz, Nawazish A. Khan, and E. U. Khan, *Physica C* **470** (2010) 428.
- [132] Nawazish. A. Khan and M. Mumtaz, *J. Low Temp. Phys.* **151** (2008) 1221.
- [133] Wang, Z. Gao, L. Wang, Y. Qi, D. Wang, C. Yao, Z. Zhang, and Y. Ma, *Supercond. Sci. Technol.* **23** (2010) 055002.
- [134] N. L. Wang, M. Ziaei, B.P. Clayman, and G.D. Gu, *Physica C* **341** (2000) 2227.

- [135] Shi, M.S. Boley, U. Whelp, J.G. Chen, and Y. Liao, *Phys. Rev. B* **40** (1989) 5255.
- [136] H. Shakeripour and M. Akhavan, *Supercond. Sci. Technol.* **14** (2001) 234.
- [137] P. Malozemoff, Q. Li, and S. Flesher, *Physica C* **424** (1997) 282.
- [138] M. Schwartz, *New material processes and method technology* (CRC, New York, 2006).
- [139] Buzea, I. I. Pacheco, and K. Robbie, *Nanomaterials and nanoparticles: Sources and toxicity Biointer phases* **2** (2007) 17.
- [140] P. K. Stoimenov, R. L. Klinger, G. L. Marchin, and K. J. Klabunde, *Langmuir* **18** (2002) 6679.
- [141] Koch, *Nanostructured materials processes properties and potential applications* (Noyes Publications, New York, 2002).
- [142] W. Zhang, Q. R. Zhang, T. Y. Liu, Y. Y. Sun, K. Tao, and J. Gale, *J. Uni. Shanghai, S. Technol.* **27** (2005) 104.
- [143] R. Awad, *J. Supercond. Nov. Magn.* **21** (2008) 461.
- [144] Baqiah, S. H. M. Adam, S. Chen, S. Ravandi, M. Faisal, M. Kamarul zaman, and M. Hanif, *Solid State Sci. Technol.* **17** (2009) 81.
- [145] S. Dou, S. Soltania, Y. Zhao, E. Getin, Z. Chen, O. Shcherbakova, and J. Horvat, *J. Supercond. Sci. Technol.* **18** (2005) 710.
- [146] M. Eloker, R. Awad, A. A. E. Ghany, A. A. Shama, and A. A. Elwanis, *J Supercond Nov. Magn.* **24** (2011) 1345.
- [147] N. Mohamed, A. Abou-Aly, I. Ibrahim, R. Awad, and M. Rkaby, *J. Alloys Compd.* **486** (2009) 733.
- [148] L. Aslamazov and A. Larkin, *Sov. Phys. Solid Stat.* **10** (1968) 875.
- [149] W. Lawrence and S. Doniach, *Sov. Phys. Solid Stat.* **10** (1971) 361.
- [150] Passos, M. Orland, O. Passamai, E. de Mello, H. Correa, and L. G. Martinez, *Phys. Rev. B* **74** (2006) 094514.

■

